Design, Implementation and Characterization of the Advanced LIGO 200 W Laser System

Von der Fakultät für Mathematik und Physik

der Gottfried Wilhelm Leibniz Universität Hannover

zur Erlangung des Grades

Doktor der Naturwissenschaften

Dr. rer. nat.

genehmigte Dissertation

von

Dipl.-Phys. Jan Hendrik Põld

geboren am 11.09.1984 in Bielefeld

2014

Referent:	PD Dr. Benno Willke
Korreferent:	Prof. Dr. Kenneth A. Strain
Tag der Promotion:	06.06.2014

Abstract

Observations of the universe will be conducted with the Advanced LIGO gravitational wave detectors starting early 2015. These detectors reach an unprecedented sensitivity aiming for the first direct detection of gravitational waves.

Advanced LIGO employs a new high power laser system. The development and implementation of the high power laser together with a filter cavity called Pre-Modecleaner, the power- and frequency stabilization systems is described in this thesis.

Three Advanced LIGO laser systems were characterized over the course of three years at output power levels of 17 W and 180 W. The laser systems operate reliably and at their design performance level. For spatial and temporal filtering of the high power laser beam a bow tie shaped Pre-Modecleaner was designed, tested and extensively characterized.

Furthermore, the implementation of the in vacuum sensor for the power stabilization is discussed. The performance of the power stabilization is simulated and the simulations are compared to the measured results. A quantum noise limited performance over a wide frequency band from 30 Hz to 500 Hz was achieved at a relative power noise level of $3.5 \cdot 10^{-8}/\sqrt{\text{Hz}}$.

The existing frequency stabilization scheme from a prior LIGO configuration was adapted for Advanced LIGO and the effects impressed by the high power oscillator, which amplifies the output power up to 200 W, are evaluated. The high bandwidth feedback control loop which employs a rigid cavity as frequency reference is characterized and a frequency noise measurement is obtained with the Advanced LIGO Input-Modecleaner, a suspended in vacuum resonator with a round trip length of 32 m.

A high power test in order to study thermal effects in the Input-Modecleaner is conducted with input power levels up to 120 W.

Keywords: laser characterization, power stabilization, frequency stabilization

Kurzfassung

Beobachtungen des Universums können ab 2015 mit den Advanced LIGO Gravitationswellendetektoren durchgeführt werden. Diese Detektoren erreichen eine noch nie da gewesene Messgenauigkeit, um die erste, direkte Detektion von Gravitationswellen zu ermöglichen.

Advanced LIGO verwendet ein neues Hochleistungslasersystem. In der vorliegenden Arbeit wird die Entwicklung und Implementierung des Hochleistungslasers sowie eines Filterresonators, genannt Pre-Modecleaner, und der Leistungs- und Frequenzstabilisierung beschrieben.

Drei Advanced LIGO Lasersysteme wurden über einen Zeitraum von drei Jahren bei Ausgangsleistungen von 17 W und 180 W charakterisiert. Die Lasersysteme funktionieren zuverlässig und erreichen ihre Designziele. Für die räumliche und zeitliche Filterung des Hochleistungslaserstrahls wurde ein Pre-Modecleaner konstruiert, getestet und charakterisiert.

Außerdem wird die Implementierung eines sich im Vakuum befindenden Sensors für die Leistungsstabilisierung beschrieben. Die Effizienz der Leistungsstabilisierung wurde simuliert und die Simulationen mit den gemessenen Resultaten verglichen. In einem breiten Frequenzbereich von 30 Hz bis 500 Hz wurde eine quantenrauschbegrenzte Stabilisierung mit einem relativen Leistungsrauschen von $3.5 \cdot 10^{-8}/\sqrt{\text{Hz}}$ erreicht.

Das bestehende Frequenzstabilisierungskonzept einer früheren LIGO Konfiguration wurde für Advanced LIGO angepasst und Effekte untersucht, die durch die Verstärkung des Ausgangsstrahls auf bis zu 200 W mittels eines Hochleistungsoszillators aufgeprägt werden. Die dazu gehörige Regelschleife, die mit hoher Bandbreite betrieben wird und einen starren Resonator als Frequenzreferenz besitzt, wird charakterisiert und das Frequenzrauschen mit Hilfe des Advanced LIGO Input-Modecleaner, einem im Vakuum aufgehängten Resonator mit 32 m Umlauflänge, gemessen.

Um thermische Effekte im Input-Modecleaner zu untersuchen, wurde ein Test mit Eingangsleistungen von bis zu 120 W durchgeführt.

Schlagwörter: Lasercharakterisierung, Leistungsstabilisierung, Frequenzstabilisierung

Contents

Acronyms

AEI Albert Einstein Institute

aLIGO Advanced LIGO

AOM acousto-optic modulator

AR anti reflective

BJT bipolar junction transistor

BS beamsplitter

CDS control and data system

DBB diagnostic breadboard

DWS differential wavefront sensing

EOM electro-optic modulator

ET Einstein Telescope

ETM end test mass

FET field-effect transistor

FFU fan filter unit

FSR free spectral range

FSS frequency stabilization servo

FTIR Fourier transform infrared spectroscopy

GBP gain bandwidth product

GEO GEO600

GWD gravitational wave detector

HEPA high-efficiency particulate absorption

HG Hermite-Gaussian

HPL high power laser

HPM high power mode

HPO high power oscillator

HR high reflective

IFO interferometer

iLIGO initial LIGO

IMC Input-Modecleaner

InGaAs indium gallium arsenide

ITM input test mass

LG Laguerre-Gaussian

LHO LIGO Hanford Observatory

LIGO Laser Interferometer Gravitational-Wave Observatory

LLO LIGO Livingston Observatory

LPM low power mode

LRA long range actuator

LTI linear time invariant

NE noise eater

NPRO non-planar-ring-oscillator

OMC Output-Modecleaner

OP operational amplifier

PD photo detector

PDH Pound-Drever-Hall

PMC Pre-Modecleaner

PRC power recycling cavity

PRM power recycling mirror

PSL pre-stabilized laser

PZT piezoelectric transducer

QPD quadrant photodiode

RAM residual amplitude modulation

RF radio frequency

RIN relative power noise

ROC radius of curvature

RPN radiation pressure noise

RSE resonant sideband extraction

RTP Rubidium Titanyle Phosphate

SiC silicon carbide

SNR signal to noise ratio

SRC signal recycling cavity

SRM signal recycling mirror

TIA transimpedance amplifier

TTFSS table top frequency stabilization servo

UGF unity gain frequency

UHV ultra high vacuum

VCO voltage controlled oscillator

VGA variable gain amplifier

WFS wavefront sensor

1 Introduction

The existence of gravitational waves was predicted by Albert Einstein as a consequence of his theory of general relativity nearly one hundred years ago [Ein16, Ein18]. Gravitational waves are perturbations of space-time caused by astrophysical sources such as binary star- or black hole mergers. As their coupling to matter is extremely weak they are very hard to detect.

To date no direct detection of gravitational wave has been made. However, there are observations that imply a strong evidence of the existence of gravitational waves. Hulse and Taylor observed the binary pulsar system B1913+16 and found that the energy loss of the system matches the calculated emission into gravitational waves [WNT10]. Another result that suggests the existence of gravitational waves is obtained from the BICEP2 experiment, which observed a unique B-mode polarization signature in the cosmic microwave background that implies primordial gravitational waves [Col14].

Efforts for a direct detection of gravitational waves led to the construction of kilometer scale interferometric gravitational wave detectors (GWDs). A network of GWDs formed by LIGO [AAA$^+$09a], VIRGO [AAA$^+$12] and GEO600 [GtLSC10] has been established at the beginning of this century. Joint data runs were performed and the detectors reached an unprecedented strain sensitivity of 10^{-22}. In order to further enhance the sensitivity major upgrades are implemented in the existing detectors, while a new detector called KAGRA is currently being built in Japan [Som12]. The operation of these, so called advanced detectors, will start in early 2015 and by the time they reach their design sensitivity the detection of gravitational waves is expected on a regular basis. This will open a new field of gravitational wave astronomy in the near future.

One key element of the upgrade program is the implementation of a new high power laser system. In case of Advanced LIGO (aLIGO) [HtLSC10], the laser system is specifically designed to meet the challenging requirements set by the

GWD [WPK+11, KBD+12]. This thesis describes the design, implementation and long term characterization of the aLIGO laser systems and their power- and frequency stabilization.

Outline

In Chapter 2 the LIGO detector is described. It is explained how gravitational waves are measured with a Michelson-Interferometer and the sensitivity of the detector is evaluated.

Chapter 3 gives a detailed overview of the design of the aLIGO laser system, which was implemented at both LIGO observatories. It is characterized and analyzed in a long term test. A resonator, called Pre-Modecleaner (PMC), that is responsible for temporal and spatial beam filtering is described and characterized.

Chapter 4 describes the power stabilization scheme for aLIGO, which is designed to stabilize the power noise to a level of $2 \cdot 10^{-9}/\sqrt{\text{Hz}}$ at the input of the interferometer (IFO). The control loop was designed and fabricated. The simulated performance is compared to measured results.

Chapter 5 discusses the nested frequency stabilization control loop, which employs a rigid reference cavity as a frequency reference. An existing control scheme is adapted to the aLIGO laser system. The performance of the control loop and the resulting frequency noise is analyzed with an out-of-loop measurement performed with the Input-Modecleaner (IMC). Moreover, the IMC is tested with an input power of 120 W.

At the end of the thesis important results and implications are summarized in Chapter 6.

2 Advanced LIGO

The Laser Interferometer Gravitational-Wave Observatories (LIGO) are two terrestrial interferometric gravitational wave detectors in the USA with detector sites in Livingston, Louisiana, and Hanford, Washington. They have been operating since 2002 in a configuration that is called initial LIGO [AAA+09a] and are currently upgraded to improve the sensitivity to the Advanced LIGO configuration [HtLSC10].

Gravitational waves cause perturbations of space-time which stretch and contract the distance between two distant test masses. As the gravitational waves stretch the space-time in one direction while contracting it in the perpendicular direction, a Michelson IFO is able to detect this differential length change in the perpendicular arms. Even gigantic cosmic events produce gravitational waves that lead to strain amplitudes $\Delta L/L$ of less than 10^{-22} when they pass the earth.

In order to measure length changes with such a high precision, the aLIGO detector comprises a 200 W high power laser, state-of-the-art precision optics, advanced suspension and seismic isolation systems and a sophisticated control scheme [HtLSC10, Adh14]. Figure 2.1 pictures an overview of the aLIGO detector. The high power laser beam is generated by a 35 W laser and a high power oscillator (HPO) as described in detail in Chapter 3. The beam is temporally and spatially filtered with resonators, called PMC (Sec. 3.2) and an Input-Modecleaner (IMC) (Sec. 5.4), outside and inside the vacuum system respectively. A maximum power of 125 W will be available in front of the power recycling mirror (PRM).

The IFO itself consists of a beamsplitter (BS) and two end test masses (ETMs). Additionally, a PRM to resonantly enhance the power impinging on the BS and arm cavities consisting of an input test mass (ITM) and the ETM to increase the storage time of the light in the IFO arms are implemented. The length of the arm cavities is 4 km and the power stored inside is up to 800 kW. Moreover, a

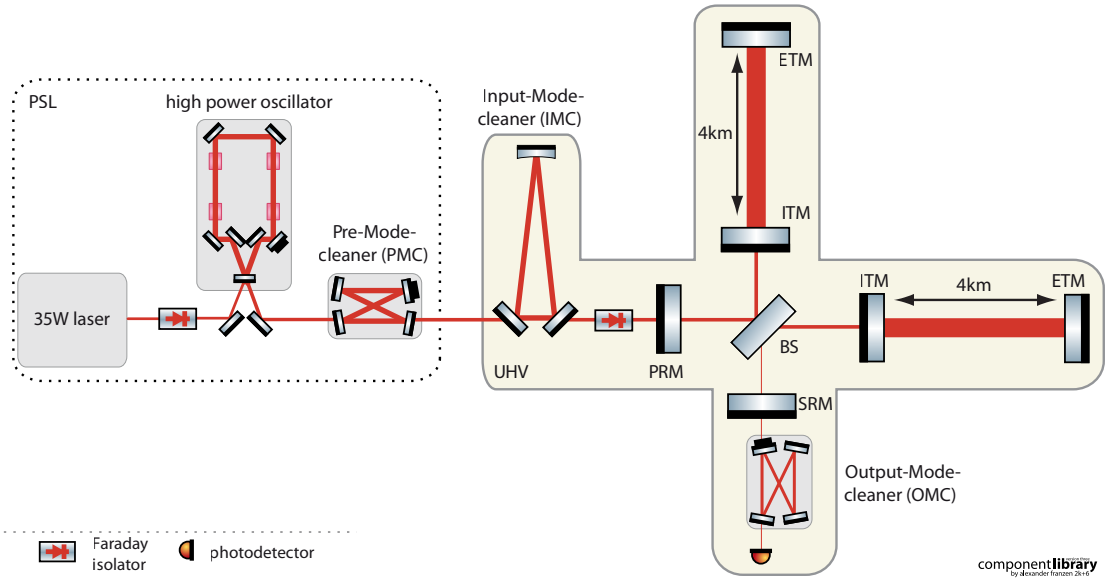

Figure 2.1: Advanced LIGO detector layout. The Input-Modecleaner, interferometer and the readout for the gravitational wave signal are contained in an ultra high vacuum (UHV) enclosure. (PSL: prestabilized laser; PRM: power recycling mirror; BS: beamsplitter; ETM: end test mass; ITM: input test mass; SRM: signal recycling mirror)

signal recycling mirror (SRM) at the output port of the IFO can, depending on the tuning, either increase or decrease the power buildup for the gravitational wave signal [Mee88, Miz95]. An IFO in this configuration is said to be dual-recycled.

At the output of the IFO an Output-Modecleaner (OMC) filters the beam in terms of higher order spatial modes and radio frequency (RF) modulation sidebands, such that they do not contribute to the gravitational wave signal sensed with a photo detector (PD) downstream of the OMC. In order to limit the amount of light on the readout PD and to reduce the influence of power noise (Chap. 4) the detector is operated close to the dark fringe, which means that most of the light is sent back to the PRM.

Compared to iLIGO the aLIGO strain sensitivity improves by a factor of 10. A noise budget for the aLIGO detector for a power level of 125 W in front of the PRM and zero-detuning is shown in Figure 2.2. The detector is generally limited by displacement and sensing noise. While displacement noise combines disturbances that have an effect on the position of the mirrors, sensing noises sum up noise sources that limit the determination of the mirror position without

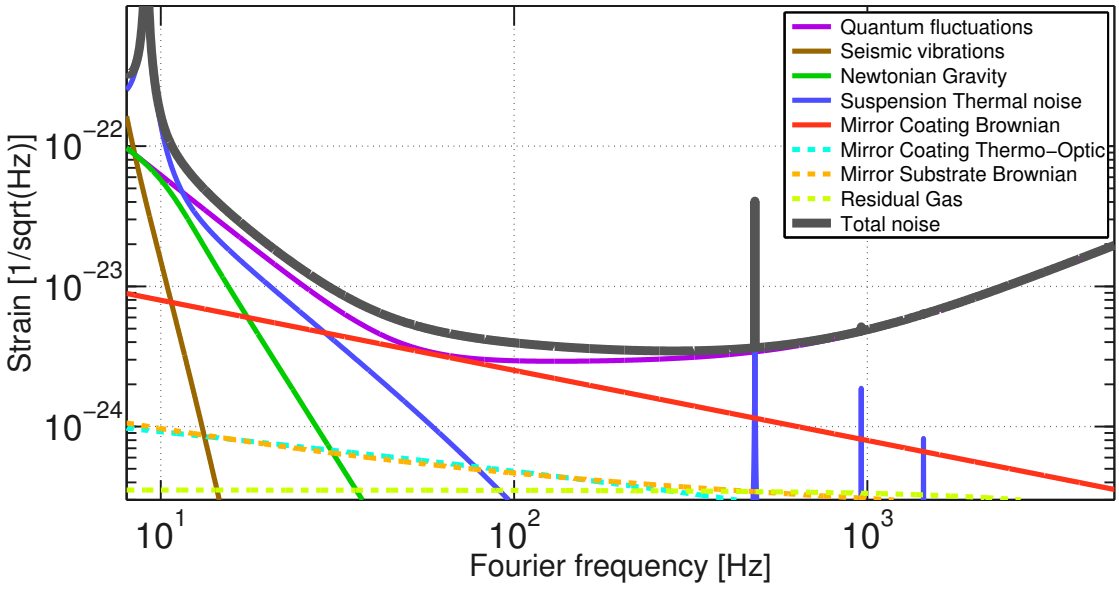

Figure 2.2: Advanced LIGO noise budget with 125 W input power upstream the PRM and zero-detuning of the SRM [GWI13]. The detector is limited by quantum noise in the most sensitive frequency band. However around 60 Hz the coating thermal noise contribution is on the same level than the quantum noise.

the presence of displacement noise. Advanced LIGO is limited in the most sensitive frequency band by noise arising from the quantum vacuum fluctuations entering the detector at the output port. In an IFO without signal recycling and arm cavities quantum noise is described as linear spectral density by [Sau94, Chap. 5]

$$h_{\text{quantum}} = \frac{1}{L}\sqrt{\left(\sqrt{\frac{\hbar c\lambda}{2\pi P_{BS}}}\right)^2 + \left(\frac{1}{mf^2}\sqrt{\frac{\hbar P_{BS}}{2\pi^3 c\lambda}}\right)^2} \tag{2.1}$$

with m being the mirror mass, c the speed of light, P_{BS} the laser power in front of the BS, L the IFO arm length, λ the wavelength of the light and f the Fourier frequency. The first term in Equation (2.1) describes the photon shot noise contribution and the second term accounts for quantum radiation pressure effects. For a dual-recycled IFO configuration with arm cavities the pole frequency of the arm cavities and the effects from the signal recycling cavity (SRC) have to be added [BC01]. The detector sensitivity is also limited as well by coating thermal noise around 60 Hz, which imposes noise at the same level than the quantum noise contribution.

For a quantum noise limited GWD high power lasers are important to improve the sensitivity at high Fourier frequencies. However, for commissioning activities and first science runs the laser power is attenuated before entering the vacuum system as risks of damaging optical components with a high power beam should be reduced during the testing of the control system. The construction of the aLIGO detector is planned to be completed early 2015 with the demonstration of a two hour lock of the full instrument. The first science run is planned for three month in 2015 and the detectors design sensitivity will presumably be reached in 2019 [RftL13].

3

Advanced LIGO laser and Pre-Modecleaner characterization

High power lasers are an essential part of the upgrade to the second-generation of gravitational wave detectors, because the input power of the IFO determines the shot noise limited sensitivity of the detector at high Fourier frequencies. In comparison to the first generation of GWDs the laser power increases from 10 W to 200 W for the second generation. Since the IFO needs to be operated with a single frequency, fundamental Gaussian mode input beam, higher order spatial modes have to be filtered before the beam enters the IFO. Consequently, high fundamental mode content and single frequency operation are two of the requirements for the aLIGO laser system.

In the past high power lasers with output power levels up to 65 W have been built for GWDs. All of them generate infrared light at 1064 nm and follow two different concepts for the high power generation. While the earlier LIGO lasers were master laser power amplifier [SKS98, FSW+07], VIRGO, GEO600 and TAMA used injection locked laser systems [BBC+02, ZBD+02, AtTC05]. For the aLIGO laser both concepts are combined.

In addition to the laser systems that were installed at the two LIGO observatories, a Reference System is operated since 2010 at the Albert Einstein Institute (AEI) in Hannover. This system serves as test bed for upgrades before they are implemented at the LIGO observatories. Furthermore, in an experiment with the high power beam generated by the aLIGO laser 134 W at a wavelength of 532 nm by second-harmonic generation were demonstrated [MWD10]. A different experiment achieved 83 W in a ninth order Laguerre-Gaussian (LG) mode [CBF+13, Bog13].

In the first part of this Chapter (Sec. 3.1) the characterization of the laser system for aLIGO is described and important parameters for laser stabilization are introduced. Focus is put on the reliability and diagnostics of the system. More-

over, an optical resonator, called Pre-Modecleaner is described in Section 3.2 that is responsible for filtering the higher order spatial modes that are present in the laser beam. Additionally, the PMC is a filter for beam pointing fluctuations, power- and frequency fluctuations at radio frequencies.

3.1 Laser characterization

A high fundamental mode content is only one aspect that makes a laser source suitable for the use in GWDs. Other important parameters are power noise, frequency noise and pointing noise. The requirements for those properties are very strict and a robust operation is demanded. These fundamental parameters are introduced in Section 3.1.1. A description of the aLIGO laser system is given in Section 3.1.2 and the possibilities to perform laser diagnostics with a tool called diagnostic breadboard (DBB), is referred to in Section 3.1.3. Afterwards the results of the laser characterization are presented (Sec. 3.1.4) and an outlook on a laser for next generation GWD (Sec. 3.1.5) concludes the first part of this Chapter.

3.1.1 Fundamental parameters

The concepts and parameters that are introduced in this Section are important throughout the thesis, as they are the basics for laser characterization. The analysis of noise is usually performed in the frequency domain obtaining linear spectral densities from the signals of interest. The output signal of a gravitational wave detector is most sensitive between Fourier frequencies from 10 Hz to 10 kHz. However, requirements for the laser exceed this frequency band in some cases, as non-linear effects like up conversion or noise due to heterodyne signal readout call for certain noise limits in a wider frequency band.

Gaussian beams

Laser beams are transversal electromagnetic waves. They can be described as Gaussian beams with z being the direction of propagation. A fundamental Gaussian beam is one solution of the paraxial Helmholtz equation with a complex amplitude [ST91, Chap. 3.1]:

$$U(\rho, z, t) = U_0(t) \cdot \frac{\omega_0}{\omega(z)} \exp\Big(-\frac{\rho^2}{\omega^2(z)}\Big) \exp(-i\varphi(\rho, z)) \tag{3.1}$$

$$\omega_0 = \sqrt{\frac{\lambda z_0}{\pi}}. \tag{3.2}$$

$U_0(t)$ is the time dependent amplitude, $\omega(z)$ the beam radius, ω_0 the beam radius at z=0, $\rho^2 = x^2 + y^2$ and φ the phase; λ denotes the wavelength of the laser beam and z_0 the Rayleigh range, at which the beam size is $\sqrt{2}\omega_0$. For $z \gg z_0$ the half divergence angle Θ_D of the Gaussian beam is defined as

$$\Theta_D = \frac{\lambda}{\pi\omega_0}. \tag{3.3}$$

Beside fundamental Gaussian beam there are other solutions of the paraxial Helmholtz equation. A special set of function that form an orthogonal, complete basis are Hermite-Gaussian (HG_{nm}) and Laguerre-Gaussian (LG_{lp}) polynomials and the indices indicate the mode order [ST91, Chap. 3.3, 3.4]. Like the fundamental Gaussian beam they have paraboloidal wavefronts and are important for the description of laser beams since they can appear as modes of a resonator with spherical mirrors.

Frequency noise

The frequency of a laser is related to its wavelength via

$$\lambda = \frac{c}{\nu}. \tag{3.4}$$

Frequency noise describes fluctuations of ν. Frequency fluctuations can also be described as fluctuations in the phase as both properties are closely related.

Power noise

Intensity I and power P of a Gaussian beam are defined as:

$$I(\rho, t) = |U(\rho, t)|^2 \tag{3.5}$$

$$P(t) = \int d\rho\, I(\rho, t) \tag{3.6}$$

A sophisticated device to measure the power noise is a PD. Since a PD cannot resolve the terahertz frequency of the laser beam, as it is bandwidth limited due to its internal properties and the readout electronics, it cannot measure the electric field directly. Instead it can measure the energy transfer to the PD material and consequently the power of the beam. Thus, power noise is only accessible within the PD bandwidth.

A normalization of the measured power P(t) by the average power $\langle P(t)\rangle$ is called relative power noise (RIN)[1]:

$$RIN = \frac{P(t)}{\langle P(t)\rangle}, \quad \langle P(t)\rangle = \frac{1}{T}\int_0^T dt\, P(t). \tag{3.7}$$

The calibration of power noise in units of RIN is convenient to compare measurements that are taken at locations with different power levels.

Pointing noise

Fluctuations of the beam position, so called pointing noise, are expressed as a mixture of translational and angular deviation from a reference beam. Pointing is described as a complex quantity ϵ with [And84, KSWD07]

$$\epsilon = \frac{\delta x}{\omega_0} + i\frac{\delta\alpha}{\Theta_D}. \tag{3.8}$$

The translational fluctuations are normalized to the beam waist and the angular fluctuations to the half divergence angle. Therefore two measurements of ϵ can be directly compared independent of their location with respect to the optical system.

Amplitude- and phase modulation

The electric field of a wave with the complex amplitude U (Eq. (3.1)) is described by the wave function

$$u(t) = U(t)\cos(\omega_0 t + \varphi(t)) = \Re(a e^{i\omega_0 t}) \tag{3.9}$$

$$a(t) = U(t)\exp(i\varphi(t)) \tag{3.10}$$

with angular frequency ω_0 and time dependent phase $\varphi(t)$. Small deviations in amplitude and phase can be considered as amplitude and phase modulation sidebands at the modulation frequency ω_{mod} around the carrier field at ω_0, which are obtained by [Miz95]:

$$\begin{aligned} a_{AM}e^{i\omega_0 t} &= a_0(1 + m_{AM}\cos(\omega_{mod}t))e^{i\omega_0 t} \\ &= a_0\left(e^{i\omega_0 t} + \frac{m_{AM}}{2}e^{i(\omega_0+\omega_{mod})t} + \frac{m_{AM}}{2}e^{i(\omega_0-\omega_{mod})t}\right) \end{aligned} \tag{3.11}$$

$$a_{PM}e^{i\omega_0 t} = a_0 \cdot \exp(i m_{PM}\cos(\omega_{mod}t))e^{i\omega_0 t} \tag{3.12}$$

$$= a_0\left(e^{i\omega_0 t} + i\frac{m_{PM}}{2}e^{i(\omega_0+\omega_{mod})t} + i\frac{m_{PM}}{2}e^{i(\omega_0-\omega_{mod})t} + \mathcal{O}(m^2)\right)$$

[1] Relative power noise is historically often referred to as relative intensity noise and since RPN is associated with radiation pressure noise the abbreviation RIN will be used in this thesis.

The strength of the modulation is given by the modulation index m and a_0 is the time independent amplitude of the field a. In both cases there is an upper sideband at $\omega_0 + \omega_{mod}$ and a lower sideband at $\omega_0 - \omega_{mod}$. Frequency fluctuations are very similar to phase fluctuations, as the frequency is the derivative of the total phase $\Phi = \omega_0 t + \varphi(t)$. Hence a frequency modulation can be written as a phase modulation [Hei99]

$$\Phi(t) = \int dt(\omega_0 + m_{FM} \sin(\omega_{mod} t)) = \omega_0 t - \frac{m_{FM}}{\omega_{mod}} \cos(\omega_{mod} t)) \quad (3.13)$$

which has a strength of m_{FM} and depends on the modulation frequency. A frequency modulation can be described as a phase modulation with modulation index

$$m_{PM} = \frac{m_{FM}}{\omega_{mod}}. \quad (3.14)$$

Resonator

Optical resonators in different configurations are utilized for experiments conducted in this thesis. Hence, general properties of resonators are reviewed in this Section.

The spacing between neighboring resonance frequencies is defined as free spectral range ν_{FSR} [ST91, Chap. 9.1]

$$\nu_{FSR} = \frac{c}{L_{rt}} \quad (3.15)$$

which depends on the resonator round trip length L_{rt} and the speed of light c.

An incoming light field can be resonantly enhanced by the resonator. In order to achieve a high power buildup inside the resonator internal losses have to be very small. Moreover, the phase matching of the incoming field U_{in} and the circulating field U_{circ} is important. The resonant enhancement of the incoming field is expressed as [ST91, Chap. 2.5]

$$U_{circ}(\Phi_{rt}) = \frac{U_{in}}{1 - r^2 \cdot \exp(-i\Phi_{rt})}. \quad (3.16)$$

r is the amplitude reflectivity of the in- and outcoupling mirrors and Φ_{rt} describes the phase accumulated after one round trip. Here it is assumed that no internal losses are present. In case the of negligible internal losses and if both the in- and the outcoupling mirror have the same transmissivity the resonator is called impedance matched.

Another characteristic resonator property is the finesse $\mathcal{F}$ which accounts for internal losses [ST91, Chap. 9.1]:

$$\mathcal{F} = \frac{\pi r}{1 - r^2} \approx \frac{\nu_{FSR}}{\nu_{LW}}. \tag{3.17}$$

For a high finesse resonator the finesse also represents the ratio of free spectral range and the resonator linewidth, that is the full width at half maximum of the resonance peak.

Resonators are often used because they filter the impinging beam temporally and spatially. This is due to the fact that light that is phase shifted and accordingly not exactly aligned with the center of the resonance peak does not experience the full power buildup inside the resonator. Comparing the power buildup of a field at resonance with a phase shifted one yields

$$\frac{U_{circ}(\Phi_{rt})}{U_{circ}(0)} = \frac{1 - r^2}{1 - r^2 \cdot \exp(-i\Phi_{rt})} \approx \frac{1 - r^2}{1 - r^2(1 - i\frac{2\pi\nu}{\nu_{FSR}})} = \frac{1}{1 + i\frac{\nu}{\nu_0}} \tag{3.18}$$

$$\nu_0 = \nu_{FSR}\left(\frac{1 - r^2}{2\pi r^2}\right) \tag{3.19}$$

$$\Phi_{rt} = \frac{2\pi\nu}{\nu_{FSR}}. \tag{3.20}$$

For $\Phi_{rt} \ll 2\pi$ the reduction in the power buildup shows a single pole low pass behavior, called resonator pole, with $\nu_0 = \frac{\nu_{LW}}{2}$ as pole frequency. If the carrier of an amplitude modulated beam as described in Equation (3.11) is resonant in the resonator, the amplitude modulation sidebands are attenuated in the transmitted beam. The amount of attenuation can be obtained by inserting $\Phi_{rt} = \frac{2\pi\nu_{mod}}{\nu_{FSR}}$ in Equation (3.18).

3.1.2 The Advanced LIGO laser

In 2001 the development for the aLIGO laser started since no high power laser with sufficient noise characteristics[2] was available at that time. A first version of this continuous wave system was set up in the lab and an output power of 213 W at 1064 nm was demonstrated [FWB+04, FWKF05]. This prototype was chosen to be the basic design for the aLIGO observatory systems. As intermediate step an engineering model of the laser was developed and tested in Hannover [Põl09] before the setup of the systems that were delivered to the LIGO sites started. The technical details of the systems are reported in [WPK+11, Win12, Pun11]. In the following the laser system is briefly described.

[2]The laser requirements are listed in [WKSF11].

As shown in Figure 3.1 the high power generation for the aLIGO laser is split into three stages. Due to the monolithic design and its low noise properties, a 2 W non-planar-ring-oscillator (NPRO) (Mephisto 2000 NE LIGO, Innolight) was chosen as master laser [KB85]. The NPRO beam is further amplified to 35 W by a four stage Nd:YVO_4 amplifier [FSW+07].

To provide more than 200 W the third stage consists of a high power ring oscillator that is injection locked to the 35 W laser. The HPO itself has four laser heads with Nd:YAG crystals and generates more than 170 W output power, but without a seed laser there is no preferred direction for the emission of photons and hence laser light is traveling in both directions towards the NPRO and towards the IFO. A Faraday isolator protects the seed laser from the beam traveling back towards the NPRO.

Due to polarization dependent elements in the beam path towards the IFO the output beam of the HPO needs to be linearly polarized. Therefore a Brewster plate inside the ring oscillator increases the loss for one polarization direction below the laser oscillation threshold.

Seven laser diodes with a wavelength of 808 nm are combined to pump each of the four laser heads with a total power of approximately 250 W each. The conversion efficiency from pump light at 808 nm to laser light at 1064 nm is on the order of 30 %. This is due to the quantum defect, optical losses and thermal effects in the laser crystal. Since 70 % of the pump light are transferred to heat one major problem is the cooling of the laser crystals. For the aLIGO HPO the laser crystals are housed in a chamber and a turbulent flow of water is surrounding them. Thus the cooling is very efficient, but at the same time water turbulences create vibrations of mechanical parts that increase the noise on the laser table (Sec. 3.1.4, 5.4.1).

In order to keep the HPO length stable one mirror in the resonator path is mounted on a piezoelectric transducer (PZT) which is itself attached to a DC translation stage. Thus fast length fluctuations can be compensated with the PZT and slow length changes with the DC translation stage, called long range actuator (LRA). While the PZT has a range of approximately 5.5 µm, the LRA range is several millimeters.

The 35 W laser seeds the HPO and if the resonance frequency of the oscillator matches the seed laser frequency the HPO will be forced to adopt the frequency noise properties of seed laser. Additionally, the HPO will be forced to mainly emit photons into the direction of the seed laser beam. This technique is called injection locking and similar to an effect first observed by Huygens, who recognized that two clocks very close to each other eventually run synchronous. This underlying principle works as well for other type of oscillators including lasers [Zaw03, Sie86, Chap. 29].

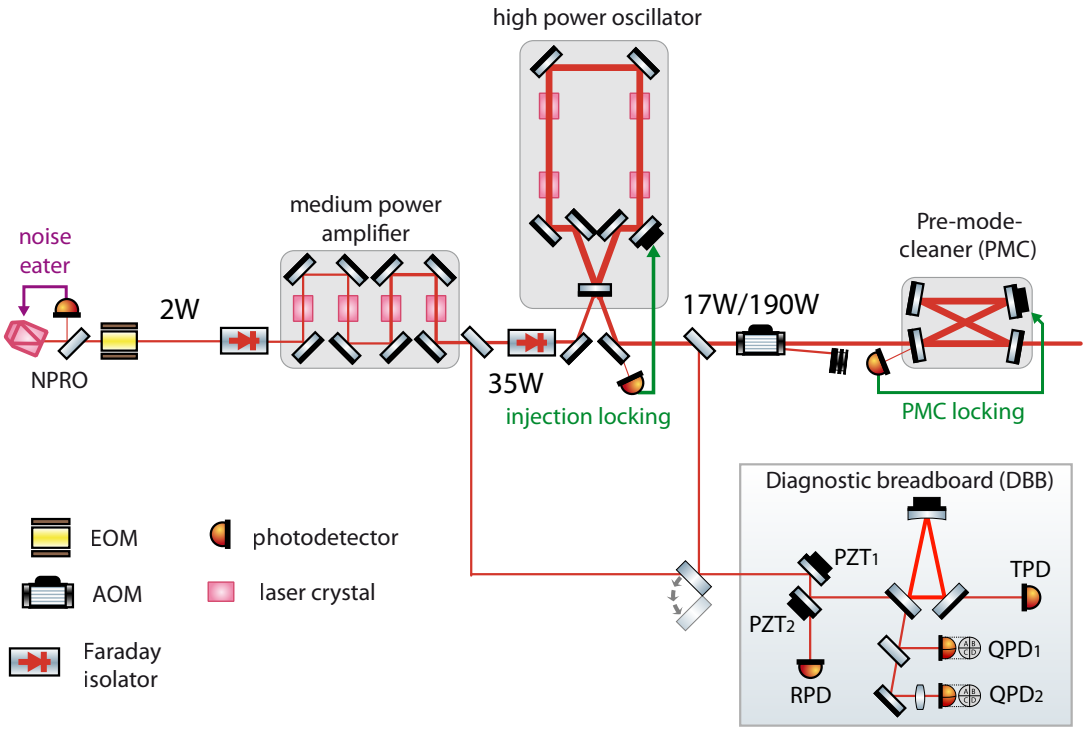

Figure 3.1: Schematic of the aLIGO laser, diagnostic breadboard and Pre-Modecleaner. The high power beam is generated by a 2 W NPRO that is amplified to 35 W and then injection locked to the high power oscillator. The injection locked system is capable of producing more than 200 W of output power in a nearly diffraction limited beam. Further temporal and spatial beam filtering is applied by the PMC. The DBB is used for beam characterization.

To ensure a robust long term stability the slave laser needs to track the frequency of the master laser to stay in the injection locking range. This is implemented by a Pound-Drever-Hall (PDH) locking scheme [Bla01, DHK+83] that uses a feedback control loop which actuates the length of the HPO, while tracking the phase of the master laser. Injection locking the two lasers has the benefit that the high power generation in the slave laser can be separated from the low noise design of the master laser and the output beam still has the noise properties of the master laser.

The drawback of this configuration is that the laser output power cannot be continuously adjusted. If the high power oscillator is switched off, the output power of the system is 17.5 W because 50 % of the light is transmitted towards

the incoupling mirror of the oscillator and blocked. This configuration is called low power mode (LPM) of the laser. In principle it is possible to put an additional HR mirror in the beam path such that 35 W are directed to the IFO.

When the high power stage is enabled the injection locked system produces up to 220 W. However, as further resonators which are part of the GWD only support light in the fundamental Gaussian mode, an aperture at the output of the high power oscillator blocks light emitted into a corona around the main beam and hence the power that can be used for the main experiment does not exceed 190 W. This configuration will be referred to as high power mode (HPM).

Acoustic enclosure

The chiller and the pump diodes are housed in a dedicated room separated from the area where the low noise experiments take place. Optical multimode fibers guide the pump light to the laser room.

The laser system is located in a class 1000 cleanroom. It is very important that the laser is in a clean environment as particles in the beam path and on optical components lead to scattering and thus reduction in the beam quality. In some cases particles can permanently damage the optics.

To prevent vibrations due to acoustic excitations, the cleanroom walls were designed such that they also act as an isolating acoustic enclosure. The laser room is connected via a sealed pipe to the viewport of the first vacuum chamber.

fan filter units (FFUs) in the ceiling of the laser room ensure frequent air exchanges and filtering through high-efficiency particulate absorption (HEPA) filters. However, these FFUs are only enabled when personnel are inside the laser room as they cause noise via vibration and air currents.

3.1.3 Laser diagnostics and interlocks

For the characterization of the laser, to ensure long term stability and to implement safety interlocks, continuous monitoring of many laser parameters is required. Therefore photodetectors are installed to monitor power levels at different locations and to sense the RF error signal for the injection locking. Furthermore flow sensors monitor the water flow of the cooling water and temperature sensors are installed to keep track of the temperatures of the laser diodes.

The photodetector design is customized such that the noise properties can be individually optimized. Four types of PDs are used in the aLIGO laser. For the injection locking, a fast PD with a bandwidth of more than 80 MHz is used. The power monitoring is done with 3 mm indium gallium arsenide (InGaAs) PDs for the 1064 nm light and silicon PDs for the pump light. To measure power

noise PDs with a high quantum efficiency such as 2 mm Excilitas InGaAs PDs are used.

Due to the complexity of the high power laser (HPL) the data from many sensors are used to control interlocks. There are power watchdogs that monitor the output power of the system and shut it down in case it drops below a predefined value. Since the cooling water is essential to protect the system from overheating a loss of cooling water flow shuts the system down immediately.

Diagnostic Breadboard

While monitoring power levels and water flows happens continuously, the diagnostic breadboard (Figure 3.1) is a device that is placed outside the laser box for further diagnostics. It has the capability to characterize important properties of the laser beam such as power noise, frequency noise, pointing noise and higher order spatial mode content using a 135 mW pickoff. Most of the measurements utilize the three mirror ring cavity with a finesse of 365 and a free spectral range (FSR) of 715 MHz. A detailed description of the DBB is given in [KSWD07]. Both a fraction of the HPO output and the 35 W laser output can be analyzed individually. Due to regular DBB measurements at the LIGO sites, a robust long term behavior of the laser system can be assured.

Besides other measurement methods the modescan technique was found to be the most accurate way to determine the higher order spatial mode content of a laser beam [KSWD07]. The decomposition of the test beam into a set of cavity modes, for example Hermite-Gaussian (HG) modes, is done by a variation of the resonator length of the DBB. Since most of the higher order modes are not degenerated due to the round trip Gouy phase [Sie86] of the resonator, the power in the modes can be determined from the signal of the PD in transmission of the resonator. The fundamental mode content of the test beam is specified as the ratio of power in the fundamental mode divided by the total power of the beam.

As an example Figure 3.2 shows the modescans of the HPL at the LIGO Livingston Observatory site and the Reference System in Hannover. Although the modescan was found to be the most accurate technique to characterize the higher order mode content of a test laser beam, the measurement just reveals an upper limit due to the fact that there are only spherical lenses to mode match the test beam to the DBB resonator. Hence, ellipticity and astigmatism of the beam cannot be compensated and appear to first order as HG_{20} and HG_{02} modes. In Figure 3.2 the position of other higher order HG modes are marked for further reference. The results of the modescans will be discussed in the following Section 3.1.4.

Due to a fundamental symmetry breaking of three mirror resonators and

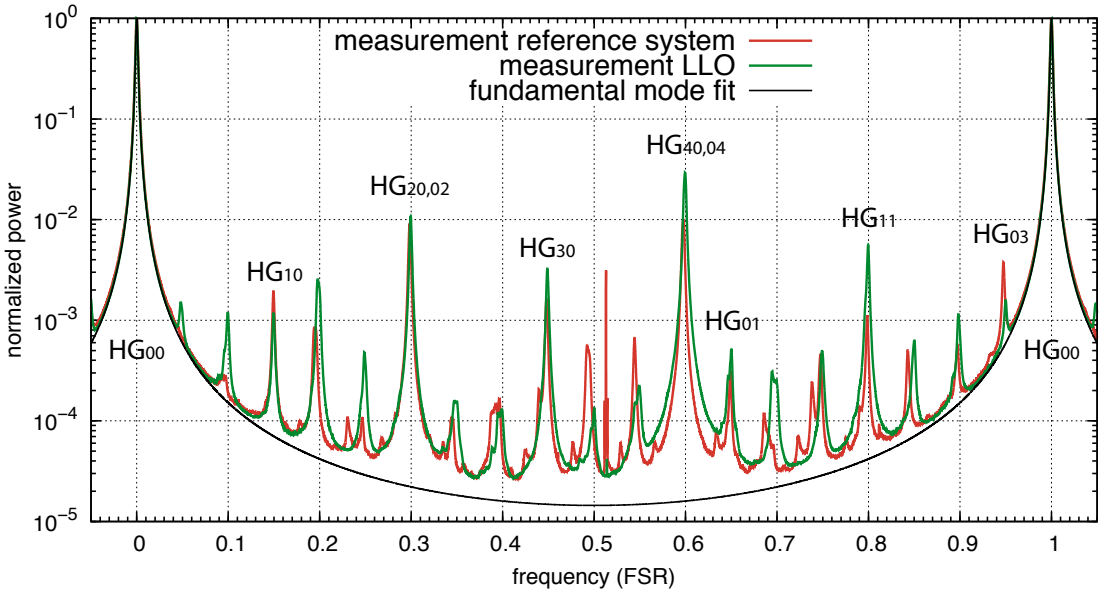

Figure 3.2: Modescan of the high power laser. The laser beam can be decomposed in higher order spatial HG modes by analyzing it with the DBB resonator.

since the reflectivity of the mirrors and their penetration depth is different for a beam in vertical and horizontal polarization, a sharp peak appears almost in the middle of the FSR for light in vertical polarization with respect to the resonator. During the installation at the LIGO sites an additional polarizer was added in front of the DBB to suppress the peak in the modescan caused by light in the vertical polarization.

To determine the power noise for Fourier frequencies up to 100 MHz, a PD upstream of the DBB resonator detects 50 mA photo current. This leads to a shot noise limited sensitivity of $2.5{\cdot}10^{-9}/\sqrt{\text{Hz}}$ RIN up to 60 MHz.

The frequency noise of the test beam can be determined by measuring frequency fluctuations with respect to one of the DBB resonator resonances while it is locked to the fundamental mode with a PDH scheme. Control and error signal are used to determine the frequency noise. The measurement relies on the assumption that the length noise of the resonator is lower than the equivalent frequency fluctuations on the test beam. To reduce this length noise the resonator is housed in a tank that serves as acoustic enclosure.

Moreover, the DBB can determine the pointing noise on the test beam. The spectrum of ϵ (Eq. 3.8) is directly measured for the two angular and two translational degrees of freedom. It can be directly obtained by using the resonator

eigenmode as reference and characterize the test beam with differential wavefront sensing (DWS) [MMRW94] on split PDs, which are two Rayleigh ranges apart from each other and in reflection of the resonator.

All measurements are automated and the DBB is fully controlled by the control and data system (CDS).

3.1.4 Results of laser characterization

After the installation of the laser systems and stabilization a set of measurements was performed to inspect the stability of the systems. The results of the measurements are presented in this Section, the characterization of the beam downstream of the PMC with further stabilization is addressed in Chapters 4 and 5.

Operating the system in LPM it takes only a few minutes for the laser to warm up and reach its thermal equilibrium. In HPM operation, however, the HPO requires approximately five minutes until the injection locking to the 35 W laser works reliably. Nevertheless, resonator length changes that are compensated by the PZT occur with a linear slope within the first few hours of operation before leveling. Up to this point it is recommended to keep the LRA disabled to avoid an operation far from the LRAs reference point.

The unity gain frequency (UGF) for the injection locking control loop is limited by the PZT resonances of which the first one is at about 30 kHz [Win12]. Thus the injection locking servo is equipped with notch filters that are adjusted individually for every laser system. The control loop is robustly locked with a UGF of 10 kHz on all three systems. Enabling the LRA the system does not relock due to environmental temperature changes of more than 3 K which is above the expected temperature variation of the LIGO laser area enclosure [WPK+11].

As mentioned in Section 3.1.3 the spatial beam profile is determined by the modescan technique. Table 3.1 contains a list of the modescan measurements at various sites for the 35 W laser and the injection locked HPO[3]. The results are considerably different due to a number of reasons that can distort the measurement. First of all alignment and modematching of the test beam with respect to the DBB resonator have to be perfect. While a perfect alignment is always possible the modematching accuracy is restricted to a limited choice of lenses. The modematching was not fully optimized for the 35 W laser modescan at the Reference System. Secondly, there are different beam path from the amplifier and the HPO to the DBB of which the amplifier one contains several more optical components that can introduce additional pointing noise, ellipticity or astig-

[3]The errors given in table 3.1 are statistical errors. Other deviations, for example due to misalignment, are not included.

matism to the beam and mimic a worse spatial beam profile. Moreover, the HPO is equipped with an aperture at its output. Its diameter varies between 1.6 and 2.6 mm and is chosen during laser installation. A perfect beam alignment towards the aperture is essential to avoid diffraction. The best modescan results, namely the LIGO Livingston Observatory (LLO) amplifier and Reference System HPO measurement are compatible to the results that were achieved by measuring a single NPRO beam [KW08].

A comparison of the laser RIN was performed with the DBB as well and is depicted in Figure 3.3. Since the Reference System is not located in a dedicated room with acoustical shielding the environmental noise is higher than the one at the LIGO sites. Generally, the noise in HPM is higher at low frequencies which could be caused by a higher amount of scattered light that reaches the PD, although the PD was carefully shielded. At Fourier frequencies above 100 Hz the noise of the HPM reaches the same level as the noise measured in LPM. However, there are additional sharp peaks in the HPM spectra above 1 kHz. Besides the ones which are caused by electrical cross couplings at the mains frequency of 50 Hz in Europe and 60 Hz in the US and their harmonics, additional peaks appear due to mechanical resonances of components in the HPO. The relative power noise in LPM is dominated by fluctuations of the pump light and the NPRO power noise, which both are at the level of $1 \cdot 10^{-7}/\sqrt{\text{Hz}}$ to $1 \cdot 10^{-6}/\sqrt{\text{Hz}}$ [FSW+07, KW08].

Scattered light was found to be a problem in many power stabilization experiments and was already characterized for the Reference Systems power stabilization in [Bog13]. To further minimize scattered light a bolometer in reflection of the PMC was replaced with a silicon carbide (SiC) beam dump with very low back scattering and residual transmission through high reflective (HR) optics were blocked as well.

Power noise was also characterized for RF frequencies (Fig. 3.4). The noise caused by NPRO relaxation oscillation [Sie86, Chap. 25.1], which occurs at approximately 1 MHz. Above 1 MHz the NPRO power noise decreases with a f^{-2}

laser system	35 W laser	HPO	downstream of the PMC
Reference System	3.7%±0.07%	2.8%±0.1%	0.5%±0.01% (in HPM)
L1	2.4%±0.03%	5.3%±0.18%	
H1	4.2%±0.02%	5.4%±0.15%	

Table 3.1: DBB measurement of the higher order mode content for lasers at various locations. These numbers ca be considered as an upper limit for the higher order mode content as the laser beam could not always be perfectly modematched to the DBB resonator.

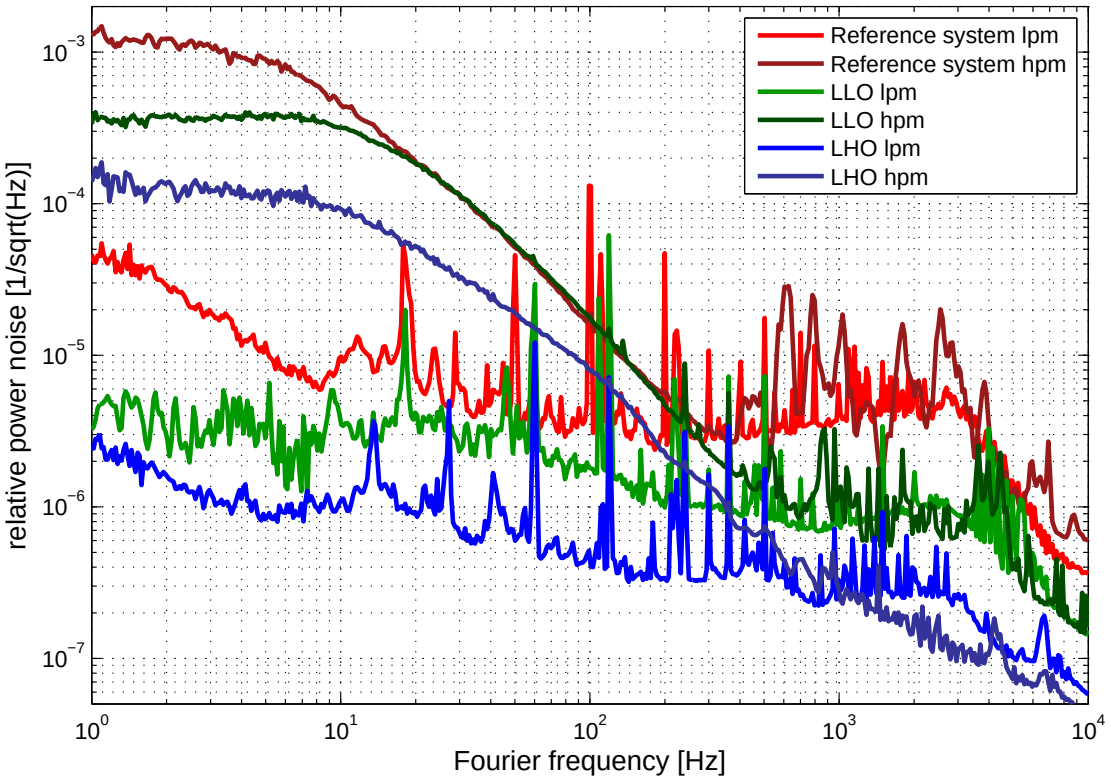

Figure 3.3: Comparison of laser unstabilized power noise in HPM and LPM. In HPM the noise level is increased could be due to scattered light which interferes in the measurement process. The noise in LPM is dominated by NPRO power noise and RIN of the pump light.

slope. There is additional filtering in HPM due to the passive power noise suppression of the HPO resonator [OVH+00]. Although seed laser power noise above half of the injection locking linewidth is not resonantly enhanced in the slave laser cavity, it is reflected at the input coupling mirror of the HPO and still present in the output beam [Zaw03]. The measurements are shot noise limited above 10 MHz in HPM and 20 MHz in LPM and electronics noise limited above 60 MHz. Residual amplitude modulation (RAM) at the phase modulation sideband frequency of 35 MHz is stronger by a factor of five in HPM. This might be caused due to a static offset in the injection locking control loop.

The advantage of the acoustic enclosure is most obvious by looking at pointing noise. Measurements of the pointing noise were performed when the LIGO Hanford Observatory (LHO) laser system was first installed in the H2 laser area enclosure and are shown in Figure 3.5. Vibrations of the FFUs and the air that is blown onto the table are the dominating noise sources up to Fourier frequencies

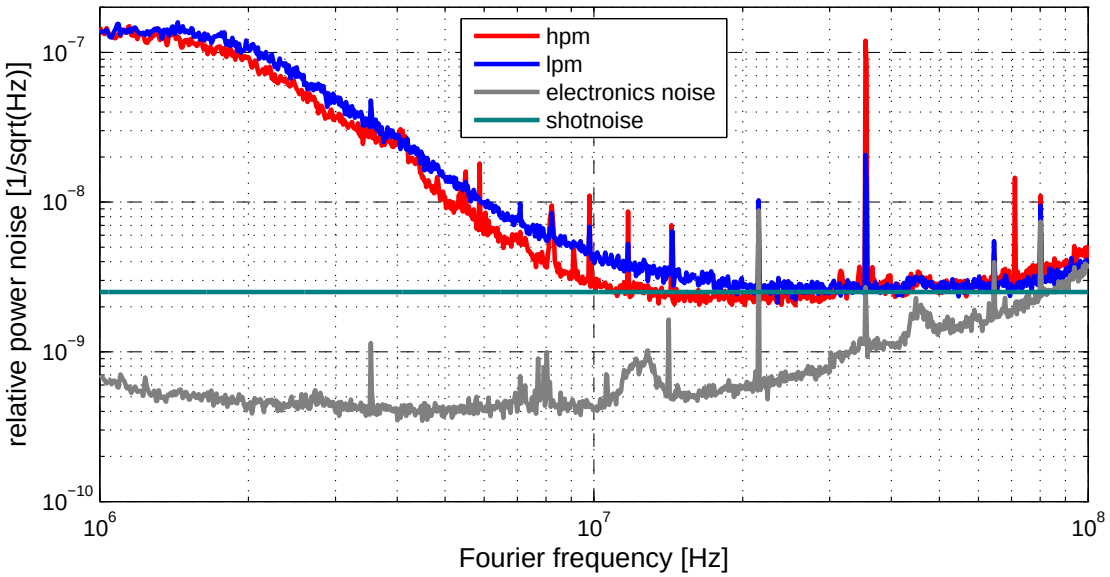

Figure 3.4: RIN measurement at radio frequencies in high- and low power mode at LLO. The measurement is shotnoise limited above 10 MHz (20 MHz in lpm) and electronics noise limited above 60 MHz. Due to the injection locking linewidth the HPO filters power noise at radio frequencies.

of approximately 200 Hz. Compared to the measurement with disabled FFUs the noise level at low frequencies is elevated up to one order of magnitude in HPM and more than two orders of magnitude in LPM. Some of the peaks in the 100 Hz to 1 kHz band are caused by vibrations of the cooling water that supplies the HPO even if the laser is operated in LPM. By a change in the water distribution the noise was further reduced as described in Section 5.4.1. Similar to the RIN measurement, peaks above 1 kHz only appear in the HPM measurement.

Compared to the data taken at the Reference System the pointing noise at LHO below 10 Hz is significantly reduced due to the shielding of the acoustic enclosure. However, in high power mode scattered light could limit the measurement at low Fourier frequencies, such that the noise reduction due to acoustic shielding covered in the measurement.

The frequency noise can also be measured with the DBB and follows the NPRO characteristics of $10\,\mathrm{kHz}/\sqrt{\mathrm{Hz}}/\mathrm{f}$ as measured in [KW08]. This is described in more detail in Chapter 5 in the context of frequency stabilization.

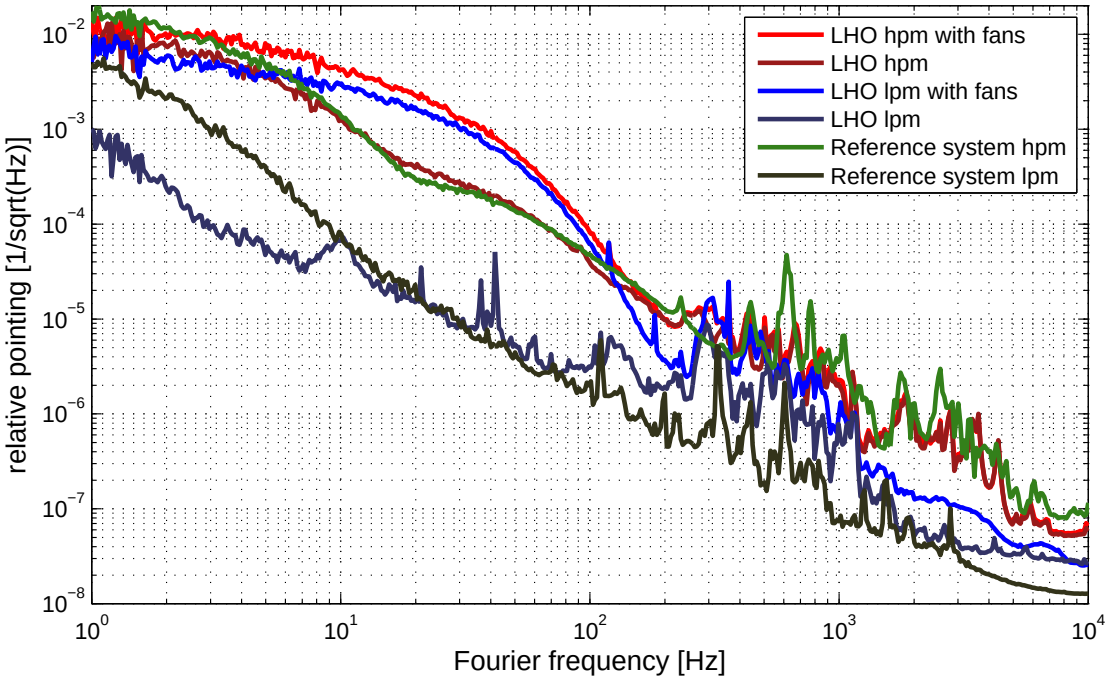

Figure 3.5: Comparison of pointing noise in LPM and HPM with fans enabled and disabled. These measurements were performed in the H2 laser area enclosure in December of 2011. The measurements in HPM could be limited by scattered light at low frequencies. In low power mode the benefit of the acoustic enclosure is apparent below 10 Hz, since the noise at LLO is up to one order of magnitude below the noise of the Reference System.

Long term stability

One major aspect in the design of the laser system was the long term stability and reliability. Regular DBB measurements are used to check the noise characteristics. The laser is continuously operating and only interrupted for occasional commissioning.

Although only a few watts of laser power are required in the early stage of the IFO commissioning the laser systems were operated for at least a few months in HPM. Thereby the robustness of the system was tested. Afterwards the lasers were operated in LPM without changing the internal alignment. Switching the laser on again after several months, the overall performance did not change considerably. Worries that the laser diodes show aging effects even if they are switched off could not be confirmed.

In Figure 3.6 the output power trends for the LLO laser and the Reference

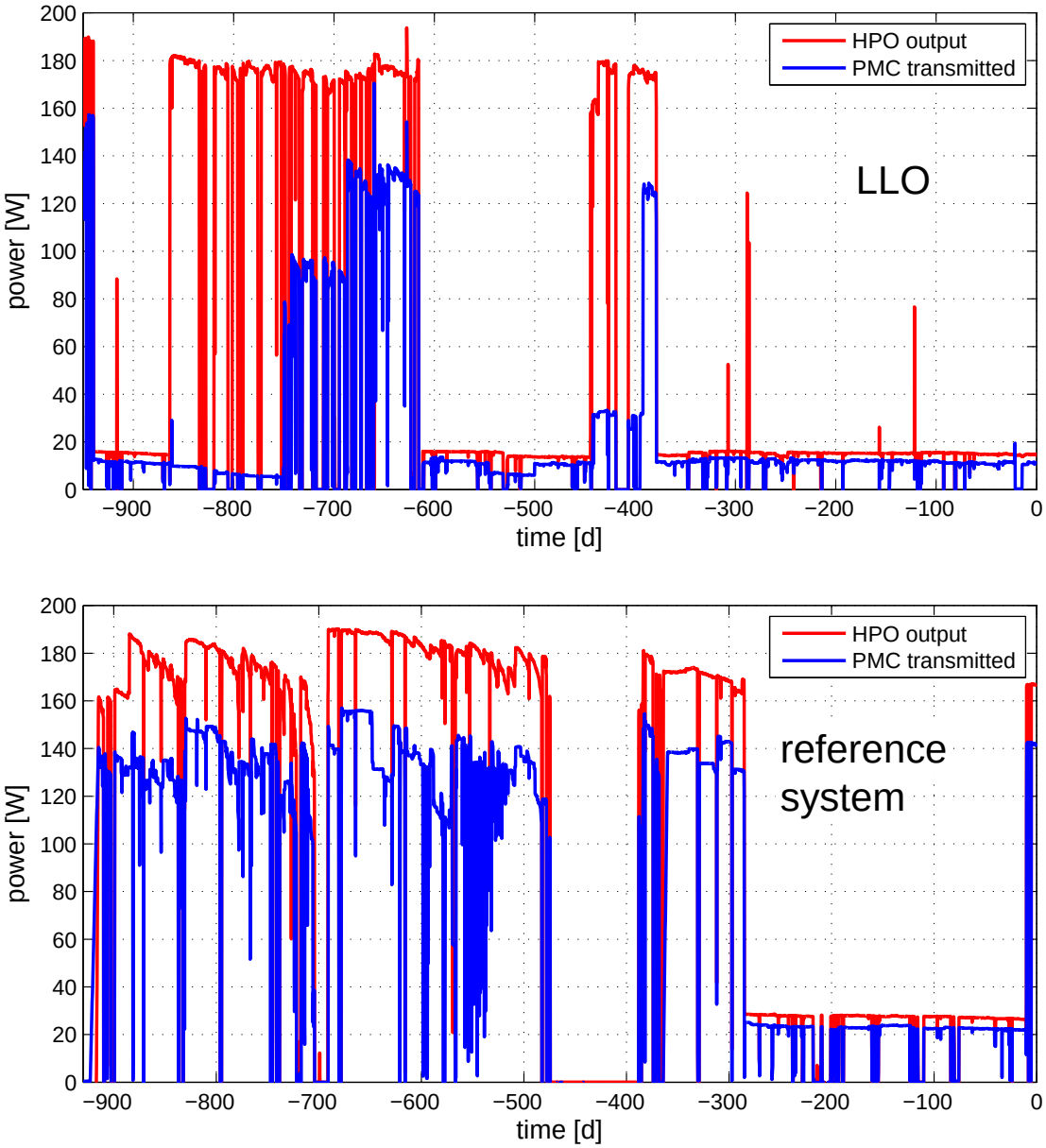

Figure 3.6: 900 day power trend from July 2011 to February 2014 for the LLO laser and Reference System. The behavior of the laser output power and the power transmitted through the PMC is displayed. It is possible to attenuate the light before it enters the PMC. Commissioning efforts particularly at LLO caused many power drops in the PMC trend due to relocks. Temperature changes in the laser enclosure impose alignment drifts resulting in a power decrease of the transmitted light through the PMC.

System are shown as well as the power transmitted through the PMC which will be addressed in Section 3.2.3. Each data point displayed in Figure 3.6 represents an one hour average of the power such that peaks between the power levels of 17 W and 160 W are instances where the HPO operated for a very short time. Overall there is only one major downtime for the Reference System which is due to a laser diode box that needed to be replaced[4]. There are more short downtimes of the LLO laser due to site power outages that occurred during heavy weather.

Laser diode degradation

It is the goal to operate the laser at the optimum working point. Hence, the power that is provided by the pump diodes should be kept constant and consequently the thermal lens in the laser crystal does not change. Due to aging the pump diode power degrades over time and this effect is compensated by increasing the current and adjusting the temperatures for the pump diodes. All four HPO diode boxes are equipped with seven pump diodes that could produce in total 315 W. Derating the current such that the output power is reduced by 20 % helps to increase the lifetime of the diodes. An 35 W laser diode box contains four laser diodes, which are derated as well.

Laser diode currents and output power are shown in Figure 3.7 for the Reference System. When the diode box is new, there is no need to adjust the current for a long time. At the end of the lifetime it is necessary to increase the current once per week. The average lifetime[5] of the HPO diode boxes is 12000 hours, the 35 W laser diode box need to be refurbished approximately every 12800 hours.

3.1.5 Future development

Although the second generation of GWDs is not fully commissioned yet, designs for laser systems with possible application in third generation GWDs are discussed. There are three main aspects that are considered. At first a more compact design, secondly a laser power increase and the third aspect is switching to a different wavelength.

So far large scale interferometric GWDs have been operating with solid state lasers, but the rapid development in the field of high power fiber laser systems make them a promising candidate as light source for the next generation of GWDs. Advantages of fiber lasers are the compact design and in case of an all

[4] At the LIGO sites a diode box swap can be done in a day. Due to a lack of laser diodes there was a long, scheduled downtime for the Reference System.

[5] This includes the data from five samples of each type of diode box.

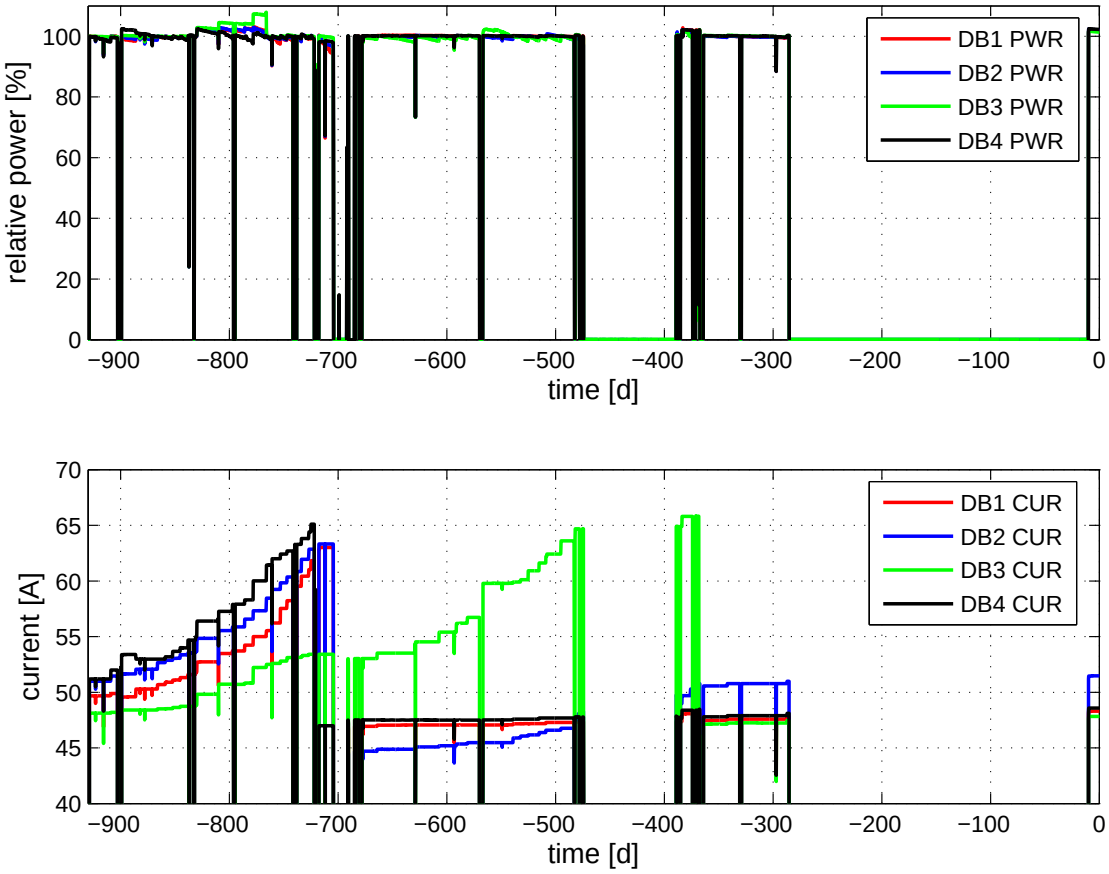

Figure 3.7: Relative power level of the Reference Systems diode boxes and corresponding currents. The diode box currents are raised to keep the output power at the optimum working point when aging effects occur in the pump diodes. A refurbishment of the diode boxes is required when the maximum current of 65 A is reached.

fiber system there is no need for any laser realignment after the system is set up. A 300 W fiber laser with the same design parameters as the aLIGO laser has been developed [TSNK12] and is currently in a long term test. In Advanced VIRGO a 100 W fiber laser system will be implemented [GBM+10].

To increase the laser power further while keeping properties such as single spatial mode and single frequency operation has been a problem for many years in fiber- and solid state laser development. This is mostly due to non-linear effects in case of fiber lasers and thermal effects as well as aberrations in case of solid state lasers. An alternative approach is to coherently combine two or more lasers to increase the output power. A table top experiment performed by the author of this thesis with a coherent combination of two fiber amplifiers

demonstrated an output beam with a combining efficiency of more than 95 % with 97 % fundamental mode content at 21.3 W [TPN+11, Tün13]. Other experiments using the same technique scaled the output power up to 1.4 kW [Flo11].

Since current and future gravitational wave detectors are quantum noise limited an increase of laser power does not increase the sensitivity over the entire measurement band as radiation pressure noise (RPN) also increases with higher laser power [Sau94]. In the design study for the Einstein Telescope (ET) [Tea11], a proposed European third generation detector, two types of IFO are planned. The first one operating at 500 W which improves the sensitivity at high frequencies and a second one with a 3 W laser at 1550 nm wavelength that provides a good sensitivity at low Fourier frequencies. Changing the laser wavelength to 1550 nm is required when silicon test masses are used which is advantageous in a cryogenic environment to further reduce the influence of thermal noise.

3.2 Pre-Modecleaner

The laser output beam is transmitted through a resonator called Pre-Modecleaner [WUG+98]. It is responsible for filtering the spatial beam profile and acts as a passive filter for power and frequency noise above the cavity pole frequency. Furthermore it suppresses pointing noise [RSS+81]. Another advantage of the PMC is, that its eigenmode sets a stable geometric reference for the beam paths on the laser table. Thus in case the laser needs to be realigned the output beam only needs to be matched to the cavity eigenmode.

Design considerations of the PMC are discussed in Section 3.2.1 and the control loop explained in Section 3.2.2. The performance of the different PMCs built for aLIGO is evaluated in Section 3.2.3 and two methods to determine a Gouy phase shift due to thermal effects are discussed in Section 3.2.4.

3.2.1 Design

The PMC is a bow-tie shaped, four mirror resonator with a round trip length of 2.02 m and therefore a FSR of 149 MHz. Three mirrors are glued to an aluminum spacer and the fourth mirror is attached to a PZT which is then glued to the spacer (Fig. 3.8). The size of the spacer is 507 mm x 160 mm x 80 mm and inside holes with a diameter of 13 mm are drilled. All mirrors are tilted by 5.6 degree around the vertical axis with respect to the input beam. The first prototype of the aLIGO PMC was characterized in [Põl09].

Acoustic excitations causing fluctuations in the resonator roundtrip length are suppressed by placing the PMC inside a pressure tight tank (Fig. 3.8). It is clamped in place with rubber in between the spacer and the tank. The tank

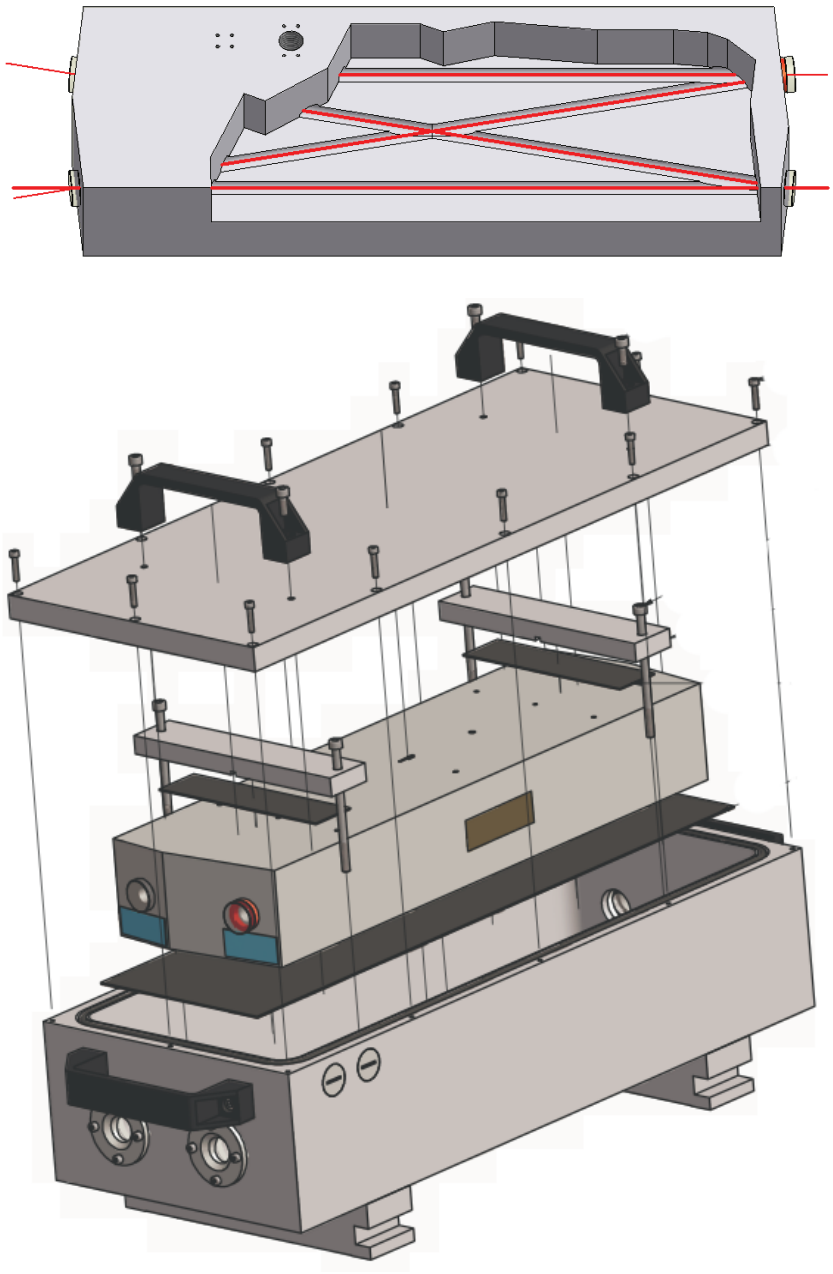

Figure 3.8: *top*: Sketch of aluminum PMC spacer and beam path. Three mirrors are glued directly onto the spacer. A PZT is placed between the fourth mirror and the spacer that is used as actuator for the length stabilization control loop. *bottom*: Assembly of PMC, which is clamped in the pressure tight tank. Rubber pads isolate the PMC from its surrounding. The PMC is equipped with heat pads on both side for length actuation by thermal expansion of the spacer and has BG39 filter mounted near the mirrors to block reflections from the tank windows.

is equipped with wedged, AR coated windows that are mounted under a 15 degree angle, such that parasitic beams, caused by residual reflections of the windows, are not aligned with the main beam axis.

There are two flat mirrors with a transmission of 2.4 % that are used as in- and outcoupling mirrors for the main beam. The other two mirrors are curved with a transmission of 68 ppm and a radius of curvature (ROC) of -3 m, which yields two beam waists. One waist is in between the flat mirrors with a radius of 548 μm and the other in between the two curved mirrors with a radius of 712 μm. In contrast to the prototype PMC the transmission of the curved mirrors was increased from 3 ppm to 68 ppm, because the stabilization downstream of the two ports requires more power than assumed at first.

For resonator length adjustment the PZT can be driven with a high voltage of up to 382 V that results in a round trip length change of 2.4 μm. However, this is not enough to compensate elongations of the spacer due to long term temperature drifts and effective optical path length changes caused by air pressure drifts. Hence, two heater pads are mounted to the spacer that are able to thermally extend the spacer by several hundred micrometers.

The finesse of the PMC is 129 and the pole frequency of 578 kHz respectively. Above the pole frequency the resonator acts as passive low pass filter for power and frequency fluctuations. This is important for the signal to noise ratio (SNR) of RF phase modulation sidebands at several MHz that are imprinted on the beam downstream of the PMC.

The round trip Gouy phase is 1.75 rad which corresponds to 0.28 FSR. Accordingly the power in the HG_{01} and HG_{10} modes are suppressed by a factor of 3969 which yields a pointing noise suppression of 63 [Mue05, KSWD07]. A circulating power of 6 kW is reached with an input beam power of 150 W and a peak intensity of $1.7 \cdot 10^{10}\,\mathrm{W/m^2}$. Other resonators had not shown a long term degradation due to a damage of the optics caused by similar intensities.

Finite element analysis of Pre-Modecleaner

For the characterization of noise it is important to know the resonance frequencies of certain components. A finite element analysis was performed to determine the mechanical resonance frequencies of the PMC spacer. Although the PMC is mounted inside the tank the simulation was done with the aluminum spacer in an unconstrained environment. This is a very general approach, as neither the exact material properties of the rubber that the PMC sits on nor the torque that is applied to the clamps was well known.

Table 3.2 contains a list of mechanical resonance frequencies up to 10 kHz. Even if those might shift in case the PMC is clamped inside the tank, adding more constrains will shift the resonance frequencies to higher values. Two of

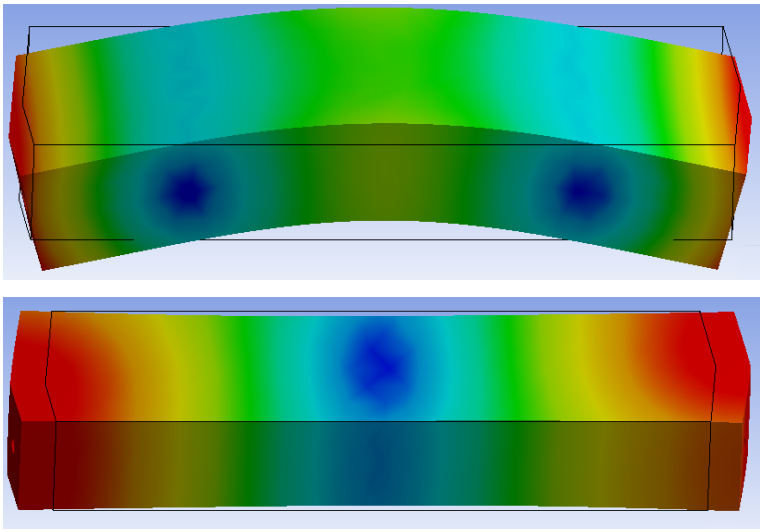

Figure 3.9: Two resonant modes derived from the finite element analysis of the PMC spacer. The upper mode has a resonance frequency of 1522.5 Hz and the bottom one 5026.6 Hz.

these modes are shown in Figure 3.9. The top mode has the nodes roughly at the location where the clamps are (Fig. 3.8) such that clamping the PMC will not improve the suppression of this mode. The picture on the bottom shows a mode where the whole spacer is stretched and contracted in the beam direction. This mode will have most impact on the round trip length and might be as well excited by the PZT.

The rubber that is used for clamping in between the aluminum parts will improve the damping of the mechanical resonances.

Mode	Frequency	Mode	Frequency	Mode	Frequency
1	**1522.5 Hz**	6	**5026.6 Hz**	11	9085.6 Hz
2	2302.4 Hz	7	5357.9 Hz	12	9397.6 Hz
3	2592.8 Hz	8	6354.4 Hz	13	9719.2 Hz
4	3713.5 Hz	9	6963.2 Hz	14	9778.8 Hz
5	4609.7 Hz	10	8242.1 Hz	15	10273 Hz

Table 3.2: Table of resonance frequencies of unconstrained PMC spacer up to 10 kHz.

3.2.2 Control loop

In a Pound-Drever-Hall scheme the PMC length is locked to the laser frequency via a feedback control loop as shown in Figure 3.1. The phase modulation sidebands that are required for the PDH locking are produced by the EOM downstream of the NPRO. The sidebands are reflected from the HPO because they are outside the cavity linewidth such that the sideband strength at the PMC is halved when the HPO is switched off due to the 50 % reflectivity of the HPO incoupling mirror. However, in addition to this effect the SNR on the PMC locking PD is considerably better in LPM, because the carrier amplitude is about a factor of 10 weaker resulting in a 10 times less attenuation of the beam in front of the PD. Furthermore switching laser power modes adds 180 degree of phase to the error signal, because the carrier signal is either reflected at the HPO incoupling mirror or at the apparently overcoupled HPO. An offset in the injection locking control loop spoils the PMC PDH error signals because the phase modulation sidebands are not symmetrically around the carrier any more.

The PMC locking is done with analog electronics to achieve a high UGF. It contains an automated locking logic that is changing the resonator length. When the PMC is on resonance with the laser frequency the feedback control is enabled. After a lock loss the logic is able to acquire lock within 65 ms (averaged value). The speed of the length control loop is limited by mechanical resonances of the PZT, which are at approximately 30 kHz. A notch in the servo electronics is adjusted for each PMC individually to suppress the first PZT resonance.

Once the PMC is locked a slow, digital loop controls the spacer temperature via the heater pads such that the PZT is kept in the middle of its dynamic range. The heater control loop UGF is about 0.3 Hz.

Figure 3.10 displays the control loop transfer functions of the PMCs at the various sites. The measurements for LHO and the Reference System are similar and they both reach a UGF of 8 kHz with a phase margin of 76 and 55 degree respectively. However, the LLO loop gain is limited due to a resonance that had been at 8 kHz after the pre-stabilized laser (PSL) installation and looking at the same measurement over a two year period of time the feature shifts dynamically towards lower Fourier frequencies.

Installing a notch filter for the resonance a UGF of 2 kHz is still achievable, but with a very small phase margin of 13 degree. At the moment it is unknown what the reason for this behavior is. It could be an undamped resonance of the PMC spacer that shifts due to a changing force applied by the clamps, but so far there is no indication for an issue like this. Another possible explanation could be a change in the stiffness of the PZT material due to improper glueing or mechanical failures.

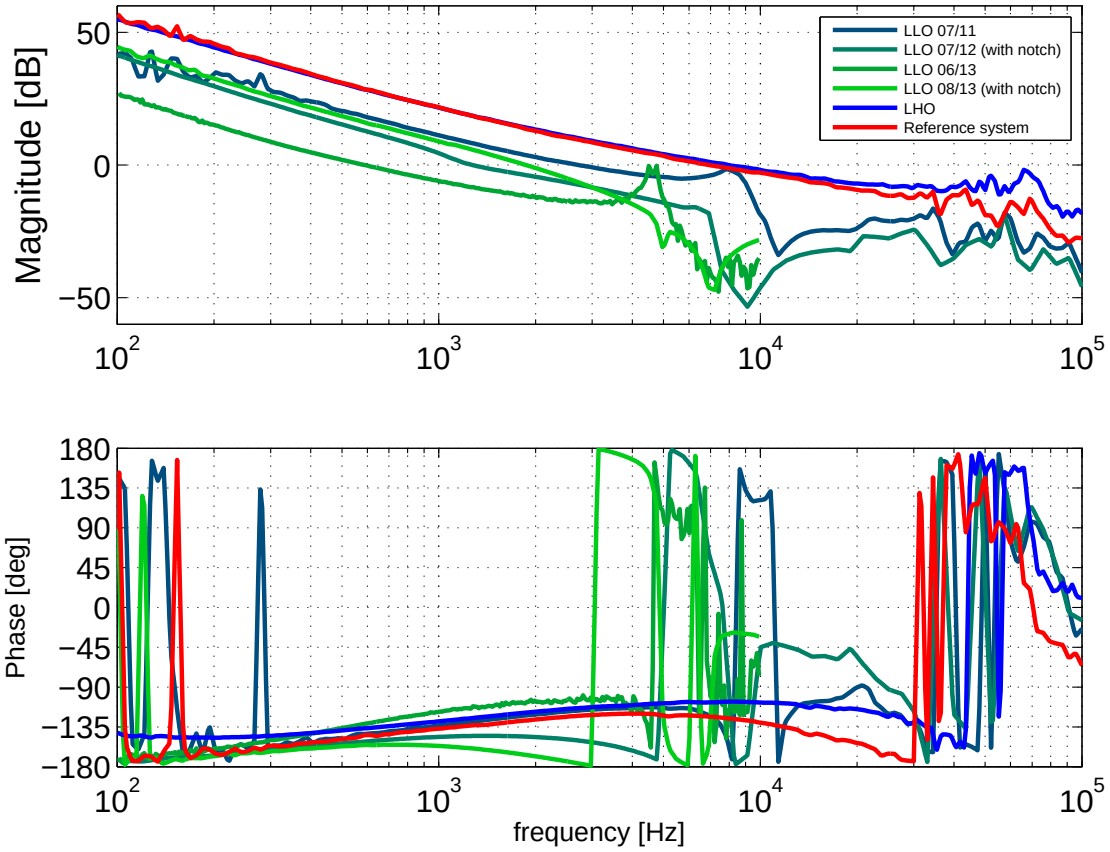

Figure 3.10: Transfer functions of PMC control loops. While the Reference System and LHO measurements look similar with a UGF of 8 kHz the LLO one has a resonance in the kHz regime that is dynamically shifting. Therefore the UGF is only 2 kHz with a phase margin of 13 degree.

3.2.3 Performance of PMCs

For the aLIGO project seven PMCs were built and characterized in total. The measured results are compared to the simulated ones in Section 3.2.1. Table 3.3 shows the results from the characterization. From the finesse and Gouy-phase measurement and static values like resonator round trip length many other parameters can be deduced. This includes internal power buildup, resonator pole frequency, total internal losses, ROC of the mirrors and waist sizes. Apart from that the beam position on every mirror was measured to verify that the eigenmode is not clipping inside the resonator.

The results of the finesse measurement are in accordance with the simula-

tions. Instead of 129 the average value for the finesse is 130, while 136 is the highest and 125 the lowest value that has been measured. The pole frequency varies accordingly between 548 kHz and 596 kHz.

The Gouy phase, however, is much lower than expected. The simulation predicted a Gouy phase of 1.75 rad and the measurement average is 1.7 rad or 0.271 FSR. Most likely the ROC of the two curved mirror deviates from the target specification. A Gouy phase of 1.7 rad corresponds to -3.15 m ROC which in turns leads to waist sizes of 561 µm and 715 µm. The Gouy phase for the first prototype PMC that is equipped with curved mirrors from another batch of substrates was 1.72 rad and therefore already smaller than the specified ROC.

The filter effects of the PMC were characterized in [KBD+12, Põl09] and are summarized here. The output beam of the PMC of the Reference System was measured with a second DBB and an upper limit for the higher order mode content of 0.5 % was obtained. A power noise suppression of 21 dB at 9 MHz was verified and determined by the use of the optical AC coupling technique [KWD08] that made it possible to measure a corresponding power noise level as low as $2{\cdot}10^{-10}/\sqrt{\text{Hz}}$. At the Reference System the pointing noise suppression is hard to determine at low Fourier frequencies because of environmental disturbances. The expected pointing noise suppression of 63 could be confirmed for Fourier frequencies of 20 Hz and higher.

Frequency noise is as well filtered above the PMC pole frequency, but can also contribute frequency noise (Sec. 5.2). Figure 3.11 shows a frequency noise measurement from the acquired PMC control and error signal at the Reference System. During the measurement the frequency stabilization servo (FSS) was operating to guarantee that the laser frequency noise is not the dominating noise source. Compared to a typical NPRO frequency noise, the noise caused by PMC

[6]Spacer with other S/Ns were fabricated, but not equipped with mirrors.

PMC S/N[6]	finesse	Gouy-phase [FSR]
002	133	0.271
005	135	0.271
008	125	0.272
009	136	0.274
010	125	0.271
011	125	0.272
012	134	0.268
average	130	0.271

Table 3.3: List of measured finesse and Gouy phase values for the PMCs that were produced for aLIGO.

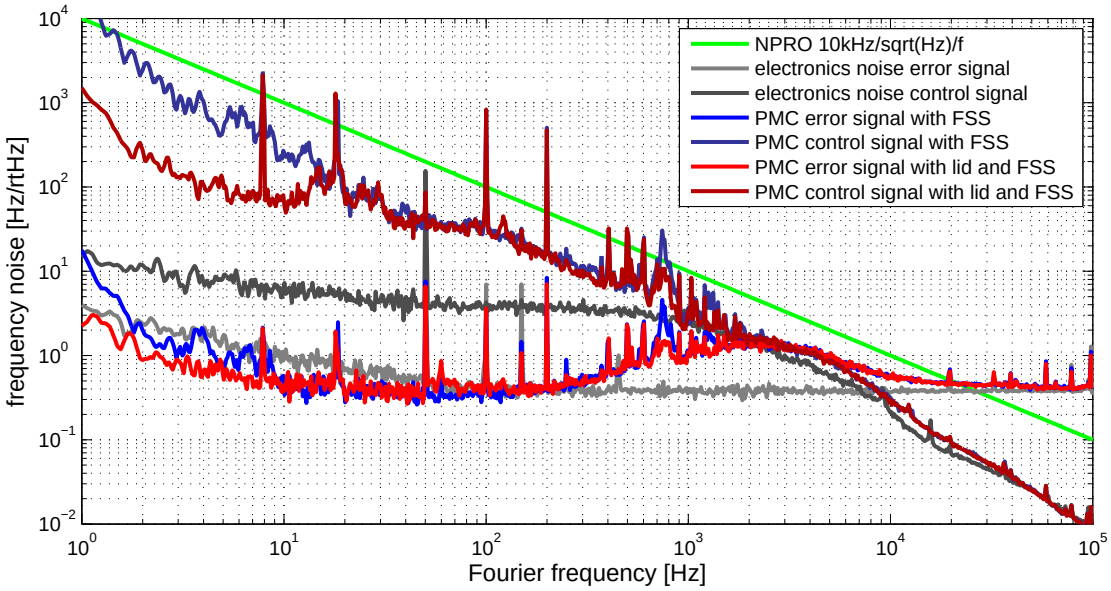

Figure 3.11: Measurement of the length noise of the PMC. The laser frequency noise during the measurement was reduced by a separate control loop. If the lid of the acoustic housing is removed the length noise increases at low Fourier frequencies.

length fluctuation is below the NPRO trace up to Fourier frequencies of 20 kHz, except for a few peaks from 400 Hz up to 2 kHz. Above 10 kHz the measurement is electronics noise limited.

The origin of the peaks are probably due to vibration of mechanical components either of the PMC itself or on the beam path towards it, which are imprinting phase noise at their resonance frequencies. While the results of the finite element analysis in Section 3.2.1 did not indicate that the peaks below 1.5 kHz are from the PMC spacer, they could be caused by the tank which has resonance frequencies as low as 650 Hz.

In a second measurement the noise contribution of the PMC in a tank with closed and opened lid was investigated. With the lid open the length noise deteriorates considerably at low Fourier frequencies and an increase of a peak at 750 Hz by more than a factor of two is observed. The unstabilized laser frequency noise is further characterized and discussed in Chapter 5.

The beam path towards the PMC is only equipped with spherical lenses. Thus a mismodematch due to ellipticity and astigmatism cannot be compensated. The power in transmission of the PMCs at the Reference System and LLO is shown in Figure 3.6. Without changing the state of the laser and because of the robust configuration of the feedback control loop the power in transmission of

the PMC is stable for a long time. However, it does not exceed 160 W, which is an indication that a fraction of the power is lost on the way towards the PMC or is distorted by optical elements in the beam path. More than 20 W difference in the laser output power compared with the transmitted power is more than expected from the modescan measurement. However some power is diffracted by the power stabilization acousto-optic modulator (AOM) as described in Chapter 4. At LLO the transmitted power is sometimes below 20 W even though the laser is in HPM. In this case the light is attenuated directly at the output of the laser.

Long term power degradation

Observations at LLO revealed that the power of the beam reflected from the PMC window increased several watts after operating the PMC for nine month most of the time in LPM. Inspecting the window under a microscope showed residuals on it at the location where the beam enters and leaves. It did not appear to be a permanent damage as the residuals could be cleaned off the window with alcohol. These residuals were found on the input and output window, whereas the two windows at the monitoring ports did not show any contamination. Moreover, it was also found on the anti reflective (AR) surface of the flat PMC mirrors.

The PMCs at LHO and the Reference System showed the same characteristic. However, the effect was less evident as the system at LHO was not operating for such a long time and the lid of the Reference Systems PMC had been frequently opened due to commissioning activities.

Recognizing that the issue seems to be less severe if the PMC tank is open, one plausible explanation is that there is an outgasing material inside the PMC tank and photochemistry in conjunction with the strong laser beam occurs. This effect could increase the reflectivity of the optical surface.

Despite the contamination on the AR surface of the optics the losses inside the PMC did not increase significantly. A finesse measurement confirmed no change compared to the data taken after the PMC was built. According to the simulations, a change lower than 0.1 % for the absorption inside the resonator can be observed with the available precision of the finesse measurement.

Fourier transform infrared spectroscopy (FTIR) analysis of the contamination on the window surface was performed. The result did not show any aliphatic hydrocarbon.

Since the performance of the PMC without the lid did not get significantly worse inside the laser area enclosure the PMC tank was left open, such that outgasing substances do not accumulate in the pressure tight tank. In this configuration the PMC windows and mirrors did not show an increasing reflectivity

while operating more than a year.

3.2.4 Thermal lens analysis

The suppression for higher order spatial modes depends on the Gouy phase of the resonator, since higher order HG_{mn} have an additional phase of (m+n)ζ [KTAAM07] and ζ describes the Gouy phase that the beam accumulates during one resonator roundtrip. Hence, there is nearly no suppression for $\Phi_{rt} = (m + n)\zeta \approx 2q\pi$ (Eq. (3.18)) with q being an integer number. Furthermore, the Gouy phase depends only on the resonator geometry, such as round trip length and ROC of the curved mirrors.

For the PMC design simulations were done to make sure that the round trip Gouy phase is such that higher order HG modes with mode orders less than 15 are well suppressed. Due to the aperture inside the PMC clipping losses increase with the mode number and therefore modes with a high mode order are suppressed anyway. A round trip Gouy phase of 1.75 rad was chosen as result of the simulations. However, the results of the PMC characterization (tab. 3.3) revealed that the Gouy phase is lower, which is most likely because the ROC of the curved mirrors is higher than the design specifications. Consequently, modes of fourth order experience an additional phase shift close to 2π if the resonator is resonant for the fundamental Gaussian mode.

Since the intensity inside the PMC is very high, absorptions in the optics lead to thermal lensing effects [BGF+03, HV90, WDRS91], which effectively increase the ROC of the mirrors and thus decrease the Gouy phase. For other resonators thermal effects were characterized in [UGFB97, BLFB08]. Furthermore, contaminations on the mirror surface yield higher absorption. A Gouy phase measurement contains information about contaminations on the PMCs HR mirror surfaces which are not accessible and cannot be cleaned.

To evaluate the round trip Gouy phase of the PMC at the Reference System, a DBB in transmission of the PMC was used. The suppression of the HG_{40} and LG_{10} was measured while the incident power on the PMC was ramped from 100 W to 153 W. Thus, an equation for the power dependent Gouy phase was derived [KBD+12]:

$$\zeta(P) = 1.73\,\text{rad} - 848 \cdot 10^{-6} P \,\frac{\text{rad}}{\text{W}}. \tag{3.21}$$

As there is no second DBB in transmission of the PMC at the LIGO observatories, another possibility to check the power dependence of the Gouy phase is by misaligning the input beam towards the PMC, impressing phase modulation sidebands (Eq. (3.12)) and sweeping the modulation frequency. The misalign-

ment increases the power in the HG_{40} mode[7]. As the HG_{40} mode is presumably not exactly on resonance of the PMC the sidebands are swept up to the point, when one of them is resonant along with the fundamental mode. Thus, one HG_{40} sidebands will be transmitted, while the carrier HG_{40} and the other sideband will be reflected. There are two possibilities to obtain the round trip Gouy phase with a PD. Either a PD in transmission of the PMC is used to determine the beat signal of the HG_{40} sideband and the fundamental mode. Since they are orthogonal this signal can only be detected if the PD senses only a fraction of the beam for example by placing an aperture in front of it, that breaks the symmetry of the electrical field. The correct modulation frequency is set by maximizing the power of the beat signal. In principle there is also a power increase in the DC signal, which is hard to detect because the power fluctuations might be too strong. Since the power stabilization sensor is as well in transmission of the PMC it cannot be used to improve the signals SNR. Alternatively the signal in reflection of the PMC can be measured, which contains an amplitude modulation of the beat signal from the HG_{40} carrier and the reflected sideband. This method is easier to apply as there is already a high bandwidth PD in reflection of the PMC that is used for PDH locking.

3.3 Summary

To summarize, this Section gave an overview of the aLIGO laser and the PMC design. The performance of the aLIGO laser (Sec. 3.1) and PMC (Sec. 3.2) is evaluated. A long term study was conducted, which revealed that the laser system is operating robustly within the requirements set by the GWD. This was regularly checked by output beam characterization measurements with the DBB and other PD data that are recorded continuously. When the system operates in high power mode excess noise is present that is added by the HPO. Laser systems at both LIGO observatories and the Reference System in Hannover have been probed for three years without major downtime in HPM and LPM.

The results of the laser characterization show the distinct advantage of having the acoustically shielded cleanroom laser enclosure (Sec. 3.1.2, 3.1.4). Both the long term stability of the laser and the noise performance benefit from the low noise, dust free environment.

Section 3.1.5 summarizes the development and problems of lasers for future generation of GWD. It is most likely that fiber lasers will be chosen due to their compact design and the fact that they do not require beam alignment. Coherent

[7]Since the HG_{40} and HG_{04} experience the same round trip Gouy phase HG_{40} is used as a synonym for both of them in paragraph.

beam combining was introduced as method to further scale the laser power without having to deal with non-linear effects in optical fibers at high power levels.

Furthermore the design of the Pre-Modecleaner was described (Sec. 3.2.1) that is responsible for spatial beam filtering, power noise suppression at radio frequencies and pointing noise suppression. For aLIGO seven PMCs were built and the test results are according to the design specifications (Sec. 3.2.3). However, problems with contaminations inside the PMC tank were found and addressed. As a result the lid of the PMC tank was removed to mitigate the problem. A method to determine the Gouy phase is described in Section 3.2.4, which can be used to track absorptions on the resonators mirror surfaces and thus as check for contaminations.

4 Power Stabilization

An extremely low level of power noise was one of the major constraints for the aLIGO laser design. However, the power noise of the beam coming from the laser would still limit the IFO sensitivity and needs further suppression. Hence, active and passive filtering in several stages is used for the suppression of power noise.

At low Fourier frequencies technical noise is the main contributor to the overall power noise, whereas at higher frequencies quantum noise is limiting.

Many approaches were done to build a power stabilization sensor feasible for aLIGO [ROZ+04, SKH+06] and other second generation GWDs [BSK05, MOMM07, TAT08]. It took several years to demonstrate the capability to build a power stabilization that fulfills the aLIGO requirements. For the first time this was achieved by Kwee in 2009 using an array of eight PDs as sensor [KWD09]. For the active power stabilization of the aLIGO detector a similar sensor is used to detect up to 200 mA of photocurrent and build a quantum noise limited power stabilization with a power noise level of $2 \cdot 10^{-9}/\sqrt{\text{Hz}}$ at a Fourier frequency of 10 Hz.

This Chapter focuses on the implementation of the second loop power stabilization into the aLIGO detector at Livingston. First of all a short review of the principles when detecting at the quantum noise limit (sec. 4.1.1) and an overview of technical noise sources (sec. 4.1.2) are given. Additionally the coupling of power noise to the IFO readout (sec. 4.1.4), the topology of the aLIGO power stabilization is introduced (sec. 4.2), the first loop (sec. 4.3) and the power noise downstream of the IMC (sec. 4.3.2) are analyzed. In section 4.4 the improvements that were implemented for the sensor and the difficulties that occurred during the installation are pointed out. Furthermore the control loop design is discussed (sec. 4.4.4). Lastly, the results of a quantum noise limited second loop power stabilization with the sensor located inside (sec. 4.4.6) and

outside (sec. 4.5) the vacuum system are presented and the future development is discussed (sec. 4.6).

4.1 Fundamentals

For the description of noise there is a common distinction made between noise caused by the quantum nature of the light and other, so called technical noise sources. These are for example environmental disturbances or electrical couplings. This section will give an introduction to the limitations due to quantum noise and the next section deals with the influences of technical noise.

4.1.1 Sensing at the quantum noise level

In quantum mechanics laser beams, as they are generated by energy transfer to the modes of a laser resonator, can be described as coherent states. A general introduction to this topic can be found in [GK04] and [BR03].

Coherent states can be expressed as a superposition of number states $|n\rangle$ [GK04, Chap. 3.1]

$$|\alpha\rangle = \sum_{n=0}^{N} \alpha^n \frac{e^{-\frac{|\alpha|^2}{2}}}{\sqrt{n!}} |n\rangle \tag{4.1}$$

with α being the Eigenvalue and $|\alpha\rangle$ the Eigenstates of the annihilation operator $\hat{A}$. α is a complex value and contains information about amplitude and phase of the laser beam. To determine the power in a laser beam the number state representation is useful, since the number operator $\hat{N} = \hat{A}^\dagger \hat{A}$ is measuring the number of photons in state $|n\rangle$. $\hat{A}^\dagger$ is the creation operator and fulfills the commutation relation

$$[\hat{A}, \hat{A}^\dagger] = 1. \tag{4.2}$$

For a bright single mode laser beam with small fluctuations it is possible to linearize $\hat{A}$ in the frequency domain [BR03, Chap. 4.5]

$$\hat{A}(\Omega) = \delta(\Omega)\alpha + \delta\hat{A}(\Omega). \tag{4.3}$$

The Dirac delta function $\delta(\Omega)$ describes the complex amplitude α at a Fourier frequency $\Omega = 0$, which denotes the carrier frequency of the laser. The second term accounts for the noise sidebands at non-zero Fourier frequencies.

Applying Equation (4.3) to the number operator yields

$$\hat{N} = (\delta(\Omega)\alpha + \delta\hat{A}^{\dagger}(\Omega))(\delta(\Omega)\alpha + \delta\hat{A}(\Omega)) \approx \alpha^2\delta(\Omega) + \alpha\delta\hat{X}1(\Omega), \quad (4.4)$$

$$\delta\hat{X}1(\Omega) = \delta\hat{A}^{\dagger}(\Omega) + \delta\hat{A}(\Omega). \quad (4.5)$$

Here α^2 represents the average photon number and $\delta\hat{X}1$ are the amplitude fluctuations. If all technical noises are well suppressed $\delta\hat{X}1$ only represent the quantum noise contribution. $\delta\hat{X}1$ is called the amplitude quadrature operator. Since the fluctuations of $\delta\hat{X}1$ are small the expectation value is 0.

Calculating the expectation value and the variance of $\hat{N}$ yields

$$\langle\hat{N}\rangle = \langle\alpha|\hat{N}|\alpha\rangle \approx \alpha^2 \quad (4.6)$$

$$\mathrm{Var}(\hat{N}) = \langle\alpha|\hat{N}^2|\alpha\rangle - (\langle\alpha|\hat{N}|\alpha\rangle)^2 = \alpha^2\mathrm{Var}(\delta\hat{X}1). \quad (4.7)$$

Although the fluctuation do not contribute to the expectation value they show up in the variance.

If quantum noise dominates $\delta\hat{X}1$ the variance can be calculated as:

$$\mathrm{Var}(\delta\hat{X}1(\Omega)) = \langle 0|\delta\hat{X}1(\Omega)^2|0\rangle = 1. \quad (4.8)$$

Therefore, there is always noise caused by zero point fluctuation of the vacuum state on a laser beam.

The quantum noise s_q of a beam with power P, photon energy $h\nu$ and average photon number $P_{mean}/h\nu$ expressed as a single-sided linear spectral density applying Equations (4.7) and (4.8) is

$$s_q = \sqrt{2\mathrm{Var}(P(\Omega))} = \sqrt{2(h\nu)^2\mathrm{Var}(\hat{N}(\Omega))} = \sqrt{\frac{2hcP_{mean}}{\lambda}}. \quad (4.9)$$

Consequently, with an ideal photodetector the lowest noise level that can be measured for a quantum noise limited laser beam is a white noise linear spectral density at a level calculated in Equation (4.9), which is called shot noise.

A power stabilization sensor in a GWD is always sensing a fraction of the power from the main beam. Using a classical description of a beam splitter it can be assumed that the relative power noise level does not change for the beams in transmission and reflection. However, vacuum fluctuations have to be considered as Figure 4.1 illustrates. Only fluctuations caused by quantum noise are considered in the following. $\delta\hat{X}1_{in}$ is the noise of the initial beam, the beam reflected from BS_1 is directed towards the power stabilization sensor.

Evaluating the noise of the beam in reflection of BS_1 the operator $\delta\hat{X}1_{in}$ transforms with the following matrix relation [BR03, Chap. 5.1]:

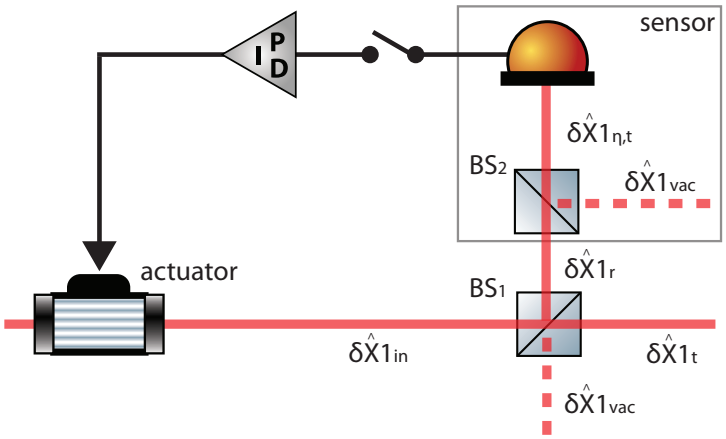

Figure 4.1: Sensing and feedback control of quantum noise limited beam. $\delta\hat{X}1_{in}$, $\delta\hat{X}1_r$ and $\delta\hat{X}1_t$ describe the fluctuations in the amplitude quadrature of the input beam, the reflected and transmitted beam of BS_1. The sensor is considered as another beam splitter, where the splitting ratio is determined by the quantum efficiency.

$$\begin{pmatrix} \delta\hat{X}1_r \\ \delta\hat{X}1_t \end{pmatrix} = \begin{pmatrix} r & t \\ t & -r \end{pmatrix} \begin{pmatrix} \delta\hat{X}1_{in} \\ \delta\hat{X}1_{vac} \end{pmatrix}. \tag{4.10}$$

Here, t and r are the amplitude transmission and reflection coefficients, which obey the relation $r^2 + t^2 = 1$, if internal losses are not considered. Assuming that no light is entering from the open port of the beam splitter, vacuum fluctuations $\delta\hat{X}1_{vac}$ still have to be considered.

For the power stabilization the beam of interest is the one in reflection. In this case optical losses can be described as a reduction of the beam splitter amplitude reflection coefficient to determine the quantum noise limit of the power stabilization.

The reflected light has a noise according to Equation (4.10)

$$\begin{aligned} \mathrm{Var}(\delta\hat{X}1_r(\Omega)) &= r^2\mathrm{Var}(\delta\hat{X}1_{in}(\Omega)) + t^2\mathrm{Var}(\delta\hat{X}1_{vac}(\Omega)) \\ &= r^2\mathrm{Var}(\delta\hat{X}1_{in}(\Omega)) + (1 - r^2) \end{aligned} \tag{4.11}$$

in which the last term is representing the contribution from the vacuum noise entering the open port. Unless $r^2 = 1$ the noise of reflected beam is higher than the noise of the input beam.

In the actual experiment, PDs are used to convert an optical signal into an electrical signal. The quantum efficiency η describes the rate of photons that are

converted into electrons and if $\eta = 1$ every photon is converted to an electron. During this process no extra noise is added. However, in reality η is always less than one and thus there is extra noise. This noise can be modeled as a second beamsplitter that is added before the laser beam hits the PD as shown in Figure 4.1. The beam splitter BS_2 has a amplitude transmission of $\sqrt{\eta}$ and can be described with the same formalism that is used to evaluate the light picked off from the main beam at BS_1.

For most applications the photo current is measured and hence shot noise is referred to as current shot noise

$$s_q = \sqrt{2eI_{mean}}. \tag{4.12}$$

Compared to Equation (4.9), the photon energy is replaced by the charge of an electron and the average power is replaced by the current I.

By injecting amplitude squeezed vacuum into the open port, which has a sub-poissonian distribution the noise level in the amplitude quadrature decreases. This comes at the cost of a higher noise in the perpendicular phase quadrature $\delta\hat{X}2$ according to Heisenberg's uncertainty principle. Squeezed states were used to improve the sensitivity of a GWD [VKL+10, ftLSC13], but there hasn't been a power stabilization experiment involving squeezed states, to my knowledge, so far. Optical losses and a low quantum efficiency of the PD decrease the squeezing quality.

4.1.2 Technical noise sources

Quantum noise can be observed if all other noise sources are small compared to the quantum noise limit, but that is often not the case. Especially at low Fourier frequencies technical noise sources dominate the power noise spectrum. The term technical noise describes all contributions to the power noise that are not related to the quantum nature of the light.

The technical noise sources can further be split in two groups. Using the notation from Figure 4.1 there is power noise $\delta X1_{in}$ that is present on the main beam that is being stabilized and noise that couples in downstream of BS_1 in the pick off path to the in-loop detector.

Noise $\delta X1_{in}$ present on the main beam can originate from thermal drifts, laser pump light power fluctuation, dust particles passing through the beam, vibrations causing length fluctuations in the laser resonator by exciting resonances of mechanical components, pointing to power noise coupling of a cavity, polarization fluctuations and frequency noise cross coupling.

Downstream of the pick off temperature drifts and unwanted polarization rotation affect the splitting ratio of subsequent beamsplitters that are for example used to direct the beam towards an in-loop and an out-of-loop detector.

Scattered light on the PD and a non-uniform response across the PD surface in combination with pointing of the laser beam can add noise. Moreover, internal properties of the semi-conductor couple via the dark current and electronics noise of the PD readout and have to be considered.

While noise present in front of the BS can be suppressed with a feedback control loop, the latter noise source have to be as low as possible, since they are imprinted on the main beam. The noise sources that are limiting the aLIGO power stability are described more detailed in the next Sections. A detailed characterization of noise sources was done in [Sei09, Kwe10] and [Bog13].

As most noise sources have independent origins they are uncorrelated and add quadratically. In terms of noise current at the PD readout the total noise is

$$\tilde{I}_{tot} = \sqrt{\tilde{I}^2_{\text{technical A}} + \tilde{I}^2_{\text{technical B}} + ... + \tilde{I}^2_{\text{quantum}}}. \tag{4.13}$$

4.1.3 Power noise limit for active feedback and passive filtering

Power stabilization can be done with active feedback by building a control loop or using a passive filter, such as an optical resonator. Both approaches have advantages and disadvantages which are discussed in this Section.

Optical resonators filter technical power noise above their pole frequency with a low pass behavior. Building optical resonators with a low pole frequency is challenging since they require a long round trip path length and low internal losses. Therefore they are usually used for power noise filtering at high frequencies (Sec. 3.2). In order to get power noise suppression as low as the quantum noise limit of the input beam impedance matched cavities have to be used because the carrier is not completely transmitted in the under- or over coupled case.

For an active feedback loop a sensor that converts an optical signal to an electrical signal is necessary. Considering the setup shown in Figure 4.1 a PD is used as sensor. The obtained signal contains quantum noise that does not originate from the main beam, but is added at BS_1 and BS_2. By closing the control loop and adding the feedback signal to the main beam, noise is imprinted on the beam. The magnitude of the additional noise depends on the splitting ratio of BS_1 and the PD quantum efficiency η.

To evaluate the power stability of the main beam with feedback engaged another PD has to be added that detects the power noise $\delta X1_t$. If the same power level is sensed with the in-loop and out-of loop PD the best achievable noise level is 6 dB above the quantum noise of the original beam [TWMB95, KWD10].

This is a clear disadvantage of active power stabilization and furthermore

there are additional limitations set by damage thresholds of the PDs. Apart from that it is possible to suppress technical power noise with very high gain at low Fourier frequencies with an active control loop. Hence, it makes sense to combine active and passive stabilization methods in many experiments.

A novel method to do active power stabilization by stabilizing the power in reflection of a high finesse cavity is called optical AC coupling [KWD08]. As most of the carrier light is transmitted through the cavity, a very high shot noise limited sensitivity above the cavity pole frequency can be reached. However, this technique requires a resonator with a low pole frequency to be useful for GWDs.

4.1.4 Power noise coupling to the Interferometer readout

After the description of the noise sources this Section will give a qualitative overview of the coupling mechanisms from power noise to the dark port of the GWD. The coupling strength determines the requirements for the power stability of the input beam.

Advanced LIGO operates in a dual-recycled Michelson IFO configuration with arm cavities [HtLSC10]. If the dark port would be totally dark there would be no coupling of power noise.

However, it is not possible to detect the gravitational wave signal with no light at the dark port. Besides there is always some tolerance in the fabrication of optics, such that leakage light is always present at the dark port. There are two approaches to read out the IFO [Sau94]. The first one is an intentional offset of the IFO from the dark fringe to generate a local oscillator for a homodyne detection scheme. This, so called DC readout scheme, is usually done in combination with an OMC that removes higher order spatial modes and modulation sidebands from the beam at the dark port. The second approach is to imprint phase modulation sidebands on the beam and use a modulation-demodulation scheme to generate an error signal and lock the IFO. The drawback is that the modulation sidebands are only resonant in the power recycling cavity and thus rf power noise is limiting the sensitivity of the GWD at high frequencies. Additionally if detuned resonant sideband extraction (RSE) [MSN+93] is used there is an imbalance in the sideband power as they resonate in the SRC.

Since aLIGO will use DC readout only the power noise coupling for this readout scheme is considered in the following analysis. The signal at the output port is sensitive to asymmetries in the IFO arms. Thus only effects, that intentionally or unintentionally introduce such an asymmetry can contribute to the power noise at the output. The full analysis is done in [SCKM06, SCKM07], but in principle there are two processes that couple power noise to the IFO output.

The first one is a direct coupling from power noise at the input to the output. Although the power recycling cavity has a pole frequency of several kHz, power noise is filtered with f^{-1} above 1 Hz. This is due to the over coupled arm cavities since noise sidebands outside the arm cavity line width experience an extra π phase shift and are not resonant in the power recycling cavity. This compound pole created by the power recycling cavity and the arm cavities is called the coupled cavity pole. An IFO contrast defect, a finesse mismatch of the arm cavities and an offset in the microscopic arm length mismatch are the dominating coupling channels for power noise at high Fourier frequencies.

At low frequencies is power noise coupling due to radiation pressure differences in the arms is more important. Radiation pressure noise arises from the impact of the photons on the arm cavity mirrors causing a momentum transfer. This noise scales inversely with the mirror mass and the power of the field stored in the cavity. An imbalance of the mirror masses, finesse differences and an unequal beam splitter splitting ratio are leading to radiation pressure effects that contribute to the differential IFO readout signal. Since the signal at the dark port is sensitive to differential length changes of the two arms and the origin for radiation pressure is a force on the mirror it scales with f^{-2} in the spectrum of the readout signal. Therefore it dominates the power noise coupling at low frequencies, but falls off rapidly towards higher frequencies.

Additionally, the coupling strength depends on the readout quadrature. The signal is read out in the phase quadrature for a power recycled Fabry-Perot Michelson IFO. Adding the signal recycling tuning of the cavity changes the read out quadrature and the shape of the quantum noise in the read out signal. Advanced LIGO will start operating with broadband signal recycling and the optimum readout phase of $\pi/2$. However, in this configuration the power noise coupling is maximum and the technical power noise exceeds the quantum noise in the IFO readout signal, as it is currently not foreseen to sense more than 100 mA photocurrent for the power stabilization. Fortunately, a reduction of the DC offset by small change in the readout phase affects the power noise coupling significantly, while the shape of the quantum noise changes marginally [KSA06].

This leads to requirements that are set for the input of the IFO and have to be met by the power stabilization [WKSF11]. A requirement for power noise at radio frequencies is necessary to avoid excess power noise in RF sidebands that are imprinted on the beam downstream of the PMC (Sec. 3.1.4).

4.2 Topology of the Advanced LIGO power stabilization

The aLIGO power stabilization consists of active and passive components. For the active feedback control loop there are two sensors. Figure 4.2 shows the schematic of the loops. For the pre-stabilization a fast loop, called first loop, employs a single PD as a sensor and an AOM as an actuator. A second, in vacuum sensor is using four PDs as in-loop sensor. The control signal is fed back to the error point of the first loop in order to add a sensor correction.

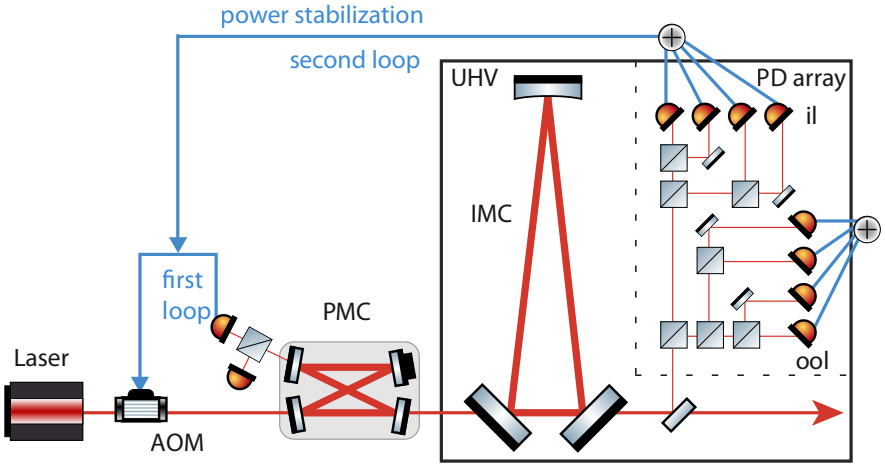

Figure 4.2: Schematics of aLIGO power stabilization. The first loop sensor is located downstream of the PMC. The in vacuum sensor for the second loop power stabilization consists of four PDs. An identical set of sensors is utilized for the out-of-loop power noise detection. An AOM in the high power beam serves as an actuator.

Passive power noise filtering is provided by the PMC and the IMC. The PMC pole frequency is 578 kHz and the IMC pole frequency at 8.7 kHz. The PMC filter effect is important for noise suppression at high Fourier frequencies, at which phase modulation sidebands are imprinted since the electro-optic modulator (EOM) that creates these sidebands is located downstream of the PMC and before the IMC.

As experiments in the past showed a difference between the measured in-loop performance and the power noise of an independent sensor, a second, identical set of sensors is installed to provide an independent out-of-loop measurement.

Due to its small size a verification measurement of power noise at radio fre-

quencies is not possible with classical methods and a single PD. More than 100 mW need to be detected (Fig. 3.4) to keep the shot noise below the technical noise. To check the power noise downstream of the PMC a measurement using the optical AC coupling technique was performed [KBD+12].

The following Sections describe the first and the second loop in more detail. Furthermore a computer model was developed for control loop simulations (Sec. 4.2). For the first loop the bandwidth limits are studied in Section 4.3.1 and the power noise downstream of the IMC is analyzed in Section 4.3.2. A description of the in vacuum sensor, the control loop design for the second loop and the results of the stabilization in different configurations is given in Section 4.4. The second loop measurements were performed at LLO.

All measurements at LLO were done in low power mode without the HPO engaged, because technical difficulties, unrelated to the laser system, allowed only for a maximum power of 1 W entering the vacuum system. To achieve a better shot noise limited sensitivity another sensor was installed outside the vacuum system and in transmission of the IMC and described in Section 4.5. Amongst other possibilities to improve the second loop in the future, the impact of high power operation is addressed in Section 4.6.

Control loop modeling and simulations

The loop simulations are done with a Simulink model, that evaluates linear time invariant (LTI) elements representing individual parts of the power stabilization loop. Figure 4.3 gives an overview of the Simulink model. Transfer functions can be obtained from various inputs and outputs. The LTI objects are created by converting them from given zeros, poles and gains.

Although the model is evaluated with a state space approach, so far the analysis was only conducted in the frequency domain. The simulation includes both, the first and the second loop. It can be configured to either simulate only the first loop or both loops. It also has the possibility to simulate a loop with the first loop sensor downstream of the IMC, as it was realized at LLO and is described in Section 4.5.

The simulations of electronic circuits are done with LISO [Hei00]. The advantage of LISO is that it includes measured parameters of operational amplifiers (OPs) and simulates effects due to gain bandwidth product (GBP) limitations of a feedback loop. Additionally, LISO is used for noise simulations of readout and servo electronics. The vector fitting algorithm of LISO is very powerful and led to the identification of zeros and poles that were transferred to the Simulink simulation.

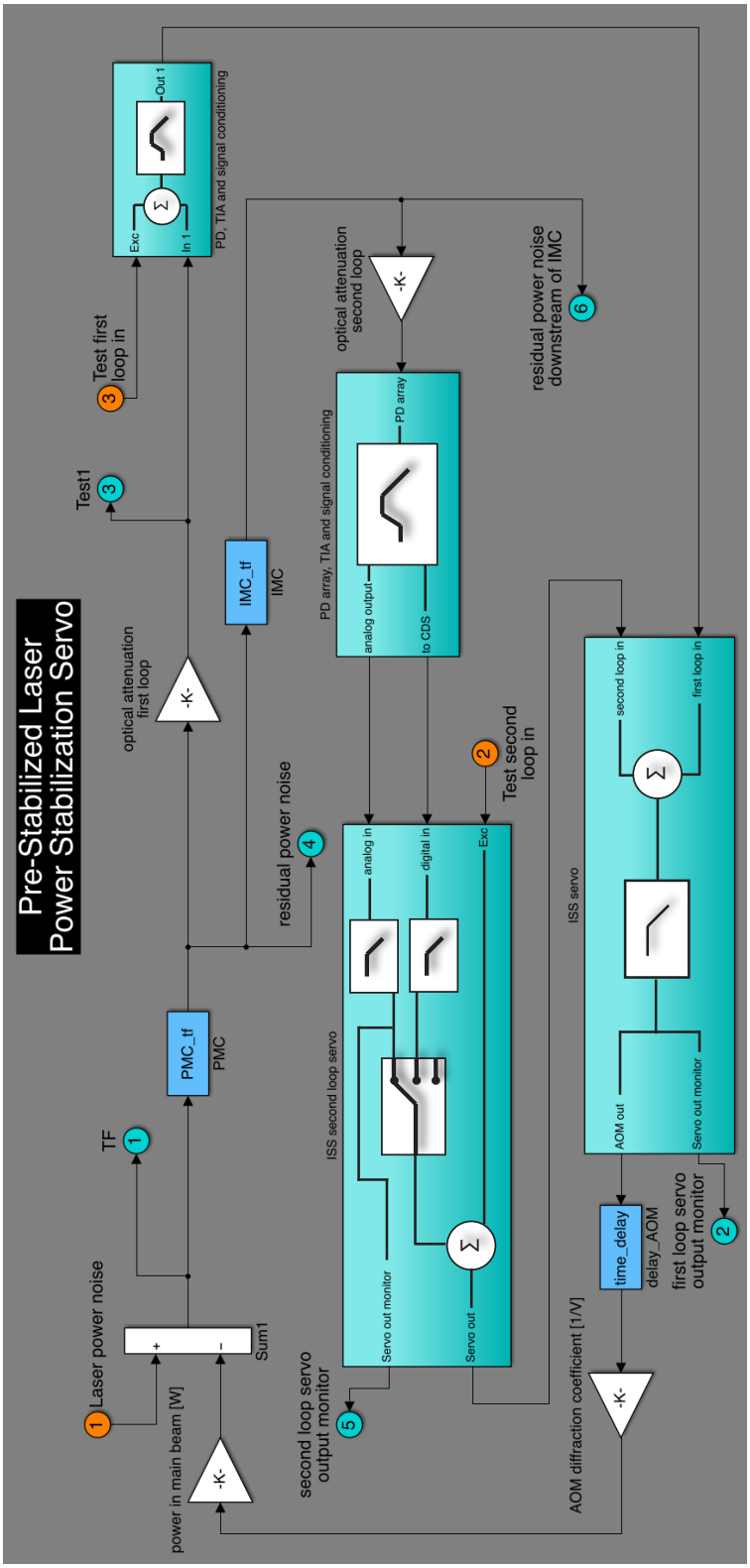

Figure 4.3: Simulink model of the aLIGO power stabilization

4.3 First loop

The first loop power stabilization uses a single PD as a sensor that is located outside the vacuum system and detects up to 3 mA of photocurrent. This is equivalent to a shot noise limited sensitivity of $1 \cdot 10^{-8}/\sqrt{\text{Hz}}$. The amount of light on the PDs can be adjusted with an attenuator and is set such that in low- and high power mode the light level does not change. To avoid problems with stray light on the PDs, they are housed in an aluminum box.

The loop is DC coupled, but has an attenuation of 0.2 at Fourier frequencies less than 70 mHz. Furthermore, the signal conditioning amplifies the signal at 10 Hz by 52 dB.

An AOM (Crystal Technologies 3080-199) serves as actuator upstream of the PMC (Fig. 4.2). The actuation is done by modulating the power with a static offset in first diffraction order of the AOM. To amplify the signal applied to the AOM a RF amplifier (Neos 21086-2AM-RFX) is used. The beam passing the AOM in zeroth order is directed towards the main experiment. It was verified that the AOM does not deteriorate the spatial beam quality [Põl09].

Although the loop state is controlled by the computer system its signal processing is done in analog electronics to achieve a high bandwidth. The design and performance of the loop is described in more detail in [Bog13] and [KBD+12]. In the following Section the limits for this control loop bandwidth are pointed out.

4.3.1 Bandwidth limits of the first loop

In LPM the first loop is limited by loop gain at Fourier frequencies smaller than 2 Hz and higher than 1 kHz whereas in the intermediate frequency range the loop is limited by quantum noise. In high power mode there is additional unidentified noise at Fourier frequencies below 50 Hz (Fig. 4.6).

Figure 4.4 shows a measurement and a simulation of the first loop transfer function at the Reference System and LLO. The simulation was done with a state space Simulink model that is described in Section 4.2. In order to fit the results for the initial simulation and the measurement a time delay of 2 µs[1] was added to the simulation to fit the phase to the measured curve. In the current configuration at LLO the unity gain frequency is 80 kHz with a phase margin 15 degrees. Moreover, the loop is bandwidth limited[2] around 100 kHz and a high bandwidth is important for this loop, because it also determines the maximum bandwidth for the second loop.

[1] 2.2 µs for LLO measurement

[2] The bandwidth limit is defined as the point where the phase reaches -180 degree.

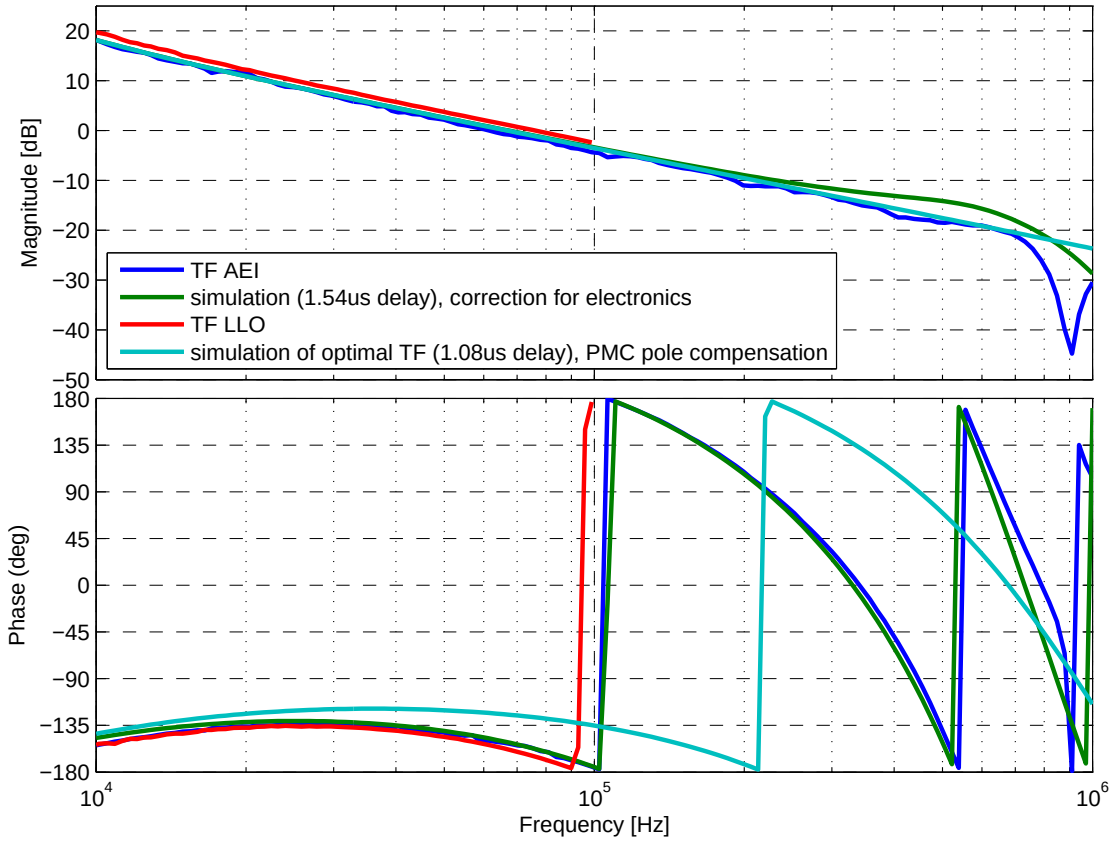

Figure 4.4: Simulation and measurement of the transfer function of the first loop power stabilization: measurements at the AEI Reference System (blue) and LLO (red); Simulations of the current Reference System setup (green) and the optimal loop (turquoise) without phase delays caused by the servo electronics including a PMC pole compensation

The most obvious reason for a time delay is due to the propagation velocity of the acoustic wave in the AOM. The literature specifies 0.5-5 µs [GS11] as expected time delays in commonly available AOMs. The delay depends on the AOM crystal material, the laser beam size and the distance between the transducer, which generates the acoustic wave and the laser beam. The crystal material is TeO_2 and the speed of the acoustic wave is 4.2 µm/µs [Liu05, Chap. 8.2].

A measurement of the time delay of the AOM was conducted at the Reference System by obtaining a transfer function from the AOM driver modulation input to a high speed PD, that monitors the power in the main beam downstream of the AOM. An additional time delay caused by the cables is included in the measurement, because this cable is part of the setup as well. On the passage

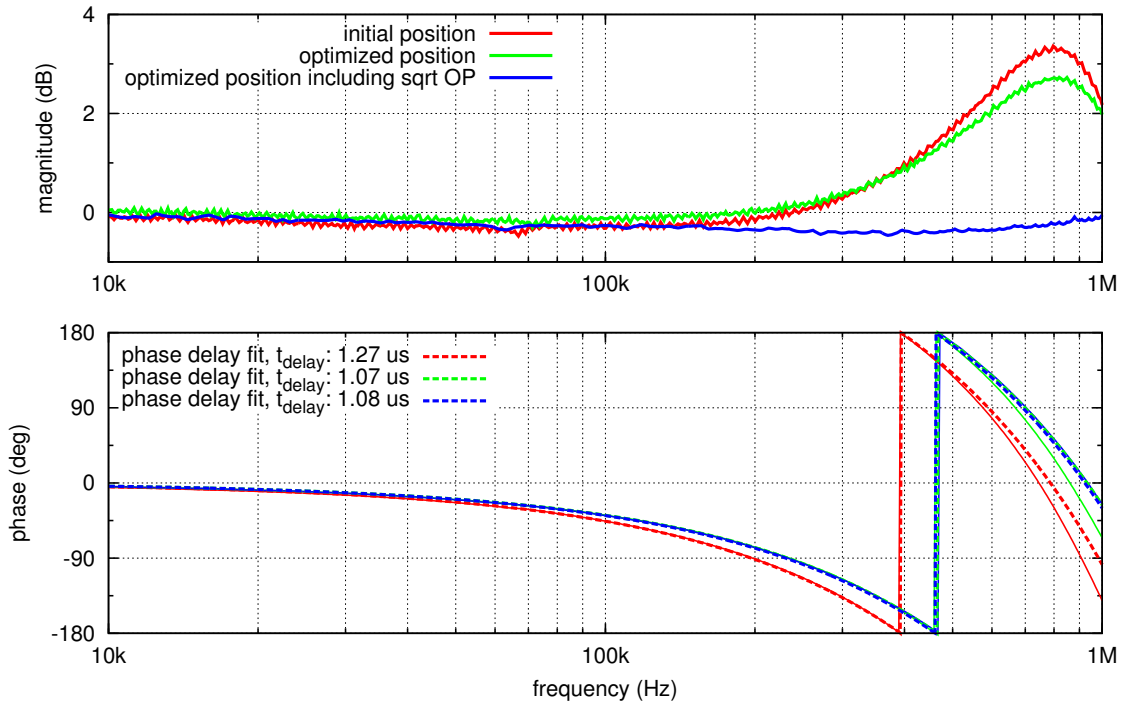

Figure 4.5: Transfer function and fit of AOM driver and AOM including a 13 m cable at the Reference System. The distance from the AOM transducer to the laser beam is varied to evaluate the time delay that is mainly introduced by the propagation speed of the acoustic wave. A gain peaking at 800 kHz can be removed using a square root OP which linearizes the transfer function of the AOM.

towards the AOM the beam diameter is approximately 740 µm and the beam divergence is small.

Figure 4.5 shows the AOM transfer function including a fit for the time delay that was measured. In the initial position a time delay of 1.27 µs is observed. To optimize the response the position of the AOM was varied with a translation stage and micrometer accuracy. Thus the beam was moved closer to the PZT that generates the acoustic wave. At the same time the DC voltage on the high speed PD and the power transmitted through the PMC was monitored to make sure that the beam is not clipped at the AOM. Moving the beam 0.85 mm closer to the transducer reduced the time delay by 0.2 µs. This agrees well with the travel time of the acoustic wave in TeO_2. The center of the beam is still 2 mm - 3 mm from the edge of the crystal. As the laser beam also contains higher order modes with a wider spatial distribution the AOM is kept in this position.

The power in the diffracted beam of the AOM depends quadratically on the

offset voltage that is supplied to the AOM driver. When the voltage modulations are small and the AOM is operated with an offset it can be assumed that the response is linear. To verify that the measurement can be analyzed in a linear regime, the modulation amplitude was changed and no change in the transfer function was observed. For the control loop an OP taking the square root of the control signal is implemented to avoid nonlinear effects. For the final position of the AOM another transfer function was taken that included the square root OP. As seen in Figure 4.5 the delay does not change significantly, but the amplitude response is smoother at high Fourier frequencies.

Accounting for the AOM time delay and for additional 13 m coaxial cable[3] 1.15 µs time delay of the 2 µs inserted in the simulation are understood. Measuring the transfer function of the servo electronics revealed extra phase lag due to limitations of the OP GBP. Additional poles and zeros determined by a fit of the measured servo transfer function allows a correction for the phase lag caused by the electronics in the simulation. This leaves an unexplained phase lag, which the simulation accounts for with 0.4 µs time delay, that is presumably caused by the actual OP response in the PD signal conditioning filter.

For further bandwidth optimization the PMC pole needs to be compensated. Assuming a PMC pole compensation and no phase lag caused by the electronics, that can be realized by using faster OPs an optimum bandwidth of 200 kHz can be achieved (Fig. 4.5). With similar AOMs a phase lag of 45 degree at 450 kHz was achieved [Sei09], but therefore the beam has to be smaller and located closer to the transducer. This was not possible for the aLIGO PSL due to the high intensity of the laser beam in conjunction with the AOM crystal damage threshold.

To overcome the limitation of the AOM, an alternative is an EOM, that has a bandwidth up to 100 MHz. However, the damage threshold for off-the-shelf devices is very low. Custom made EOMs, utilizing Rubidium Titanyle Phosphate (RTP) crystals, are already in use in aLIGO [Que08] and are compatible with high laser power [Bog13]. These EOMs in combination with a polarizing element might also be feasible as power actuator.

4.3.2 Power noise downstream of the Input-Modecleaner

One essential question for the design of the second loop is how much power noise is added to the beam in transmission of the IMC, since this is what the second loop needs to suppress as well. From the output of the PMC the beam passes an EOM, steering optics and a periscope that elevates the beam to the height of the vacuum systems viewport. Inside the vacuum chamber it passes

[3] The cable length from readout PD to servo electronics.

several suspended optics, the IMC and a Faraday isolator before it enters the power recycling cavity (PRC).

Figure 4.6 shows two measurements of the power noise downstream of the IMC. The trace from September 2012 was taken with a PD that detects a pick off beam right in front of the PRM. Since this PD is electronics noise limited at $5 \cdot 10^{-7}/\sqrt{\text{Hz}}$ the measurement in August 2013 was done with a PD outside the vacuum chamber in transmission of the IMC and in front of the Faraday isolator (Fig. 4.8). Both measurements were taken while the first loop was engaged.

The September 2012 measurement does not contain significant features, except one at the mains frequency, but the overall power noise level is very high and even exceeding the unstabilized laser power noise in LPM (Fig. 3.3). The measurement upstream of the periscope shows that most of the noise is impressed by the IMC in conjunction with the periscope, although the noise upstream of the periscope is already higher compared to the out-of-loop measurement of the first loop (Fig. 4.6).

Over the course of the commissioning noise sources were identified and lowered. In order to make a low noise measurement the FFUs and AC in the PSL enclosure need to be switched off, since air currents and vibrations of the fans cause additional noise especially at low frequencies.

A major noise contribution is caused by pointing to power noise conversion at the IMC. In the eigenbasis of a resonator a misalignment of the input beam in position or angle can be expressed in the Hermite-Gauss basis as [ACT+06, And84]

$$E_{in} = HG_{00} + \epsilon_x(t)HG_{10} + \epsilon_y(t)HG_{01} \tag{4.14}$$

with $\epsilon_{x,y}(t)$ being the pointing noise as a function of time. Since the first order HG modes are non resonant if the cavity is locked on the HG_{00} mode, they are reflected. Thus the power noise in transmission of the cavity scales with ϵ^2 if there is no static misalignment.

On top of the periscope a Piezo controlled mirror is mounted that steers the beam towards the IMC input mirror. Although this control loop runs with a UGF less than 1 Hz the electronics noise of the controller contributes to the pointing noise of the input beam in the detection band. Furthermore the Piezo controller has a position readback that is part of a control loop which was also found to introduce noise that influenced the power noise downstream of the IMC. Additionally turbulent water flow in the laser cooling circuit caused vibrations on the table (Sec. 5.4.1).

After switching off the position feedback to the Piezo and applying additional passive low pass filtering in the output of the Piezo driver electronics the pointing noise and thus the power noise downstream of the IMC could be lowered (Fig. 4.6). The power noise measurement from August 2013 nearly follows

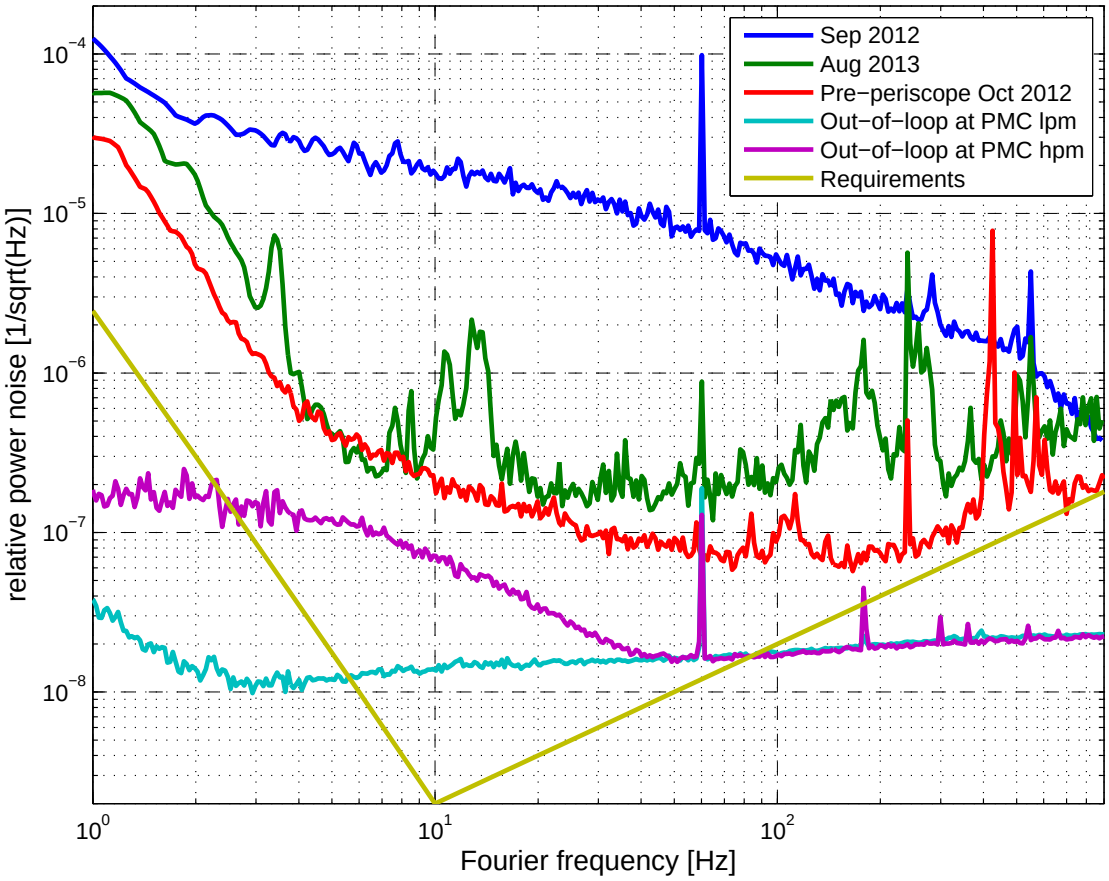

Figure 4.6: Power noise measurements. The blue trace shows the power noise after installation of the IMC in September 2012 and the power noise upstream of the periscope in the PSL enclosure is shown in red. After some improvements the noise was lowered and remeasured in August 2013 (green trace). Out-of-loop measurements in HPM (purple) and LPM (turquoise), which were acquired at the out-of-loop detector of the first loop, show excess noise at low frequencies when the HPO is switched on.

the shape of the noise measured upstream of the periscope and has additional peaks above 100 Hz. These are presumably caused by PSL table and periscope resonances.

Moreover, relative motion between the passively isolated PSL table and the actively controlled HAM internal seismic isolation system or the suspended mirrors of the IMC contributes to the power noise downstream of the IMC. According to [Mül09] this noise coupling should be negligible.

4.4 Second loop

The power noise downstream of the IMC leads to the gain requirements for the second loop power stabilization.

It is necessary to use a sensor that is capable of detecting more than 100 mW of light, as shown in the previous Section. The description of this sensor and the difficulties for its alignment (Sec. 4.4.1) is followed by a discussion of the electronics (Sec. 4.4.2) and the actuator (Sec. 4.4.3). The question whether it is sufficient to build a digital control loop with the existing real-time control system is addressed in Section 4.4.5. Section 4.4.6 summarizes the results achieved with an analog control loop.

4.4.1 Sensor

The only sensor that ever showed the performance required for aLIGO is reported in [KWD09]. Therefore a similar sensor design was chosen for the aLIGO second loop power stabilization and built by LIGO scientists. It consists of eight 2 mm InGaAs Excelitas[4] C30642 PDs which are positioned in two rows of four. The glass windows in front of the PDs were removed to avoid scattering and reflection from the surface. The beam reaches the PDs at a 45 degree angle, which makes its projection elliptical on the PD chip. Residual light reflected from the PD is absorbed by a BG39 glass filter. Figure 4.7 shows a picture of the PD array installed in the LIGO vacuum chamber (Fig. 4.8) and a sketch with pointers to the individual components is illustrated in figure 4.9.

The beam that is sent to the PD array is picked off right before the PRM. There are several optics in the beam path between the pick off and the array, such that there is a power level between $214 \cdot 10^{-6} \cdot P_{main}$ and $272 \cdot 10^{-6} \cdot P_{main}$ on the PDs due to the unequal splitting ratio of the beam splitter inside the PD array for the reflected and transmitted beam. Contrary to the first loop there is no power attenuator for the second loop. As the IFO is not always operating at the full power level of $P_{main} = 125\,W$ the light level on the PDs varies depending on the input power. On average 30 mW is detected on each PD at full power. The beam injected into the PD array is horizontally polarized.

From the IMC the nearly collimated beam with a radius of 2.2 mm travels through a mode matching telescope in order to match the beam size with the PRC eigenmode. The slightly divergent beam does not exceed a radius of 3 mm before it reaches the mirror in front of the array where it is focused such that it does not exceed the active area of the PD. The average beam radius is 237 μm on the PDs. All optics in the main path have at least a diameter of 3 inch (76.2 mm)

[4] former Perkin Elmer

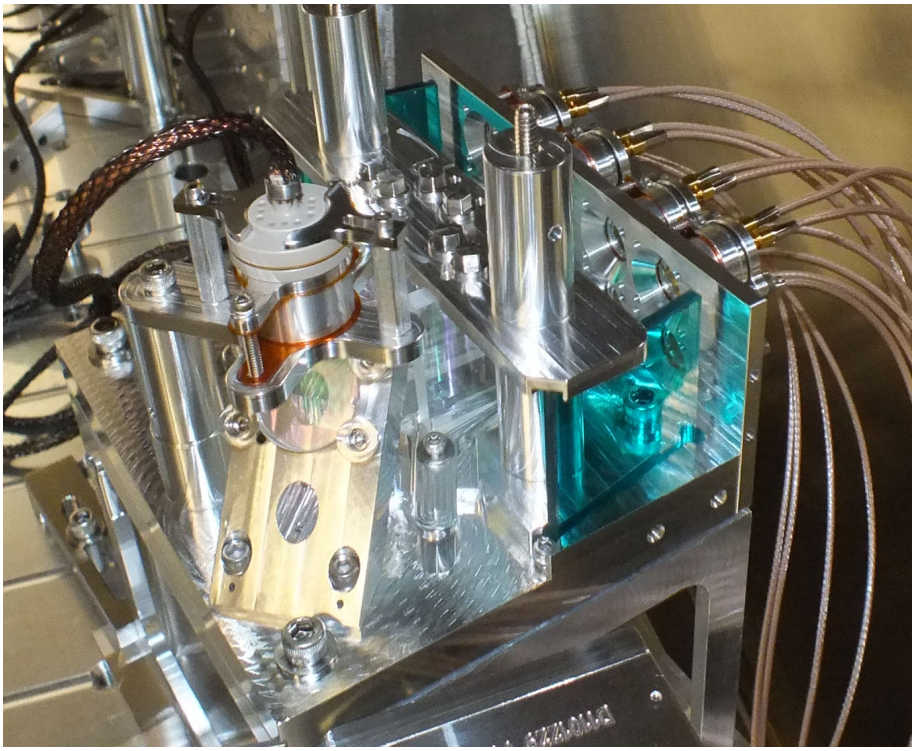

Figure 4.7: Picture of PD array inside the LLO HAM2 chamber.

and in the path towards the array 2 inch (50.8 mm) diameter. However, the smallest apertures the beam has to pass are apertures of stray light baffles.

For alignment purposes and in order to measure the pointing noise a quadrant photodiode (QPD) (FCI InGaAs-Q3000) is part of the array assembly. When the eight individual PDs are initially aligned outside the vacuum system a reference position for in chamber alignment is set by centering the beam on the QPD.

In contrast to prior assumptions there are differences in the optical path length to the eight PDs of the PD array. Hence, they are not in the same focal plane and it is generally not possible to define an optimum alignment reference on the QPD. However, a long Rayleigh range of the beam impinging on the PD array is beneficial for the alignment.

For future versions of the PD array the power of the beam shining on the QPD will be increased in order to obtain a signal during alignment with low power as well. Therefore mirror transmission of the mirror in front of the QPD will be increased to 1 % . At full power this yields a power level of 1.25 mW on the QPD.

The PDs are connected via a vacuum feedthrough to the readout electronics

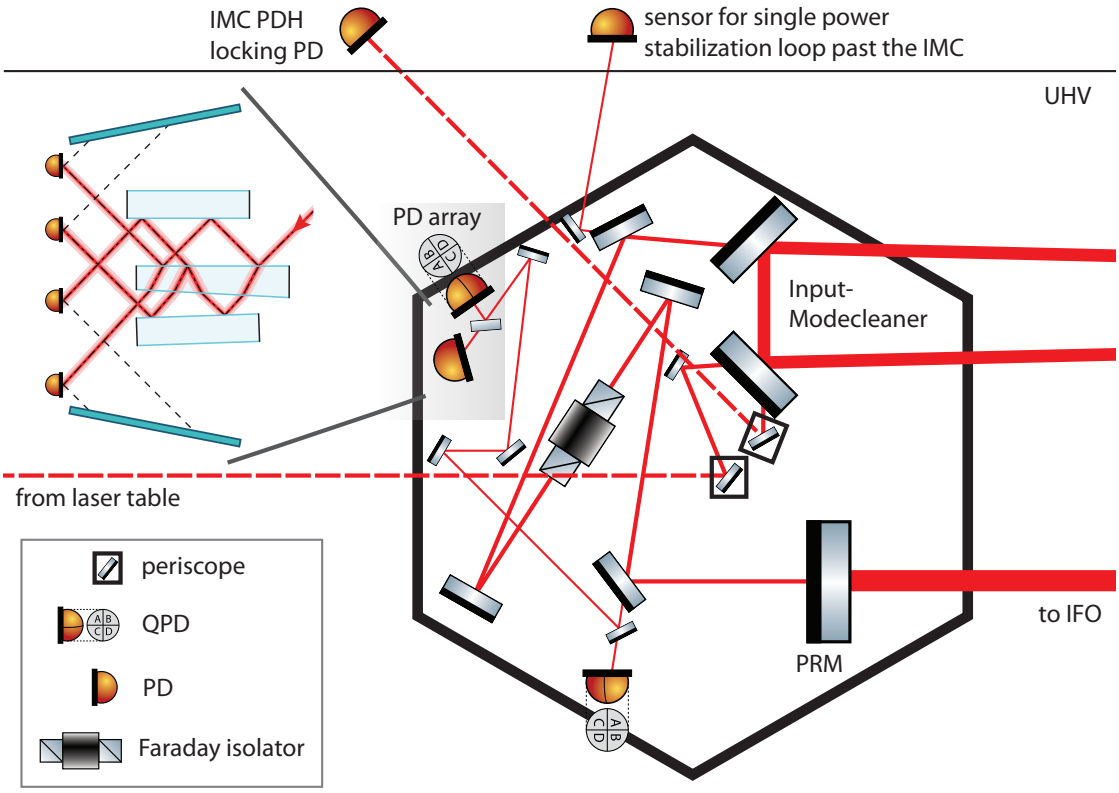

Figure 4.8: HAM2 layout and beam path towards PD array. Zoom in on the PD array beam path.

that are located outside the vacuum system (Fig. 4.10). The distance from the PDs to the readout electronics is approximately 7 m. After finding problems with the electrical interface and short circuits at the back of the PDs, Teflon sleeves were put around the PD legs to insulate them from the aluminum can they are sitting in. Furthermore the circuit board mounting was improved.

Sensor alignment

In this Section difficulties with the in chamber alignment are addressed. As the suspended optics are moving much more in the vented chamber due to air currents, it is not easy to find the sweet spot of the PDs. Here, sweet spot describes the location on the PD where the coupling from pointing to power noise is at its minimum. Moreover, it should not differ more than 1 % from the maximum response according to [Sei09]. To find this point for all PDs simultaneously the alignment procedure requires the incoming beam hits the PD array identical to

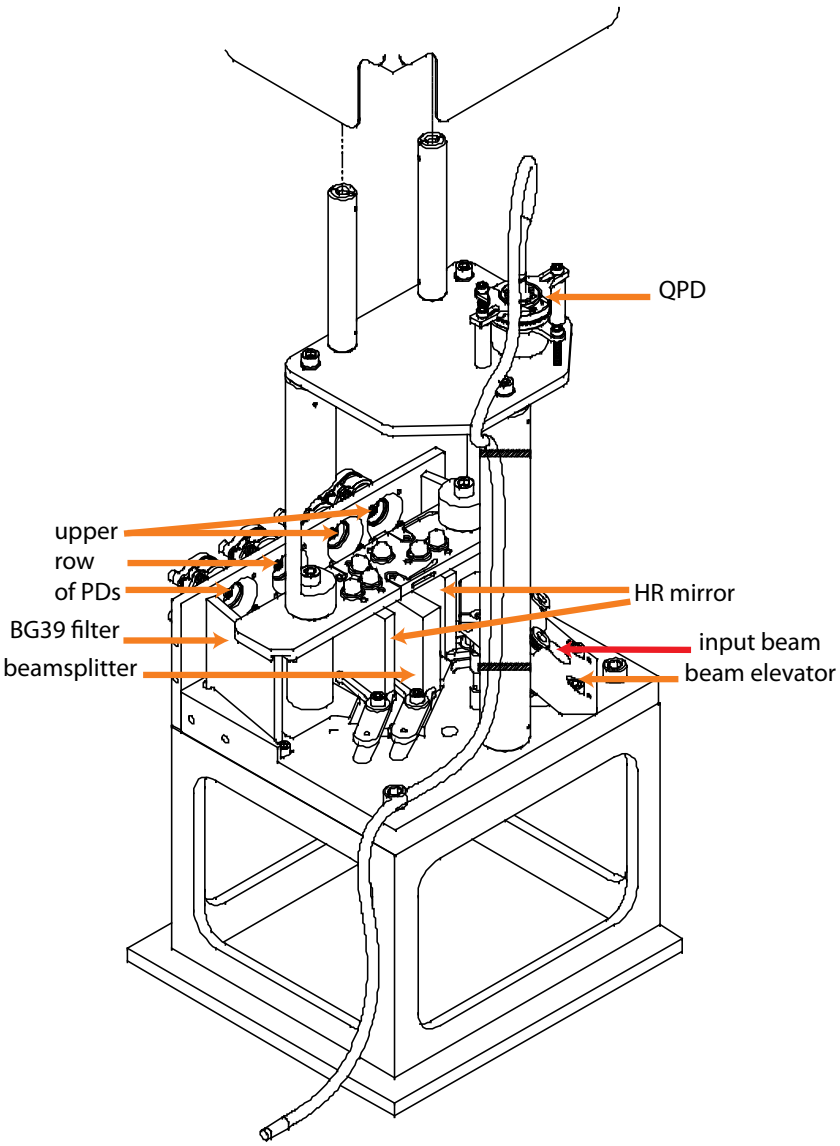

Figure 4.9: Drawing of PD array including modifications. A lid covers the whole assembly when installed in the vacuum system.

the beam used for the PD alignment.

The pointing to power noise coupling due to the non uniform response of the PD across its surface is [Kwe10]

$$c_{pnt\rightarrow RIN} = \frac{1}{P(0)} \cdot \frac{dP(x)}{dx}\bigg|_{x=x_0} \tag{4.15}$$

and defined in the unit 1/m. The impact of the coupling is the strongest at

10 Hz as the power noise requirements are most stringent at this frequency. The pointing noise requirement for the transmitted beam of the IMC at 10 Hz is $\epsilon = 1{\cdot}10^{-6}/\sqrt{\text{Hz}}$ [Mül09]. As the beam is elliptical on the array PDs a beam radius ω of 400 µm is assumed. Furthermore, it is assumed that the lateral motion of the beam δx is approximately $\delta x = \epsilon\omega$. Consequently $c_{\text{pnt}\rightarrow\text{RIN}}$ should be less than 5/m to be on the same level as the quantum noise. For this calculation pointing noise was assumed to contribute as correlated noise on the PDs. Although in prior experiments coupling factors less than 5/m have been reported [KWD09, KBD+12], experiments with another aLIGO PD array showed that the coupling is between 5/m and 40/m for the individual PDs.

As the beam directed towards the PD array has a waist of 70 µm and consequently a Raleigh range of 1.5 cm the positioning has to be very accurate [MWG+14]. Due to the 45 degree angle of incidence and the ellipticity of the input beam it is likely that the beam exceeds the active area of the PD if it is not positioned correctly. Inserting another curved mirror in the beam path towards the PD array can extend the Raleigh range and allows for a better in vacuum alignment if it is equipped with a pico motor for remote alignment.

Unfortunately, due to technical difficulties the QPD signal was not available for the array installation at LLO. Furthermore one PD could not be used, since it had ohmic resistance of 220 kΩ such that it was not possible to operate the PD with reverse bias. Due to the missing reference position on the QPD the signals on the remaining seven PDs were maximized in order to find a good alignment reference and minimize the pointing to power noise coupling.

Another difficulty for the alignment is that the IFO cannot be locked when the vacuum system is vented due to the noisy environmental conditions. Even though the beam is aligned to the array during the vent[5] it could be that this is not the reference position that perfectly overlaps with the IFO eigenmode. Therefore it is possible to compensate small differences with a pico motor actuating on one mirror in the path towards the PD array. Since the IFO was aligned for the first time after the installation of the PD array it turned out that it is only possible to either find a good alignment for the PD array or the IFO. Further investigation have to reveal if this is still the case with a pre-aligned IFO or if the alignment procedure for the PD array has to be revisited. In the worst case a second pico motor actuated mirror would be required for the PD array alignment. For all investigations of this thesis the beam towards the PD array suffered from clipping losses leading to more than 30 % reduction in the DC level, when the IFO is aligned. For the measurements presented in the following Section the main beam was adjusted to an optimum position for the PD array.

[5] This was either done with occasional IMC resonance flashes or by building a beam path around the IMC as described in [MMT+14].

4.4.2 Electronics

A crucial part of the readout are the first stages of the readout electronics, because the anticipated current noise level is close to the limit of the electronics noise of state-of-the-art OPs. The electronics for the second loop are split in two parts. A PD readout electronics is located close to the vacuum chamber and an analog servo electronics in the electronics rack with the other PSL electronic modules (Fig. 4.10).

In most cases the power sensed with a PD does not change much, such that electronics can be optimized for a certain photo current. This is different for the PDs used as second loop sensor. Since the transmission ratios for in vacuum optics are fixed a wide range of photo currents has to be processed without being limited by electronics noise. In the early days the Interferometer will operate at 12.5 W and then the power will be increased throughout the commissioning to 125 W [Bftat12] entering the PRC.

It is the target to have 10V DC level at the output of the transimpedance amplifier at the maximum power level. The current noise at the input of the transimpedance amplifier consists of [Hei99]:

$$\tilde{I}_{el} = \sqrt{\frac{4kT}{R} + \tilde{I}_{op}^2 + \frac{1}{R^2}\tilde{U}_{op}^2}. \tag{4.16}$$

The first term describes the thermal noise (Johnson noise) of the transimpedance resistor R, Boltzmann constant k at temperature T. $\tilde{I}_{op}$ and $\tilde{U}_{op}$ are the input current noise and voltage noise of the operational amplifier, respectively. Both terms contribute due to the feedback circuit. Since all noise contributions are uncorrelated they add in quadrature.

The choice of R depends on the signal strength. The higher the photo current the lower R has to be, which on the contrary raises the Johnson noise contribution. Unfortunately, there is additional f^{-1} noise in electronic components that exceeds the thermal noise at low Fourier frequencies. Using multiple PDs and thereby splitting the photo current relaxes the noise requirements for the readout electronics and avoids using high voltage OPs.

Each photodiode is read out with an independent transimpedance amplifier and the signal is amplified in a subsequent filter stage, before the signals are summed. Four PDs are combined as in loop sensor and the other four are dedicated to do an independent out of loop measurement. Furthermore the single PD readouts are sampled with the data acquisition system as illustrated in Figure 4.10. That way, the loop can be done digitally or with analog electronics. As long as the signals are not summed any differential delays or additional noise in the signal processing destroys the correlation of the signals and must be avoided.

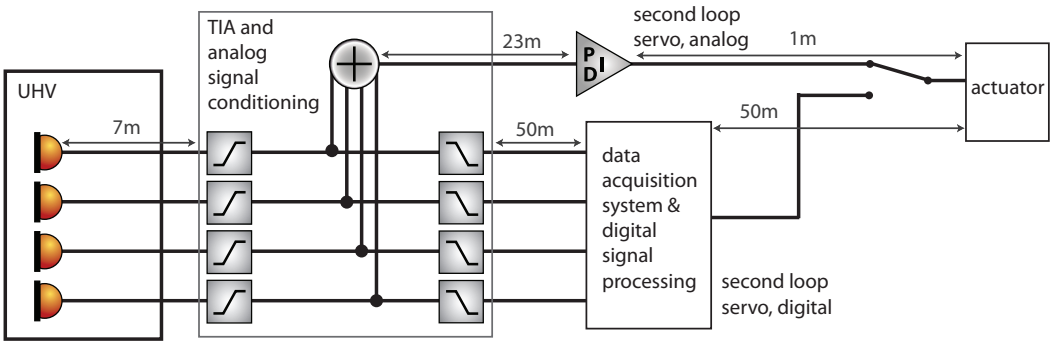

Figure 4.10: Readout of four PDs. There is an equivalent scheme for the other four PDs. The PD signal is acquired outside the vacuum and processed either digitally or with analog electronics and fed to the actuator.

For the low noise readout the AD797 is chosen in the transimpedance amplifier (TIA) stage, because it provides very low voltage and current noise. It can also sink 50 mA current, which supersedes a subsequent current buffer. At very low photocurrents it is better to use field-effect transistor (FET) OPs instead of using bipolar junction transistor (BJT) operational amplifiers like the AD797, because their input current noise is lower.

The PDs are reverse biased with 5 V to improve their response. Due to the long cables connecting the PDs with the readout electronics the transimpedance amplifier and the bias voltage have to be compensated to be able to drive the high capacitive load. The photo diodes have typically 100 pF shunt capacitance. However, in a combined impedance measurement of cables and PD the capacitance turned out to be 1.4 nF.

Relevant properties of the Excelitas C30642 PDs are given in table 4.1. The measurement of these parameters and a study of the influence of bias voltage fluctuations, temperature increase on the PD chip and the behavior at Fourier frequencies around 10 Hz, where the noise increases was conducted in [Sei09]. All the parameters are such that they are not limiting the stabilization at Fourier frequencies of interest. However, critical parameters like dark noise and dark current noise were checked for each PD before it is built into the PD array.

4.4.3 Actuator

The control signal of the second loop is fed back to the error point of the first loop. Hence the closed loop response, a laser power modulation caused by a voltage modulation that is injected to the error point, can be interpreted as the

actuator for the second loop. Since the signal conditioning filter of the first loop PD is part of the sensor block and thus before the error point summation point (Fig. 4.3) the expected shape of the actuator looks like the inverted first loop PD signal conditioning filter as long as the second loop signals are well within the bandwidth of the first loop.

Figure 4.11 shows the simulation and measurement of the actuator transfer function for two cases. In the first one the first loop sensor is upstream of the IMC in the other case it is located downstream of the IMC. The measurement was done by injecting a swept sine into the error point of the first loop while observing the response on the second loop sensor. It is calibrated in Watt in the main beam per Volts applied to the error point, such that the only parameter that might change is the power in the main beam.

Measured and simulated results agree very well. The only difference in setting up the first loop sensor downstream of the IMC is that the IMC pole has to be considered (see Section 4.5). However, at the UGF of the second loop this difference only produces a small effect in the phase. Consequently, it does not matter for the shape of the second loop if the first loop sensor is installed upstream or downstream the IMC. The difference in proportional gain is due to the fact that the first loop gain distribution differs for the first loop sensor downstream of the IMC.

To determine the actuator range a sine wave at a certain frequency was injected to the first loop error point. The amplitude was increased up to the point at which the first loop was not able to hold the error point at zero and started oscillating. For injected amplitudes less than 8.5 V_{pp} and below 3 kHz the error point stayed close to zero.

4.4.4 Loop design

From the measurement of the laser noise downstream of the IMC (Sec. 4.3.2) and the requirements set by the power noise coupling to the IFO dark port (Sec. 4.1.4) some parameters can already be set. The feature at 300 Hz in the power noise spectrum downstream the IMC (Fig. 4.6) must be suppressed by more

quantum efficiency	0.92
dark noise	1 µA
dark current at 1Hz	0.15 pA/$\sqrt{\text{Hz}}$
dark current at 10kHz, 1Hz	0.03 pA/$\sqrt{\text{Hz}}$
capacitance with 2V reverse bias	108 pF

Table 4.1: Properties of Excelitas C30642 according to data sheet

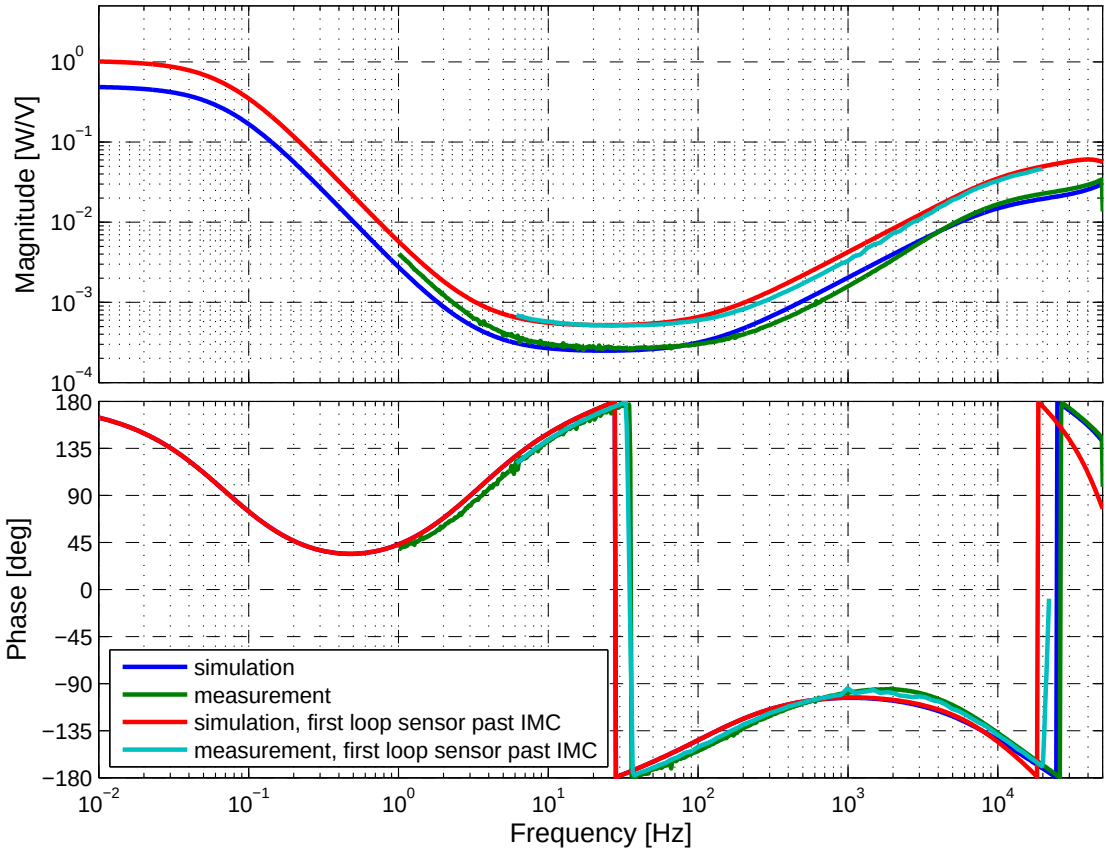

Figure 4.11: Simulations and measurement of second loop actuator transfer function with a main beam power of 1 W.

than a factor of 10. This leads to a required UGF greater than 3 kHz. A similar value is calculated by looking at the noise at 10 Hz. A suppression of 3 orders of magnitude is required here. Assuming a second zero at 100 Hz in the second loop servo the UGF has to be higher than 1 kHz to meet this requirement.

To get a more relaxed noise requirement for the later filter stages it is important to increase the signal of interest immediately after the transimpedance amplifier, while reducing the DC signal at the same time in order to avoid saturation in the electronics. The design chosen is the same as that used in [KWD09] with a DC attenuation of 0.1 and 35 dB amplification of the signal at Fourier frequencies between 10 and 10 kHz in front of the summation point of the signals from the PDs (Fig. 4.10). The DC coupling requires a reference voltage subtraction at the error point.

A graph including all simulated signal transfer functions that contribute to the second loop is shown in Figure 4.12. The transfer functions are displayed

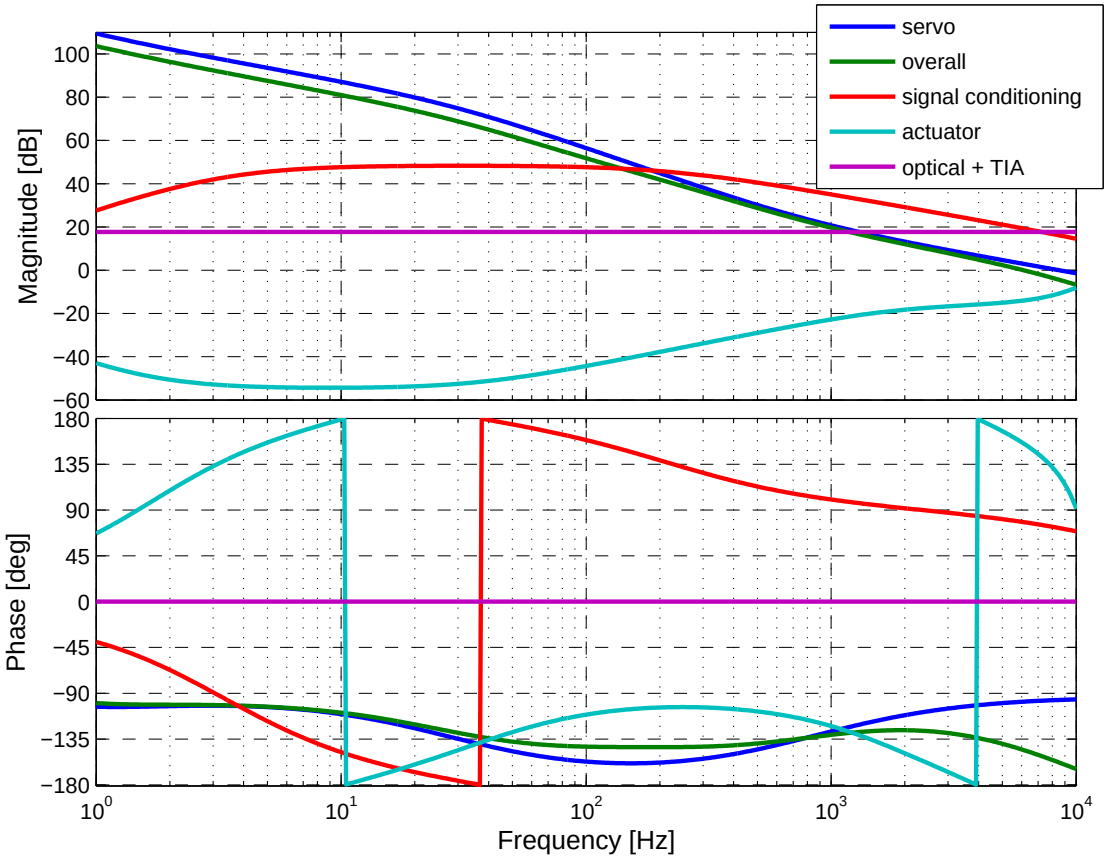

Figure 4.12: Simulation of individual transfer functions of the servo (blue), the signal conditioning (red), the actuator (turquoise) and the optical path including the TIA (purple) that sum up to the second loop transfer function (green).

in their physical units given in dB for example dB V/W for the optical and TIA path. Adding up all transfer functions yields the overall servo transfer function. Since the actuator signal has the inverted shape of the first loop PD signal conditioning filter, a similar shape of the second loop signal conditioning filter equalizes the frequency dependence of both.

However, this has to be kept in mind because a big gain difference might cause saturations in the electronics. The frequency dependent shape of the control loop is accordingly influenced by the shape of the controller transfer function.

The resulting simulations of transfer functions for the first and the second loop are shown in Figure 4.13. To ensure a stable operation of the second loop the UGF of the first loop has to be above 50 kHz. The simulated cross over be-

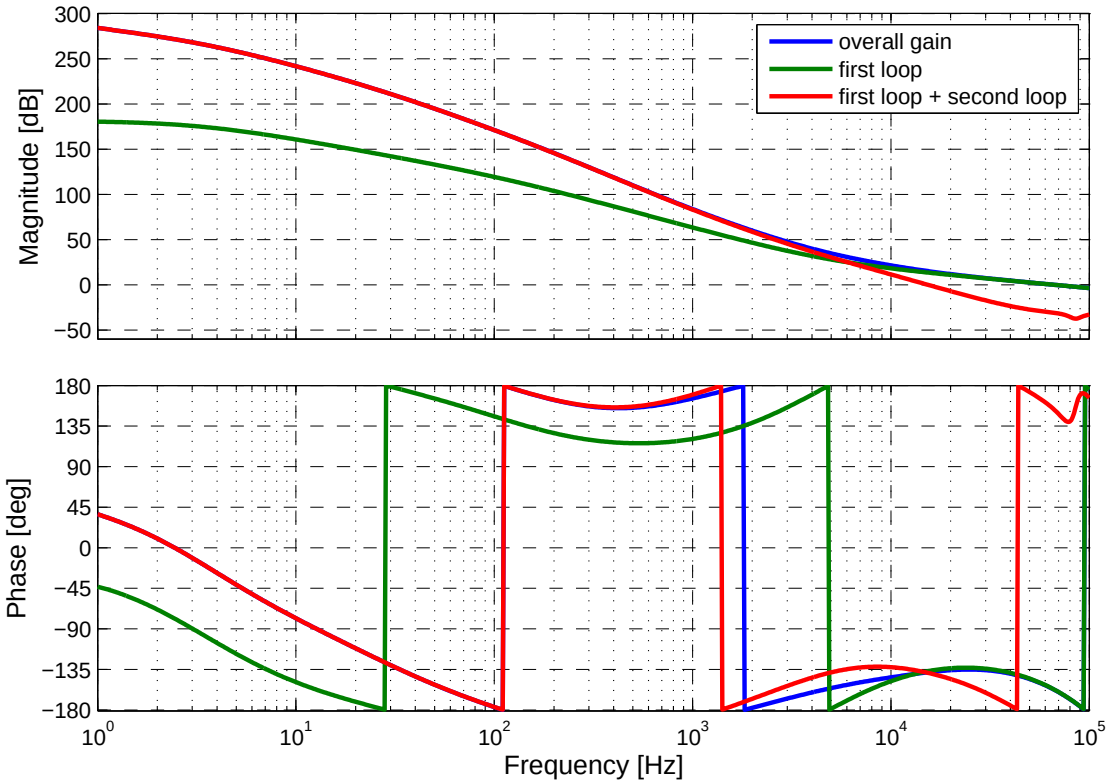

Figure 4.13: Simulation of the loop transfer functions of the first loop, a combination of first and second loop and the resulting overall gain.

tween the two loops is at 6 kHz and the UGF of the second loop can be adjusted between 2 kHz and 8 kHz. At 10 Hz the second loop has a loop gain of 80 dB, roughly a factor 10 more than required.

All simulations were done with 1 W main beam power as this power setting is selected in the measurements that are described in the following.

4.4.5 Limits of a digital loop

Before the sensor for the second loop was installed in the vacuum system, a test of a digitally controlled second loop was conducted. The advantage of having a digital servo is that the loop shape can be changed very fast and easy. In case of the real-time system that aLIGO uses it is possible to change or adjust a filter without interrupting the real time process.

For this experiment a 3 mm Exelitas C30665 PD was used as sensor in a similar scheme as shown in Figure 4.10, but just with a single PD. The location of the sensor was downstream of the IMC, but outside the vacuum system. Analog

signal conditioning is required to make the signal larger than the electronics noise of the data acquisition system.

With this setup a UGF of 600 Hz and a phase margin of 35 degree is achieved. The phase is 180 degree at approximately 1 kHz. As this is not sufficient to fulfill the goals for the second loop an investigation of the reason for the phase lag was done.

A loopback test, where output and input of the data acquisition system were directly connected, reveals that there is a 150 µs time delay which corresponds to five cycles when the real-time model runs at 32 kHz. At 1 kHz the phase lag caused by the time delay is 55 degree. An additional phase lag is caused by the 3rd order low pass in the anti-aliasing and anti-imaging filter. As long as the noise is not dominating the signal, the effect from the filters can be compensated. However, it will be impossible to build a digital loop with a UGF of 5 kHz or more. Therefore an analog servo electronics was chosen for the second loop. The time delay introduced by the 100 m long cables between the experiment and the data acquisition has an insignificant effect on the phase at a Fourier frequency of 5 kHz.

4.4.6 Performance with analog loop

For the LLO measurements presented in the following Sections four PDs are combined (Fig. 4.2) for the in-loop measurement that sense 975 µW altogether. The out-of-loop measurement is done with the remaining three PDs and a summed power level of 650 µW[6]. Since the photo current at these power levels is on the same order of magnitude as the input current noise at 10 Hz of the AD797, a FET OP (OPA140) was used instead and a 10 kΩ transimpedance resistor.

Figure 4.14 shows various power noise measurements with the PD array measured using a Stanford SR785 signal analyzer. Without the second loop feedback the power noise already differs from the noise that has been measured before (Fig. 4.6). As the beam was still not hitting the sweet spot of all PDs at the same time there is an uncorrelated increase in the noise level at low Fourier frequencies which appears in the out-of-loop measurement. The same effect arises, if a beam is clipping at the edge of the active area of a PD. This noise coupling scales with seismic excitations and couples via mechanic components. Since the isolation of the suspended optics towards higher Fourier frequencies is better, the impact decreases.

A projection of the noise without stabilization that was divided by the loop gain agrees very well with the in-loop measurement at high Fourier Frequen-

[6]Due to contaminations found on the IMC optics it was not possible to increase the power at the time of the measurement.

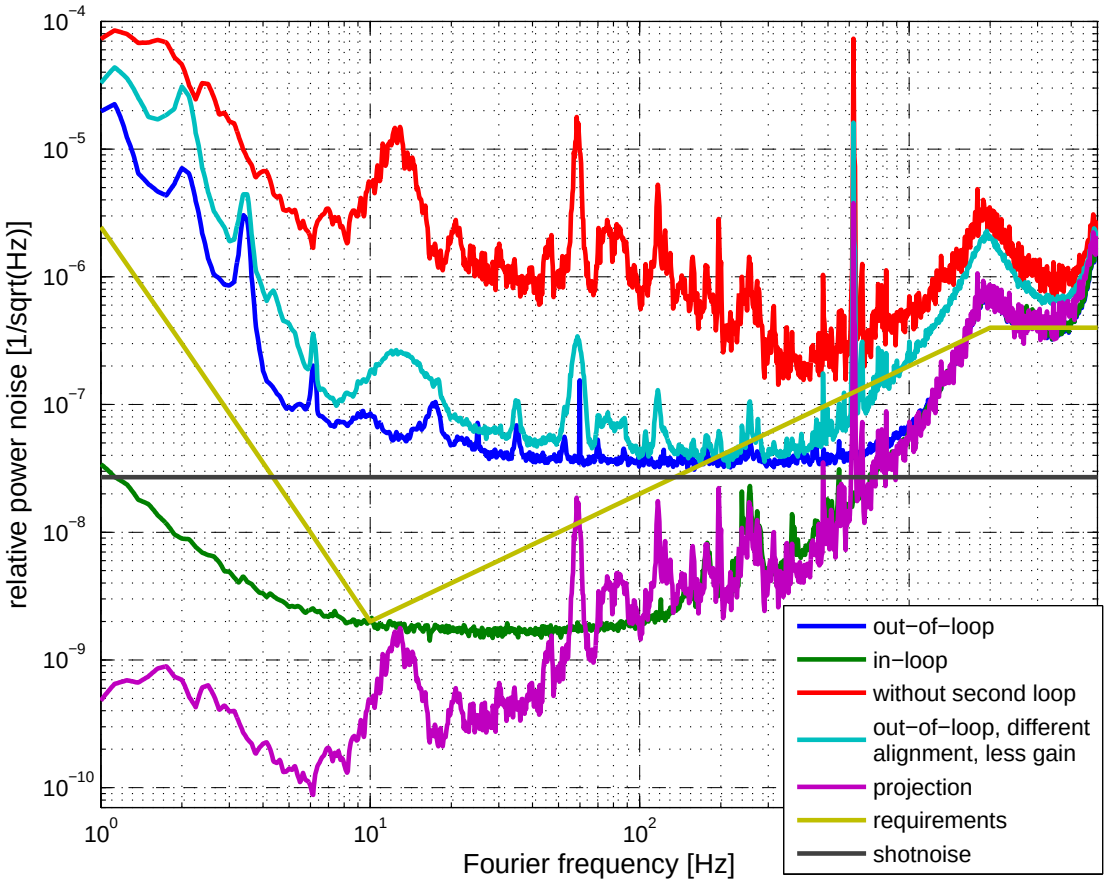

Figure 4.14: Measurement of power noise with the PD array: Without stabilization (red trace), stabilized out of loop with best alignment configuration (dark blue), stabilized with different alignment and limited by saturations at high Fourier frequencies (light blue), stabilized in loop (green) and a projection of the unstabilized trace divided by the loop gain (purple).

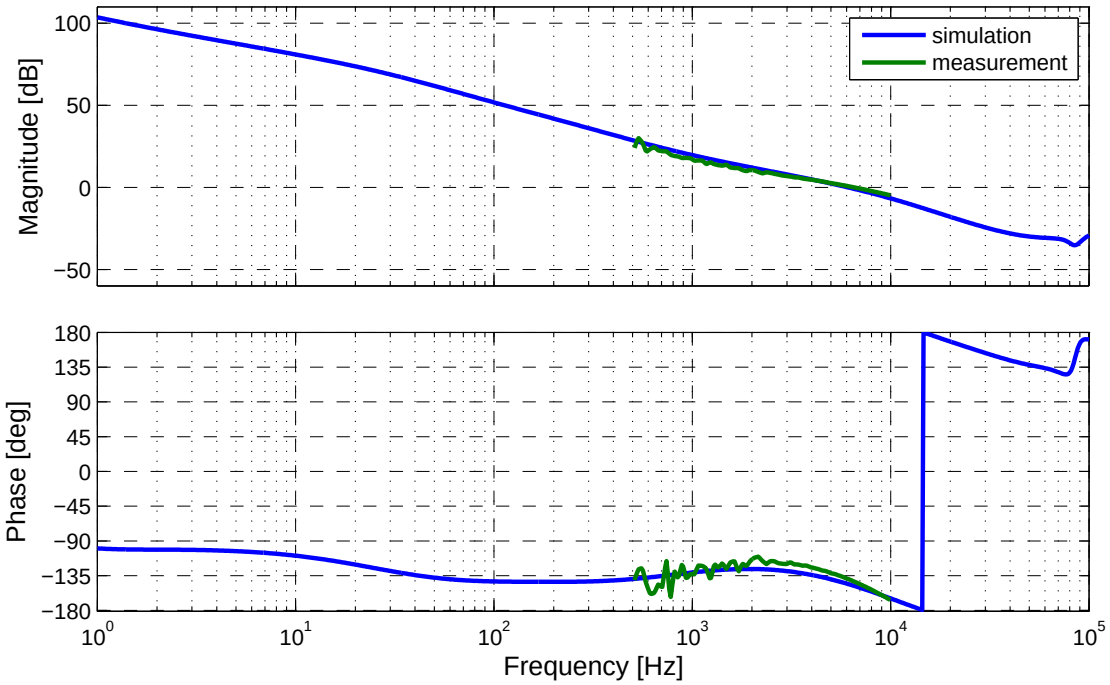

Figure 4.15: Comparison of simulation and measurement of the second loop transfer function.

cies, whereas at low Fourier frequencies the in-loop measurement is dominated by electronics noise of the analyzer. There are features at 60 Hz and 105 Hz where the projected noise is higher than the in-loop noise, because the power noise measurement without stabilization was done with the same alignment as the light blue out-of-loop measurement. Afterwards a different alignment was chosen and the noise around 15 Hz improved. The in-loop and dark blue out-of-loop measurements in Figure 4.14 were done with the improved alignment.

The out-of-loop measurement is basically quantum noise limited at $3.5{\cdot}10^{-8}/\sqrt{\text{Hz}}$ from 30 Hz to 500 Hz and loop gain limited above 500 Hz. In case of the misaligned out-of-loop measurement the loop was saturating the variable gain amplifier stage resulting in less noise suppression at Fourier frequencies above 400 Hz. After redistributing frequency dependent gain in the second loop servo the saturation went away. The shot noise level is 3 dB below the out-of-loop measurement, because there is roughly the same amount of power in the in- and out-of-loop beam.

The loop transfer function was measured and compared with the simulation. Measurement and simulation agree very good as shown in Figure 4.15. The UGF of the second loop is 6.5 kHz with a phase margin of 35 degree.

4.5 Single loop with sensing past the Input-Modecleaner

Instead of using the PD array inside the vacuum system for the second loop, a different first loop sensor outside the vacuum, but in transmission of the IMC was installed. The sensor is a copy of the first loop sensor and the PDs are housed inside a box [KBD+12]. While the main beam injected to the IMC contains 1 W, this leakage beam of one of the steering mirrors downstream of the IMC has 330 µW power, and is equally split between in and out of loop PD. In this configuration power stabilization downstream of the IMC is possible with only one sensor, while simultaneously operating the IFO.

An advantage of this setup is that the loop gain can be much higher than for the nested loop case. However, operating the first loop with a sensor downstream of the IMC an electronic pole compensation is necessary for a stable control loop operation at a high bandwidth.

Hence a compensation filter was built that had a zero at the IMC pole frequency of 8.8 kHz. Furthermore a proportional gain of 21.5 dB was implemented to compensate for low power of the incident beam. Due to the limited bandwidth of the OP, the compensation does only work up to 10 kHz like an inverted low pass and loses phase above.

Figure 4.16 shows the transfer function of the single loop power stabilization with the sensor downstream of the IMC. Compared to the setup with the first loop sensor downstream of the PMC (Fig. 4.4) the phase already reaches -180 degree at 60 kHz, whereas in the other case it does at 92 kHz. As mentioned above this difference arises, because of the IMC pole compensation filter shape. Furthermore the optical path length increases by approximately 55 m, which causes additional time delay of 0.18 µs. To keep some phase margin the UGF is set to 50 kHz.

Since the first loop sensor downstream of the PSL is disconnected the power noise measured is the unstabilized power noise, which is mostly dominated by noise of the pump light in the 35 W laser [FSW+07]. Above Fourier frequencies of 20 kHz the noise starts rising again, because electronics noise of the readout is limiting the measurement (Fig. 4.17).

Figure 4.17 contains three out-of-loop measurements at different positions inside and outside the vacuum system. The one outside the vacuum system was done with the PD in the sensing box, next to the in loop PD. It is shot noise limited at $1 \cdot 10^{-7}/\sqrt{\text{Hz}}$ between 5 Hz and 5 kHz, except one hump at 13 Hz. At the UGF there is some noise peaking that exceeds the unstabilized noise by more than an order of magnitude. Below 5 Hz the noise rises possibly due to scattered light or pointing coupling due to a non uniform response of the PD

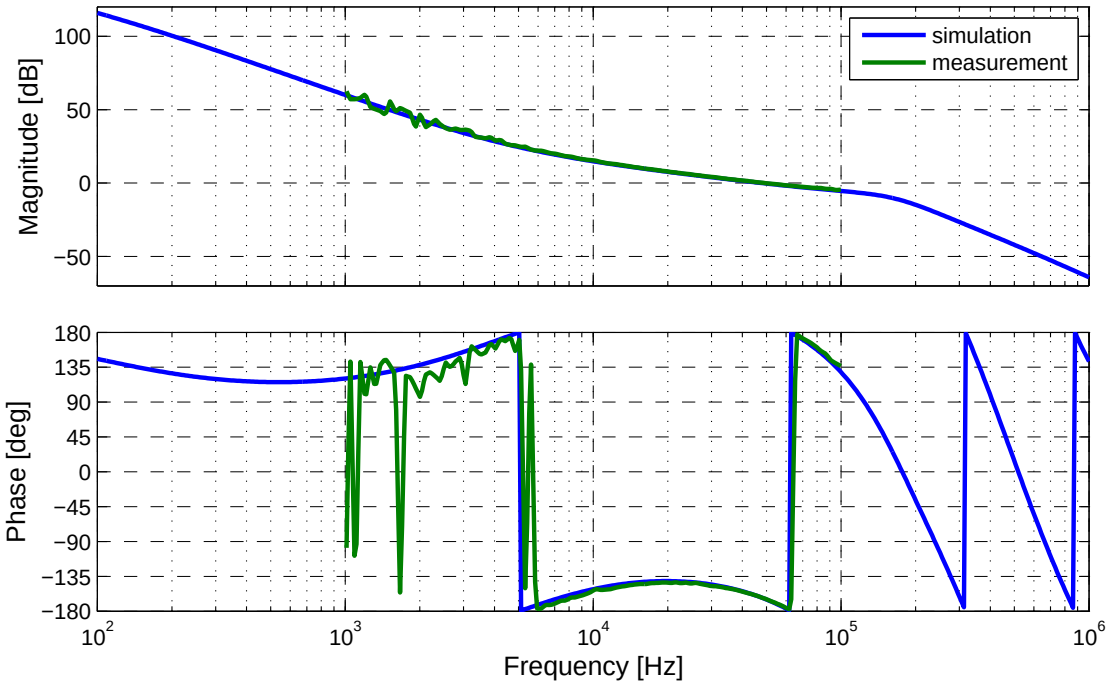

Figure 4.16: Transfer function of first loop with sensor downstream the IMC and additional IMC pole compensation.

across the active area. The electronics noise is about a factor of five lower than the quantum noise and dominated by Johnson noise of the resistor in the TIA feedback up to 1 kHz.

The other two out-of-loop measurements were recorded with the CDS. Due to the sampling rate limitation of the two CDS models these channels could only be resolved up to 900 Hz and 8 kHz. Both were done with in vacuum sensors. The shot noise limited sensitivity is lower because the power level on the out of loop detectors was higher. The first one uses the sum of four PD array detectors and is electronics noise limited for Fourier frequencies above 2 kHz. The second measurement is taken at the output of the IFO, while one arm is misaligned and the beam is reflected off one ITM and then directed towards the output port. In both measurements the noise increases below 80 Hz with the same slope and below 10 Hz another noise source is dominant in the single bounce measurement. From the shape of the noise this looks like noise introduced by scattered light, which was confirmed by a subsequent measurement. The elevated noise level in both measurements is likely due to clipping noise which was already observed when the second loop was characterized (Fig. 4.14). Note that the measurements with the PD array had to be taken at a different time than the

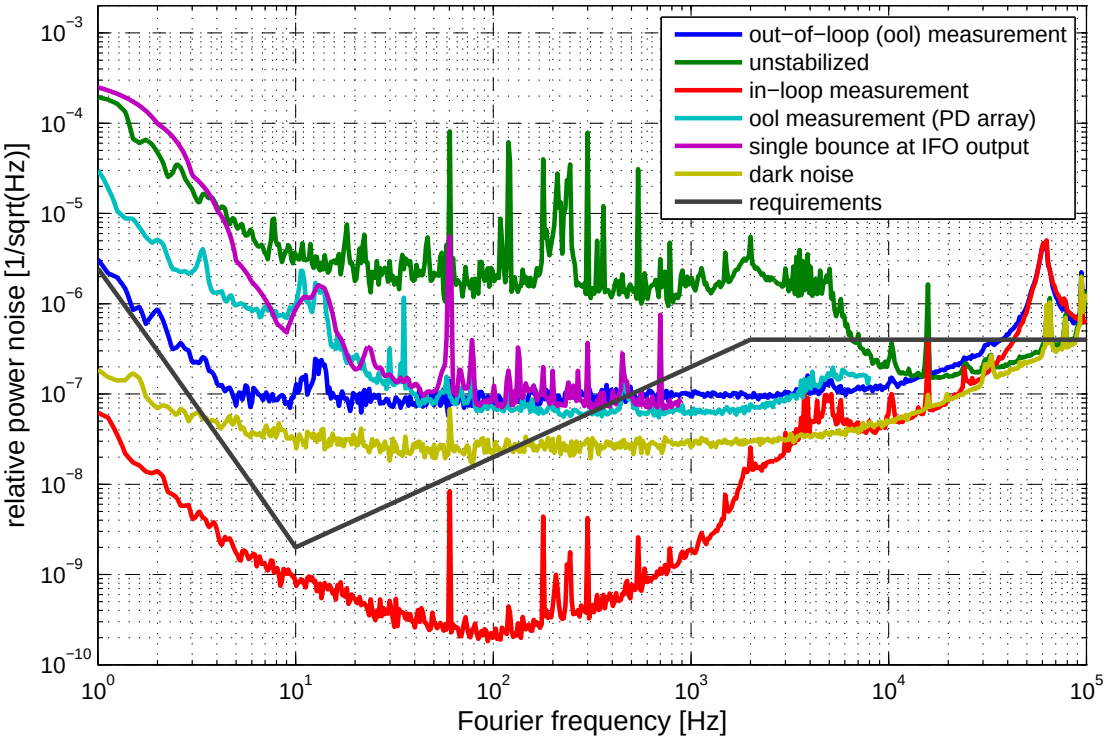

Figure 4.17: Relative power noise with the first loop sensor past the IMC. The purple curve is a measurement at the IFO output, when one ITM is misaligned; A second in vacuum out of loop measurement with the PD array (turquoise) and one with the out of loop sensor (blue) next to the in loop sensor (red). Without stabilization the green curve is obtained and the yellow trace shows the electronics noise of the readout without light on the PD.

one at the IFO output, because both sensors could not be aligned at the same time (Sec. 4.4.1) and therefore it was not possible to obtain a correlation measurements.

The hypothesis that the hump at 13 Hz is caused by residual pointing on the PD is confirmed by taking a coherence measurement with the wavefront sensors (WFSs) that are used for DWS in reflection of the IMC. The Gouy phase difference between WFS A and B is 90 degrees such that angular and transversal movement of the beam is detected. Figure 4.18 shows up to 0.8 coherence in pitch and 0.4 in yaw. The origin for the high coupling could either be a differential motion between the suspended table in vacuum with respect to the table supporting the in-loop sensor or a non optimal alignment of the sensor.

In order to suppress the peaks at 2 kHz and 4 kHz sufficiently a loop with a

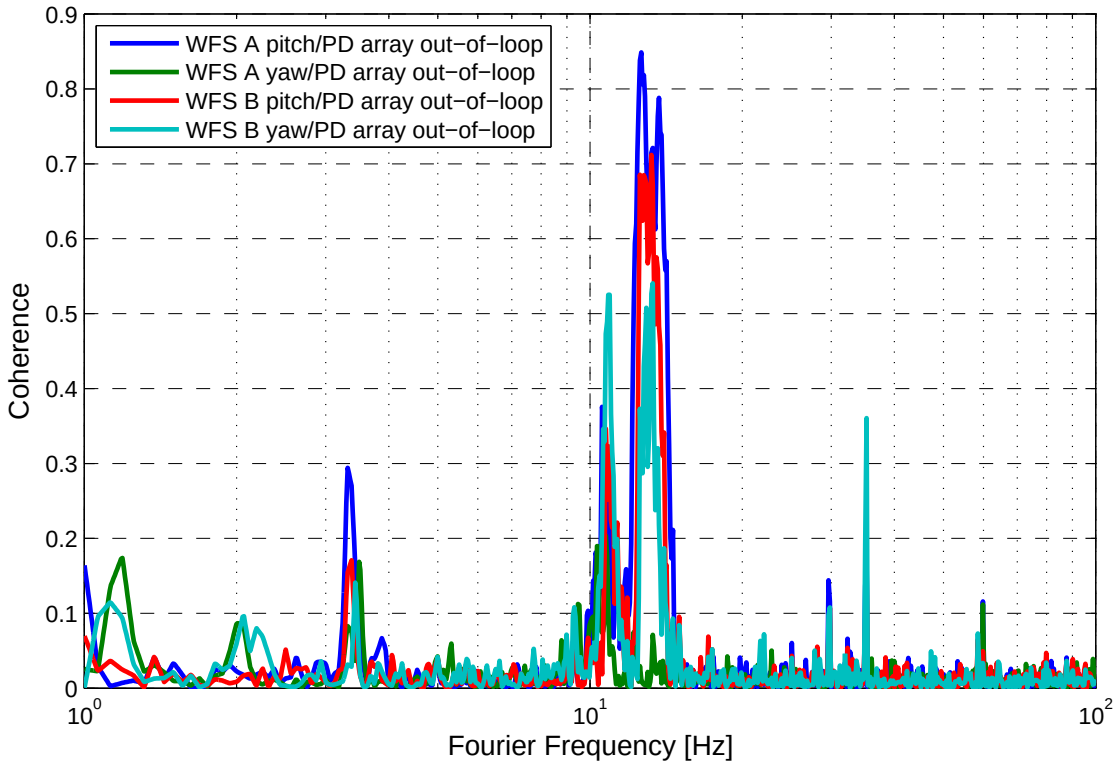

Figure 4.18: Coherence measurement of the PD array out-of-loop PD with two quadrant PDs in reflection of the IMC.

bandwidth above 10 kHz is required. This is only possible with the first loop sensor downstream of the IMC. Apart from the gain peak at 50 kHz, which can be reduced by lowering the UGF, the in-loop noise is well below the requirements down to 500 Hz. However, this sensor is only designed for a maximum power of 4 mW which corresponds to a shot noise limit of $1 \cdot 10^{-8}/\sqrt{\text{Hz}}$. Another problem is given by the excess noise around 10 Hz at the IFO input.

4.6 Future prospects

In the future the PD array alignment needs to be improved in order to be consistent with a good IFO alignment and to lower the noise at low Fourier frequencies. This includes setting up the new beam path with an extended Raleigh range for the PD array beam according to [MWG+14]. The alignment has to be very precise as it was recently found that only a slight misalignment might cause a second beam from a secondary reflection of the beam splitter to hit at least one of the PDs [Vaj14]. Furthermore, the broken PD should be fixed, the

QPD transimpedance amplifier modifications should be implemented and the pointing to power noise coupling coefficient needs to be checked by modulating one of the suspended steering mirrors.

The control loop shape is easier to change, if a split digital and analog controller is used. In this case the analog controller ensures a high bandwidth at high Fourier frequencies, while a digital controller is used at Fourier frequencies up to 500 Hz.

By increasing the power directed towards the IFO further the shot noise limited sensitivity for the second loop power stabilization will be improved. So far $8 \cdot 10^{-9}/\sqrt{\text{Hz}}$ is, to my knowledge, the best power stability achieved in a large scale GWD [BBC+02, Noc04]. If it turns out that the power noise coupling to the IFO output signal is worse than expected, the shot noise limited sensitivity can be improved by $\sqrt{2}$ when all eight PDs are summed and used as in-loop sensors.

Although the second loop has enough loop gain to reach the requirements at 10 Hz, there is not enough gain to suppress noise above 1 kHz. To increase the gain, a higher first loop bandwidth is required (Sec. 4.3.1) or the sensor for the first loop has to be located permanently downstream of the IMC. The best action, however, is to find the source for the increased noise in the kHz region and to eliminate it.

The HPO had been switched off for these measurements. However, it is required, if the IFO is operated with more than 30 W. Since the pointing noise increases in high power mode [KBD+12] the power noise downstream of the IMC will increase as well. The characterization of the PSL in high power mode revealed an unknown noise below 100 Hz in the power noise spectrum [Bog13]. It was suspected that this is caused by scattered light, which is hopefully separated from the main beam and blocked before it reaches the PD array.

4.7 Summary

The first PD array designed by LIGO scientists was installed in the LLO vacuum system. Problems that were found during installation (Sec. 4.4.1 and 4.4.1) were addressed and improvement is in progress.

It is essential to have an in vacuum sensor for the second loop power stabilization, since the stringent noise requirement at low Fourier frequencies cannot be reached with a comparable in air sensor. This was shown by a comparison of sensors in the two locations in Sections 4.4.6 and 4.5.

A computer model developed (Sec. 4.2) for the power stabilization agrees very well with the measured results and was used to design the PD readout electronics and the servo for the second loop power stabilization (Sec. 4.4.4).

Analog electronics is preferred for the second loop as a digital loop is limited by time delay of the real time computer system (Sec. 4.4.5). However a split digital and analog controller has further advantages (Sec. 4.6). Investigations concerning the bandwidth limit for the first loop are conducted in Section 4.3.1, because more gain of the second loop at Fourier frequencies above 1 kHz is necessary to fulfill the power noise requirements.

A quantum noise limited power stabilization over a wide frequency band from 30 Hz to 500 Hz was achieved with the PD array (Sec. 4.4.6). The performance will be improved by injecting more power towards the IMC, which was unfortunately not possible at the time of the measurement due to contamination control issues in the LLO IMC.

While the IMC adds power noise at low Fourier frequencies (Sec. 4.3.2), it is an essential part of the frequency stabilization loop and used as sensor for frequency fluctuation. The frequency stabilization is described in the following Chapter.

5 Frequency stabilization

Frequency fluctuations do not influence the performance of a GWD if both interferometer arms have exactly the same effective length. However, this is not the case in the real experiment due to material imperfections of the optics and intentionally introduced arm length offsets. Therefore the laser frequency is stabilized to stable frequency references in a nested control scheme.

On long time scales atom transitions are very stable and therefore they are used to provide the worlds most precise clocks [CHK+10, YDD+11]. Since the GWD is most sensitive at Fourier frequencies of 10 Hz and above, atom clocks are not suited as frequency reference as the phase noise at these frequencies is too high. Instead the laser frequency is compared to the resonance frequency of the IFOs averaged arm length. Due to the sophisticated seismic isolation and suspension system and the 4 km long resonator this is the most stable frequency reference above 10 Hz [LFR+02, AAA+09b].

A nested scheme is required as it is not possible to impose the gain that is required to suppress the unstabilized laser frequency noise with a single control loop. A plot of the typical NPRO frequency noise and the requirements for the individual subsystems are shown in Figure 5.1 [WKSF11, AMM+09, ABF08]. The requirements for the PSL and IMC are plotted with dotted lines as they depend on the gain distribution between the nested control loops. At 10 Hz the laser frequency noise has to be suppressed by more than ten orders of magnitude. While at low Fourier frequencies active stabilization is applied, the frequency noise is filtered passively by the PMC and IMC above their pole frequencies.

Due to improvements in precision in optical fabrication arm length imbalances are less severe in aLIGO compared to initial LIGO (iLIGO) and therefore the requirements in terms of frequency stability did not get more stringent than

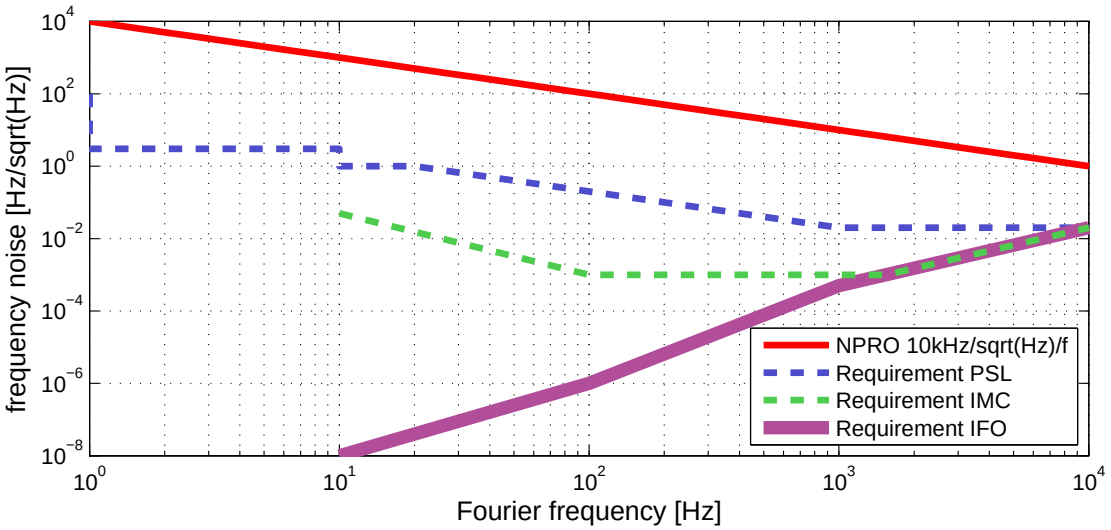

Figure 5.1: Frequency noise requirements for the PSL, IMC and IFO. The requirements for the PSL and IMC can change with respect to the gain distributions in the nested control loops.

they have been for iLIGO. Hence, the same topology of frequency stabilization can be used. However, the old scheme has to be adapted to the aLIGO infrastructure and effects caused by the addition of the HPO need to be characterized and taken into account.

In the first part of this Chapter the unstabilized laser frequency noise is analyzed in Section 5.1. The LIGO frequency stabilization scheme is reviewed (Sec. 5.2) and the characteristics of the aLIGO scheme are pointed out. A detailed description of the control loop is given in Sections 5.2.1, 5.2.2, 5.2.3 and 5.2.4 and the performance of the loop is presented (Sec. 5.3). Most of the measurements presented in the first part were taken at the Reference System.

The second part of the Chapter (Sec. 5.4) describes the 32 m long, in vacuum resonator, called IMC, which is used for subsequent frequency stabilization. The IMC at LLO is used for an out-of-loop measurement of the reference cavity frequency noise (Sec. 5.4.1) and was further tested and characterized with input power levels up to 120 W in Section 5.4.2. At the end of the Chapter future prospects are described (Sec. 5.5).

5.1 Laser frequency noise

The NPRO frequency noise has been measured in multiple experiments (for example in [Day90, Bro99]) and its linear spectral density can be estimated with

$s_\nu = \frac{10}{f}\frac{\text{kHz}}{\sqrt{\text{Hz}}}$. All NPROs that are operating in the aLIGO lasers have been characterized in [KW08]. The frequency noise from the 35 W laser consists of the noise generated by the NPRO and the amplifier. However, the frequency noise that is added by the amplifier was measured in a beat signal measurement [Kwe05] was found to be well below the NPRO frequency noise for frequencies below 100 kHz.

A fundamental noise limit is set by the so called Schawlow-Townes limit [ST58] resulting from spontaneous emission of photons from the upper state into the laser mode. A quantum mechanical description was done in [Wis99]. The Schawlow-Townes limit has been derived for a similar NPRO with 800 mW output power to be $40\text{mHz}/\sqrt{\text{Hz}}$ [Bro99].

For the measurement of frequency noise a frequency discriminator is required. The frequency noise measurements in this Chapter are done by comparing the beam that should be analyzed to the resonance frequency of a resonator. As the frequency fluctuations of a resonator are proportional to its length fluctuations, the stability of the reference resonator needs to exceed the one of the test beam. Alternatively the frequency noise can be obtained by a comparison to an ultra stable clock with a phase-locked loop [Gar05].

There are three resonators in the aLIGO PSL system, that can be utilized to analyze frequency noise: the DBB resonator, the reference cavity (Sec. 5.2.1) and the PMC. Among those three the reference cavity is the best frequency reference (Sec. 5.4.1), the stability of the PMC was already evaluated in Figure 3.11 and the DBB resonator stability is characterized in Section 5.3.

The frequency noise measurement is done by locking the resonator with a PDH scheme and obtaining a spectrum of the control- and error signal. For the calibration the error signal is determined while the cavity length is swept. To check the calibration a sinusoidal frequency modulation of known strength at 8 kHz is applied, which is higher than the UGF of the PDH control loop. Since the reference cavity is usually part of a high bandwidth control loop that is actuating the laser frequency (Sec. 5.2) a slow, digital control loop with a UGF of 70 Hz was implemented for this calibration verification, such that the error signal above the UGF represents the laser frequency noise. This loop did not operate robustly in HPM, such that the reference cavity could not be used as frequency noise sensor for the injection locked laser.

For the PDH locking of the DBB phase modulation sidebands are generated by dithering the PZT at 1 MHz. This frequency shows up as a strong peak in the frequency noise measurement.

Power noise originating from the NPRO relaxation oscillation peak is suppressed with a fast control loop, called noise eater (NE) [HGB+94]. The cross coupling of power noise to frequency noise was checked by turning off the NE.

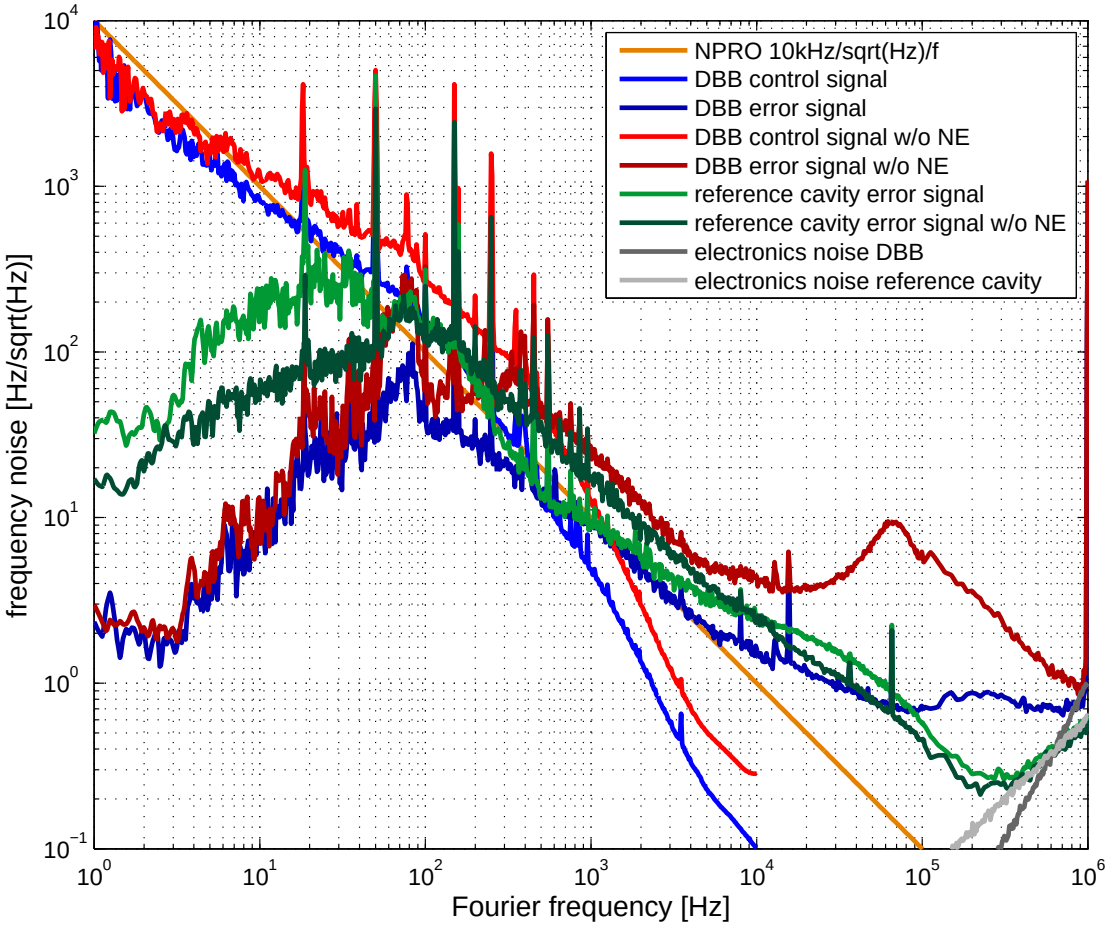

Figure 5.2: Measurement of frequency noise in LPM measured with different frequency discriminators. A typical NPRO frequency noise curve is shown in orange. Control- and error signal were measured with the DBB (red and blue trace) and the reference cavity (green trace) in two different configurations. For the first configuration the NPRO NE was engaged, while it was disengaged for the second one. At low frequencies the measurements follow the typical NPRO behavior whereas at high frequencies the DBB measurement is limited by noise related to power noise or couplings from the dither frequency at 1 MHz.

Figure 5.2 shows a frequency noise measurement of the 35 W laser. In case the NE is activated the DBB and the reference cavity frequency noise measurement agree up to a Fourier frequency of 100 kHz and follow the typical NPRO frequency noise. Above 100 kHz the DBB levels at $8 \cdot 10^{-1} \frac{\text{Hz}}{\sqrt{\text{Hz}}}$ which could be due to power noise coupling or effects from the dither frequency at 1 MHz limiting the DBB readout sensitivity, although the DBB electronics contains a double-pole lowpass filter at 200 kHz. After disabling the NE a broad peak around 65 kHz appears in the DBB spectrum, which is possibly as well caused by a power noise cross coupling. It is, however, not present in the reference cavity measurement. Furthermore, the noise increases in a broad band between 10 Hz and 10 kHz by a factor of two when the NE is disabled. Above 10 kHz the noise in the reference cavity measurement is close to the DBB measurement. The frequency noise in LPM was also measured with the PMC, which is not shown in Figure 5.2. The PMC measurement agrees very well with the DBB measurement at low frequencies and follows the noise measured with the reference cavity up to 100 kHz. Above 100 kHz the PMC error signal is electronics noise limited.

In HPM the unstabilized frequency noise of the HPO is high pass filtered up to the injection locking bandwidth of 2.6 MHz by the injection locking process [FGB95, Win12]. There is additional suppression from the injection locking control loop up to 20 kHz. Therefore frequency noise coupling from the slave laser is if at all expected at high Fourier frequencies as observed in [FGB95, YIO+96] and the frequency noise coupling from the NPRO relaxation oscillation is reduced by the slave laser as well (Sec. 3.1.4).

The frequency noise measurement in HPM is depicted in Figure 5.3. The measurement is only shown up to 100 kHz since the sensors were noise limited above 100 kHz. Compared to the prior LPM measurement the noise in HPM is on the same level up to 100 kHz and thus the HPO does not add frequency noise.

5.2 Frequency stabilization scheme

The unstabilized laser frequency noise exceeds by far the frequency noise acceptable by the interferometer (Fig. 5.1). This has been a serious problem for GWDs in the past and quite sophisticated electronics have been developed to achieve a high control loop gain and accordingly a high bandwidth of the feedback control loop. As argon ion lasers that were used for the first GWD prototypes had at 1 kHz a hundred times worse frequency noise [Zuc89] than the aLIGO laser, frequency stabilizations were built with a bandwidth as high as 2 MHz [KRHM85, HH84].

There have been several experiments with frequency stabilization system us-

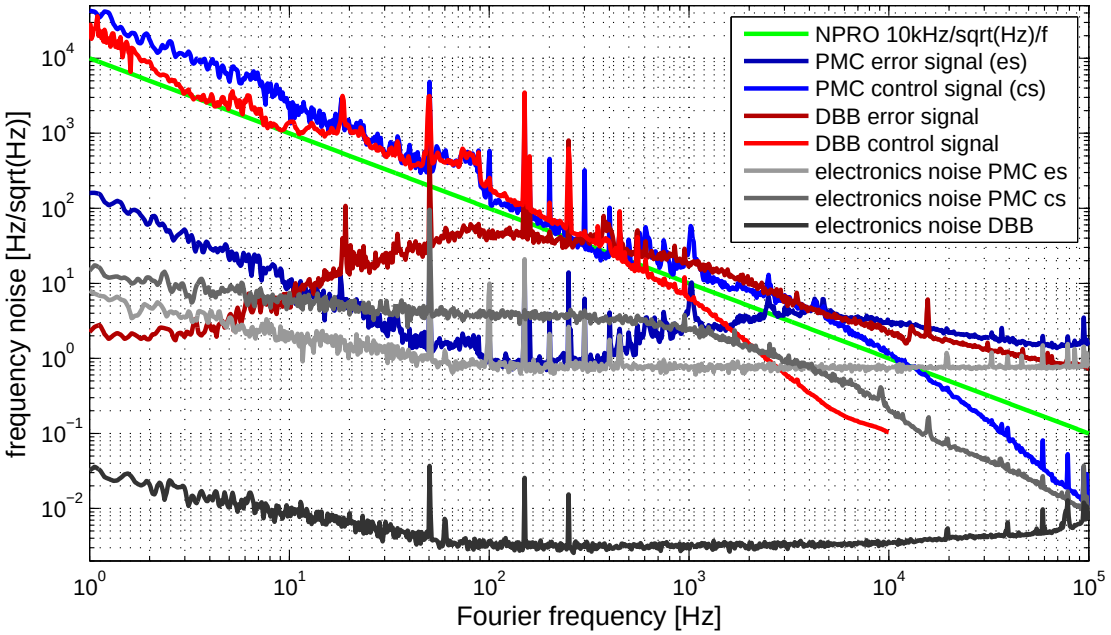

Figure 5.3: Measurement of frequency noise in HPM with DBB (red) and PMC (blue). Both measurements agree very well and follow the typical NPRO noise, that is shown in green. At high frequencies the PMC measurement is electronics noise limited.

ing NPROs [Day90, WBD+00, BFMB96, UU94] and injection locked high power laser systems [NKA+03, Bro99, OMM10]. Most of which only address the pre-stabilized laser and not the full IFO frequency stabilization scheme. The iLIGO frequency stabilization is described in [SKS98] and it was first tested and characterized with a 700 mW NPRO [AMS97]. The frequency stabilization requirements are less stringent for aLIGO than they have been for iLIGO and therefore the existing iLIGO frequency stabilization was adopted.

A schematic overview of the frequency stabilization is shown in Figure 5.4. There are two pictures that show the scheme in different fashions, one of the optical layout and the second is a block diagram to illustrate the important parts for the control loop design and the propagation of frequency noise.

The frequency stabilization that is part of the PSL consists of the reference cavity in conjunction with a PD optimized for RF as sensor (Sec. 5.2.1), which detects a beam that is transmitted from the PMC. The servo electronics is called table top frequency stabilization servo (TTFSS) and is located on the optical table to keep the length of the cables short (Sec. 5.2.2). High actuation range and high bandwidth requirements demand the use of multiple actuators. They consist of an EOM, the NPRO PZT and the NPRO crystal temperature controller

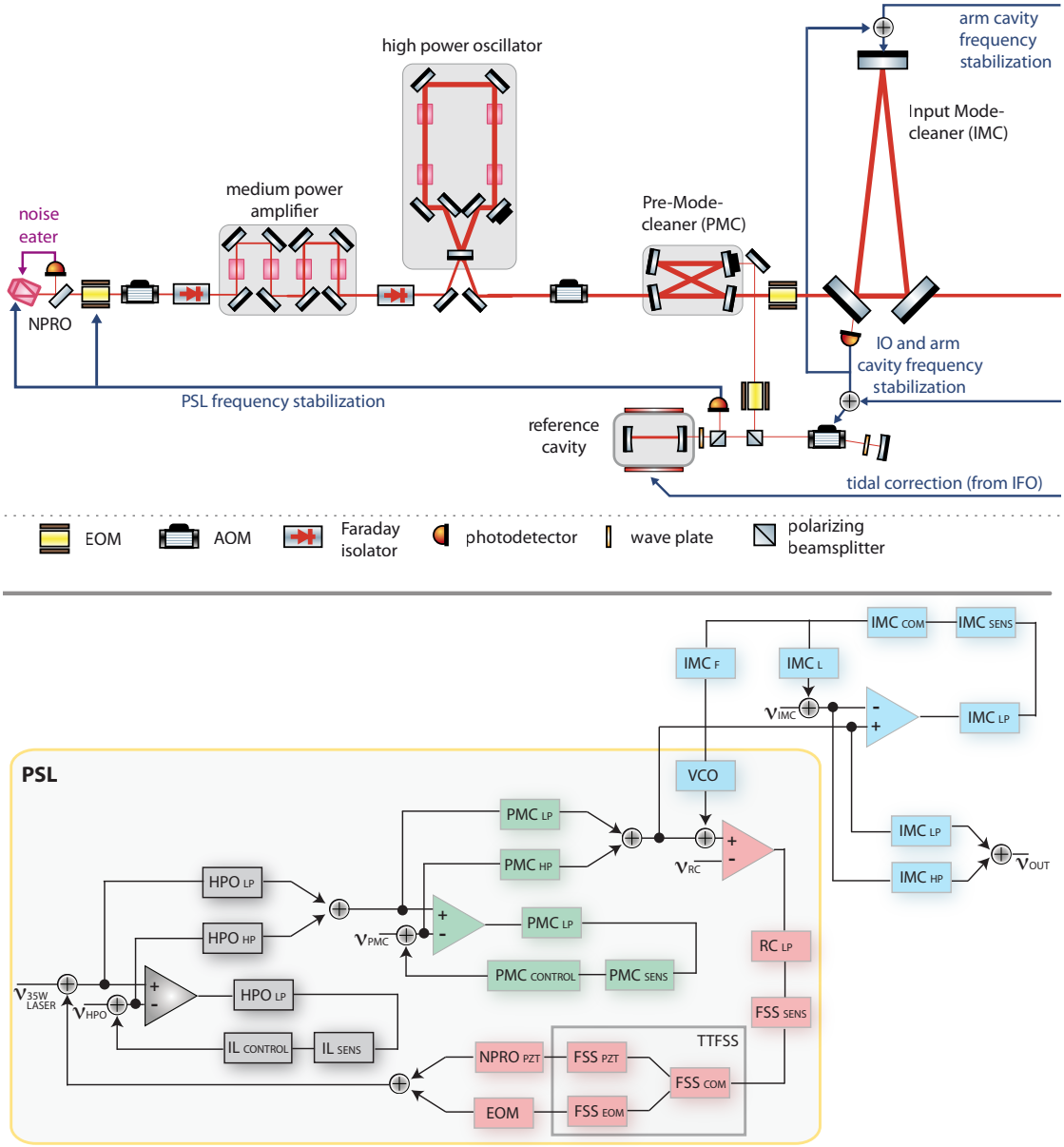

Figure 5.4: Schematic overview and block diagram of the aLIGO frequency stabilization. The frequency stabilization is built as a nested control loop with the reference cavity, the IMC and the IFO arms as sensors and the NPRO crystal temperature, a PZT mounted to the NPRO and an EOM as actuators. (IL: injection locking; SENS: sensor; COM: common feedback path; LP: low pass; HP: high pass; FSS: frequency stabilization servo; IMC_L: feedback to the IMC length; IMC_F: feedback to the laser frequency)

(Sec. 5.2.3). The control is done by a PDH locking scheme and a second EOM in the pick-off beam transmitted by the PMC is generating the phase modulation sidebands at 21.5 MHz. There are two inputs that can be used for an external sensor correction.

A beam transmitted by the PMC is double passing an AOM in first diffraction order and the AOM modulation frequency can be modulated. Moreover, heater pads are attached to the reference cavity tank. Heating the tank causes a thermal expansion of the spacer resulting in slow resonance frequency changes. The control signals of the two other sensors that are part of the frequency stabilization, namely the IMC and the IFO arms are fed back to the AOM via a voltage controlled oscillator (VCO) (Sec. 5.4). The feedback from the IFO arms will not be further discussed here and can be found in [Adh04, AAA+09a]. The IMC works in a split feedback loop as depicted in in Figure 5.4 and will only be used as frequency reference above 15 Hz (feedback via IMC_F). At low frequencies the IMC follows the PSL frequency by adjustment of its round trip length (feedback via IMC_L).

If a beam is passing a resonator it is low pass filtered with respect to frequency noise and the corner frequency equals the pole frequency of the resonator (Fig. 5.4). Length noise of the resonator itself is high pass filtered and imprinted on the output beam [BTD01]. The frequency stabilization of the control loop can additionally suppress the resonator frequency noise or the laser noise depending on the configuration of the control loop. While the HPO and the PMC follow the laser frequency the laser frequency is tuned to the resonance of the reference cavity.

Compared to the iLIGO frequency stabilization the PMC pole frequency was lowered from 1.6 MHz to 578 kHz to achieve a better RF power noise suppression. However, this influences the frequency stabilization control loop as discussed in Section 5.2.2. Moreover, the RF PD is replaced and a different NPRO is used, which changes the actuation coefficients of the crystal temperature controller and the NPRO PZT. A low noise VCO is integrated replacing the iLIGO VCO (Sec. 5.4) and the HPO is added to the setup. Since the aLIGO laser is operated in in HPM as well as in LPM effects of the HPO have to be considered (Sec. 5.2.3), such that the control loop is operating robustly in both modes.

5.2.1 Sensor

In this Section the properties of the reference cavity are summarized and the RF PD is characterized. The reference cavity is used as frequency discriminator in the PDH scheme. Furthermore noise sources associated with the length stability of the reference cavity are reviewed and the temperature control loop is

described.

Reference cavity

The reference cavity is consisting of a 203 mm long, cylindrical fused silica spacer and two curved mirrors are optically contacted to the spacer. The aperture for the beam is 6.35 mm. The mirror substrates have a ROC of 0.5 m and Silica/Tantala coatings. The spacer is attached to a single pendulum stage, that is mounted on a passive vibration isolation stack. For damping of horizontal movements eddy current dampers are used. The reference cavity is sitting inside a tank under ultra high vacuum (UHV). With an ion getter pump the pressure inside the tank is kept below $1 \cdot 10^{-6}$ Pa. The FSR of the cavity is 736.5 MHz and the calculated finesse is 9518 assuming a loss of 30 ppm per mirror due to scattering and absorption. A high finesse of the frequency discriminator is desirable because it increases the slope of the PDH error signal and hence the shot noise limited sensitivity [Bla01].

To evaluate the status of the reference cavities that were already operating for several years a finesse measurement was conducted. A sinusoidal modulation was injected to the AOM used for the power stabilization and a transfer function was measured from a PD at a pickoff upstream of the reference cavity to a PD downstream of it. Table 5.1 shows the results, which reveal that all cavities exceed the nominal finesse. This is probably due to the fact that 30 ppm absorption per mirror was considered as the worst case. However, the cavity pole frequency is between 29.4 kHz and 38.6 kHz. Since there were no prior data available it is not obvious if losses increased due to accumulated contaminations or if the differences have been present from the beginning.

Noise sources associated with the reference cavity

The two main noise sources for the reference cavity are thermal noise and seismic noise. Thermal noise appears as brownian noise in the coating [HGS+02], the substrate and the spacer [Lev98], which is associated with mechanical loss.

detector	finesse	pole frequency
LHO H1	9570	38607 Hz
LHO H2	10816	34157 Hz
LLO	12548	29443 Hz
Reference System	11505	32114 Hz

Table 5.1: Finesse measurement of reference cavities.

Furthermore, there is thermal dissipation that causes thermo-optic noise in coatings [EBF+08] and in the substrate [VB99]. Thermal noise causes fluctuation of the optical path length which can be considered as phase fluctuations. There has been a study by Numata [NKC04] stating that for the spacer geometry of the reference cavity coating brownian noise is the dominant noise. A thermal noise limit was derived and experimentally verified that is [NKC04]

$$0.1 \cdot \sqrt{\frac{1\,\mathrm{Hz}}{f}} \frac{\mathrm{Hz}}{\sqrt{\mathrm{Hz}}}. \tag{5.1}$$

A recent study is conducted at Caltech to probe the thermal noise limit of the LIGO type reference cavity [CSA+13]. In principle thermal noise can be reduced by cooling of the cavity [SSR+97, SBJ+98]. However, the choice of material is important because of the temperature dependent thermal expansion coefficient.

Seismic noise couples via vertical acceleration of the spacer. This leads to a bending of the structure and thus causing a fluctuation in the optical path length. The reference cavity is already suspended, but for more seismic isolation a second pendulum stage could be added. Moreover, mounting of the cavity vertically might be beneficial as well [NRS06, MMaM+09].

The reference cavity tank is a good acoustic enclosure. Keeping it evacuated for a long time reduces the risks of contamination on the optics. The low pressure is, however, required to reduce scattering due to residual gas fluctuation [TSF+02]. At a pressure level of 10^{-6} Pa the equivalent frequency fluctuations are on the order of $1 \cdot 10^{-5} \frac{\mathrm{Hz}}{\sqrt{\mathrm{Hz}}}$ [Fri93].

Mechanical resonances of the spacer and environmental temperature fluctuations result in length fluctuations due to the thermal expansion of the spacer. While the first effect produces peaks in the noise spectrum, temperature fluctuations appear over long time scales. The cavity tank is passively shielded by foam and a heater attached to the tank allows active temperature control as described in the next Section.

Temperature control of reference cavity

Tidal gravity fluctuation by the moon and the sun vary the 4 km long LIGO arms by 100-200µm, that needs to be compensated by a long range actuator [Adh14]. The reference cavity acts as the ultimate DC frequency reference for LIGO and the thermal expansion of the fused silica reference cavity spacer is 110 nm/K. The requirement for the thermal stability of the reference cavity is set to be less than 5 mK temperature variation per day, which is a factor of ten less than the equivalent frequency shift due to the tides. Thus no additional load is put on the long range actuators.

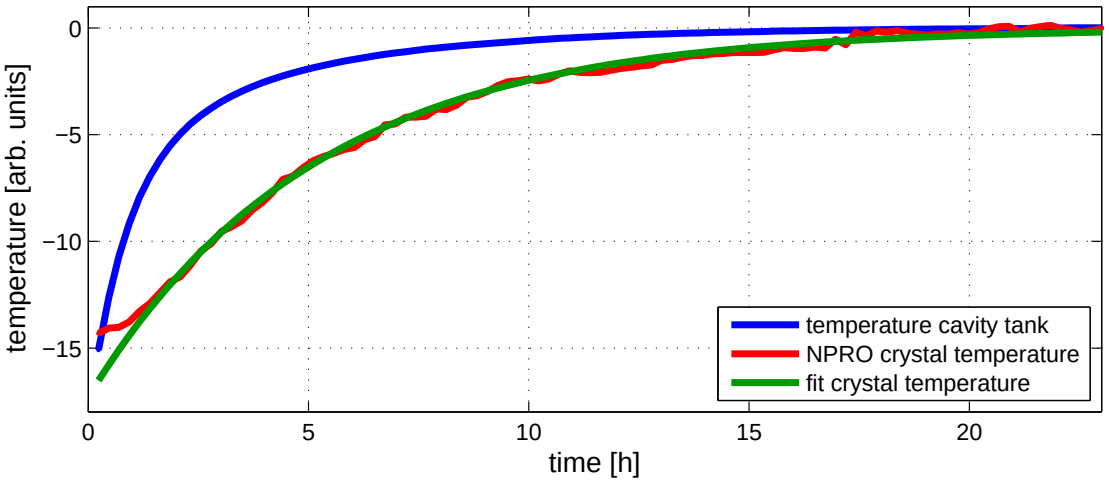

Figure 5.5: Measurement of the NPRO temperature response to a step in the reference cavity temperature. The time constant of 5.12 h is calculated by the fit.

Although it might be possible to passively stabilize the reference cavity temperature with proper thermal isolation, a local active control loop is used, which can also compensate temperature drifts to increasing ambient temperatures in the laser room when personnel are present and the FFUs are enabled. It consists of four in-loop and one out-of-loop temperature sensors that are mounted to the cavity tank. The signal of the in-loop sensors is summed and acquired by the CDS. It is digitally filtered and fed to the heater that is driven by a high current OP. The resistance of the heater is 13 Ω and it can produce up to 34 W.

The reference cavity is kept at an offset temperature of about 39 degree celsius, which is at about the middle of the heater range. It was possible to achieve an in-loop stability of 2 mK temperature variation per day and an out-of-loop stability of 40 mK temperature variation per day, while the ambient temperature was varying by 200 mK. Since the sensors are mounted to the tank there is a 34 µHz pole in the transfer function, which is caused by the time it takes to heat up the stainless steel tank. Thus the digital part of the loop consists of a proportional gain.

Due to temperature gradients in the reference cavity tank it is questionable if the accuracy of the control loop improves by summing the four in-loop sensors that are about 20 cm apart from each other. Furthermore, the temperature of the heater is proportional to the supplied power. An actuation of the heater voltage could require an square root OP in a faster loop as there is a quadratic relation between the voltage and the power.

Finally, there is another delay for the spacer to adopt the tank temperature.

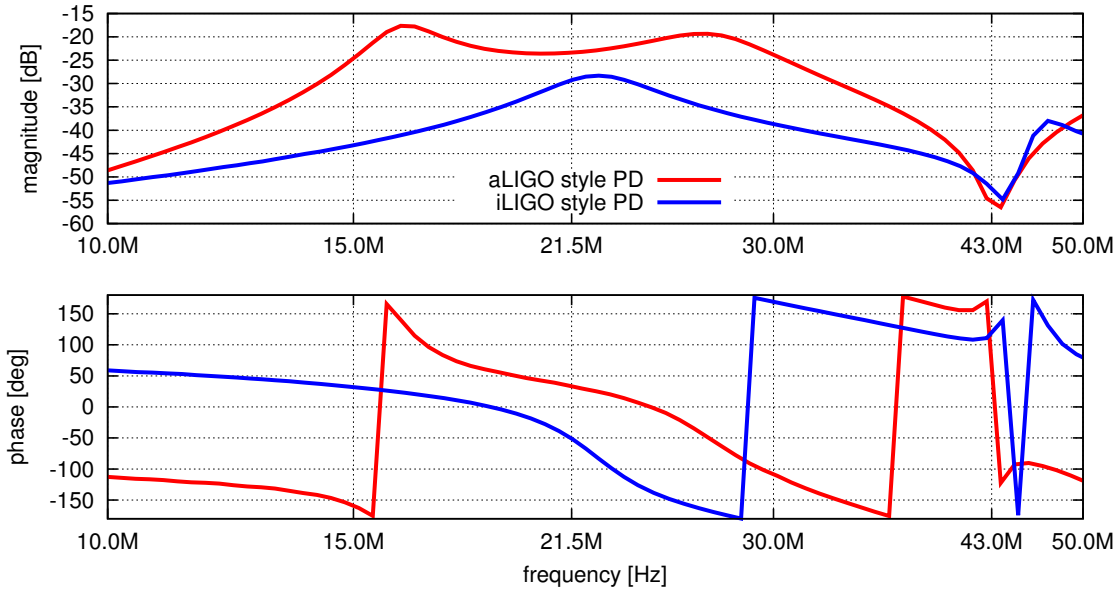

Figure 5.6: Transfer function of iLIGO and aLIGO RF PDs. The resonance peak of the aLIGO style PD is much broader. As the test setups were different the absolute level of the amplitude response cannot be compared.

To measure the time constant a temperature step is put to the heater and the NPRO crystal temperature was sampled while the frequency stabilization was locked (Fig. 5.5). A time constant of 5.12 h is calculated by a fit of the NPRO crystal temperature.

RF photodiode

To read out the RF signal for the PDH locking a PD was built with a passive resonance circuit at 21.5 MHz in order to achieve a better shot noise limited sensitivity. It is similar to other PDs utilized in several loops throughout the aLIGO detector. The amplifier design is similar to the GEO design [Gro07] and it is possible to simultaneously read out signals at two different RF frequencies. The aLIGO design employs a 2 mm Excelitas C30642 PD [AAF11] and achieves shot noise limited input sensitivity is 1.8 mA.

A transfer function of the PD was measured (Fig. 5.6) and compared to the resonant PD used in iLIGO[1]. For the characterization different test setups were used, such that the amplitude response calibration is not the same for the two measurements. The main difference between the two PDs is the width of the res-

[1]The readout amplifier design is described in [Gro07].

onance peak, which is much narrower for the iLIGO PD. In iLIGO the PD pole frequency was at 700 kHz[2]. A notch filter at twice the modulation frequency is filtering second harmonic effects.

5.2.2 Controller

In Figure 5.4 the TTFSS electronics is shown on the bottom picture. It consists of a common path (FSS_{COM}), which contains a mixer, an elliptical filter at 21.5 MHz and a 40 dB variable gain amplifier (VGA). The output of the common path is split into a path going to the NPRO PZT (FSS_{PZT}) and one that provides the control signal for the EOM (FSS_{EOM}). The PZT path has another 40 dB VGA, several amplification stages and a notch. In the EOM path there are amplification stages with high bandwidth, a notch filter, and a high voltage OP to provide a high EOM actuation range. The high voltage OP in parallel with another gain stage employing a very fast OP that is supposed to provide gain above 500 kHz where the high voltage OP is GBP limited.

The TTFSS sets the cross over frequency between the PZT and the EOM feedback, which can be changed adjusting the VGA in the PZT path. While the EOM path is AC coupled the PZT path provides gain at DC. However, it is supported by a slow digital control loop with a feedback to the NPRO crystal temperature (see upper picture in Fig. 5.4) that keeps the PZT at the middle of its dynamic range.

To adapt the TTFSS for aLIGO several changes were implemented in the TTFSS. Since the PMC pole frequency of the aLIGO PMC of 578 kHz is within the frequency stabilization control bandwidth, an electronic pole compensation with a zero at 372 kHz and a pole at 8.4 MHz was inserted. The zero was chosen to be below the PMC pole to gain some phase margin at the servo UGF. Furthermore, proportional gain was added in the PZT stage as the PZT actuation coefficient is lower for the aLIGO NPRO (Sec. 5.2.3) and the corner frequency of the AC coupling high pass in the EOM path was raised as saturation effects in the EOM path were observed in the past. Due to mechanical restrictions on the circuit board the PMC pole compensation only affects the high voltage amplifier stage and not the parallel circuit which was providing loop gain at very high frequencies. Consequently, the parallel path was deactivated as it did not improve the loop gain any more and was instead adding noise.

At the LIGO observatories the iLIGO TTFSS [ASM05] was modified and used. For the experiments at the Reference System new style TTFSS [SS09] was used,

[2]The pole of the iLIGO PD shown in Figure 5.6 is 1.35 MHz and was raised to temporarily use it in the aLIGO setup.

which had an additional input to directly measure the PZT path transfer function. Moreover, this design employs a different high voltage OP.

5.2.3 Actuator

The split feedback employs three actuators. Two of which, the NPRO crystal temperature controller and the NPRO PZT were characterized in [KW08]. The NPRO temperature actuation coefficient for the aLIGO NPROs is 2.8 ± 0.3 GHz/K with a pole at 163 ± 41 mHz. For the PZT the first PZT resonance is at 200 kHz and the actuation coefficient is 1.48 ± 0.25 MHz/V. This actuation coefficient is nearly a factor of three smaller than it used to be for the iLIGO NPRO PZT [AMS97].

While a NPRO crystal temperature change and an actuation of the PZT result in a proportional change of laser frequency, the EOM (New Focus 4004) actuates the phase of the laser light. However, as shown in Equations (3.12) and (3.14) a phase modulation is equivalent to a frequency modulation with Fourier frequency dependent modulation index.

The transfer function of the EOM shown in Figure 5.7 was measured from the EOM input to the PMC error point in LPM and HPM. Moreover, in LPM the transfer function of the EOM was also measured to the frequency stabilization error point, while the frequency stabilization was locked with low bandwidth without using the EOM as actuator. From the slope of the amplitude response an EOM modulation depth of 0.018 rad/V was calculated, which agrees with the values from iLIGO [AMS97] and the vendors specifications. There are EOM resonances at 780 kHz and a stronger one at 1.7 MHz.

For the measurement to the PMC error point the PMC pole and a complex pole (f=4.79 MHz, Q=0.486) that is implemented after the mixer to filter noise at the modulation frequency were subtracted in post processing. In case of the measurement to the reference cavity error point effects from the PMC and the reference cavity pole were subtracted. The transfer function of the non-resonant, high bandwidth PMC locking PD was measured in [Põl09] and adds less than 10 degrees phase lag at 5 MHz.

The difference of the two transfer functions measured HPM and LPM shows the influences of the HPO on the actuator transfer function. At a Fourier frequency of 1 MHz a phase lag of approximately 40 degree is added by the HPO and above 1 MHz there are additional features in the amplitude response as well.

The transfer function from the EOM input to the reference cavity error point contains effects from the RF PD and the elliptical filter that suppresses the unwanted signal at the modulation frequency downstream of the mixer. Both

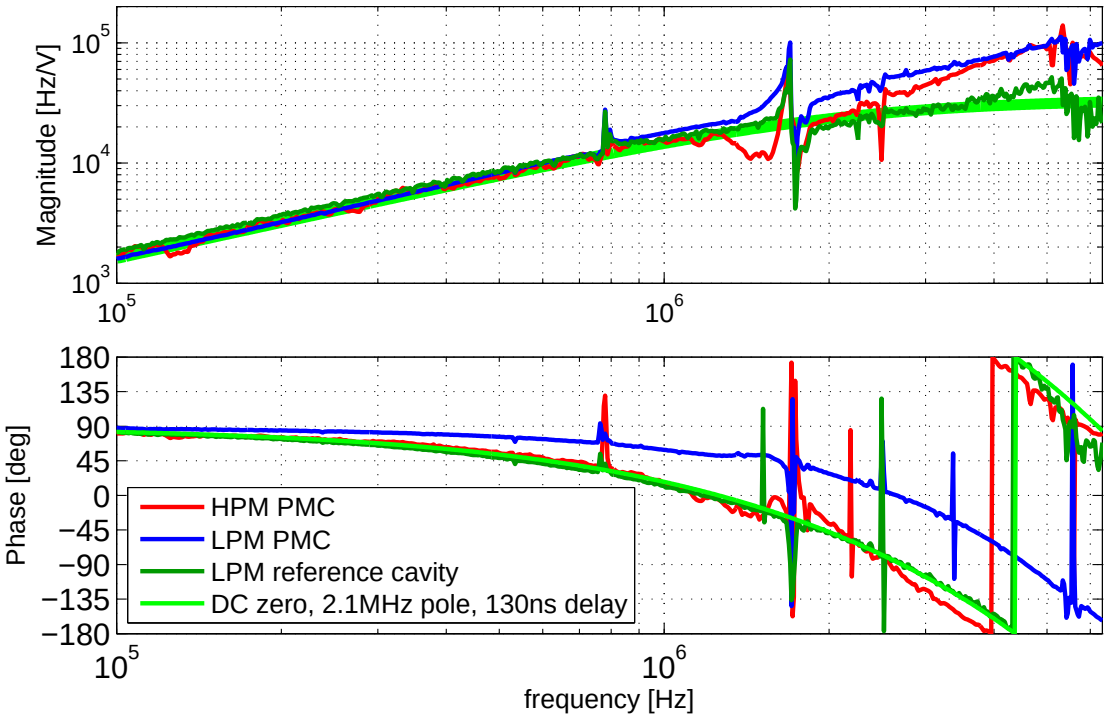

Figure 5.7: Transfer function measurement from the EOM in LPM and HPM to the PMC error point (blue and red trace). The PMC pole was subtracted in post processing. In HPM effects from the HPO contribute to the phase. A measurement from the EOM to the reference cavity error point (green trace) shows that the resonant RF PD and the elliptical filter in the TTFSS effect the actuator transfer function. This is modeled with a zero at DC, a pole at 2.1 MHz and a time delay of 130 ns. The model is accurate up to 3 MHz. There are EOM resonances at 780 kHz and 1.7 MHz.

show up at high Fourier frequencies and can be modeled with an additional pole at 2.1 MHz and a time delay of 130 ns. This model is accurate up to 3 MHz and is used for the control loop simulations that are described in the next Section.

5.2.4 Control loop simulation

A simulation of the frequency stabilization control loop is performed for the LPM and the loop transfer function along with the transfer functions of the EOM path and the PZT path are shown in Figure 5.8. This simulation does not contain any notch filters that can be implemented in the TTFSS. Furthermore

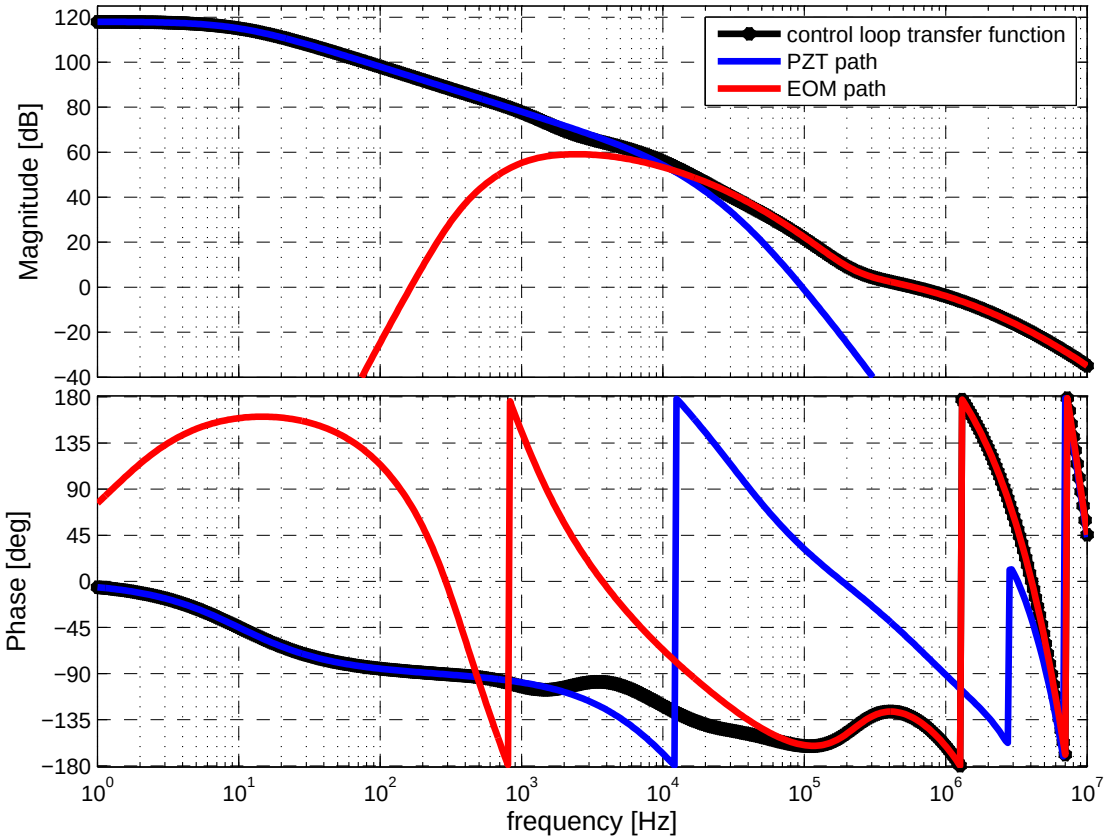

Figure 5.8: Simulation of the frequency stabilization control loop in LPM. The cross over frequency of the EOM and the PZT path is around 10 kHz. At 5 Hz the gain of the control loop is 120 dB.

the model derived for the EOM path is applied (Sec. 5.2.3), which does not contain the EOM resonances.

At 5 Hz the open loop gain is 120 dB and the cross over between the feedback paths via the PZT and via the EOM is approximately at 10 kHz.

The speed of the high voltage OP limits the bandwidth of the control loop. In the initial design this limitation was mitigated by a parallel path employing a faster OP (Sec. 5.2.2). As this path has a similar effect than the daughter board used for the PMC pole compensation [ZRO02], it can be used instead of the PMC pole compensation in order to achieve the current control loop performance.

However, for an optimization of the control loop the PMC pole compensation has to be implemented in front of the split between the high voltage OP and the fast parallel path. Consequently, such a loop configuration compensates the

PMC pole and provides gain at high frequencies due to the fast path in parallel to the high voltage OP and allows a control loop operation with a UGF above 1 MHz.

5.3 Performance of the frequency stabilization

For the evaluation of the performance of the frequency stabilization loop, loop transfer functions shown in Figure 5.9 were measured. The one taken at LLO has more loop gain at 10 kHz, which is probably due to a higher cross over frequency between the EOM and the PZT path. A cross over frequency of 10.5 kHz and a phase margin of 90 degree was measured for the Reference System in both HPM and LPM. The loop had a UGF of 600 kHz in LPM with a phase margin of 35 degree for the Reference System and 55 degree at LLO. The phase difference is due to a slightly different loop shape at high frequencies. These measurements are in accordance with the simulations (Sec. 5.2.4). Due to an additional phase lag from the HPO that was observed in the actuator transfer function measurement (Fig. 5.7) a transfer function with a UGF of 380 kHz and 32.5 degree phase margin was achieved in HPM.

An EOM resonance at 780 kHz prohibits a higher UGF in HPM since the phase already dropped below 180 degree at this frequency. This resonance is not present in the LLO measurement, although the same type of EOM is used. The other EOM resonance at 1.7 MHz is suppressed by a notch filter. Furthermore, as the PZT path transfer function measurement revealed a PZT resonance at 250 kHz an additional notch was inserted in the PZT path. This notch is not installed at LLO causing a broad resonance at 250 kHz in the loop transfer function.

The lock acquisition for the frequency stabilization is automated. First the NPRO temperature is ramped, while a 10 Hz modulation is applied to the PZT. This is necessary as the PZT does not have enough dynamic range to cover a full FSR. If the fundamental mode is found the feedback loop is closed and the variable gain in the TTFSS common path is slowly increased to the target setting. A reduced gain avoids saturation in the amplifiers when the lock is acquired.

In lock the frequency noise can be obtained by a measurement of the TTFSS error signal (Fig. 5.10). As an in-loop measurement it is, however only a best case estimate of the stabilized frequency noise because it just shows by how much the unstabilized laser frequency is suppressed by the loop gain. Other limitations like electronics noise and photon shot noise cannot be estimated from this measurement. Moreover, the frequency noise is only as good as the inherent noise of the reference cavity.

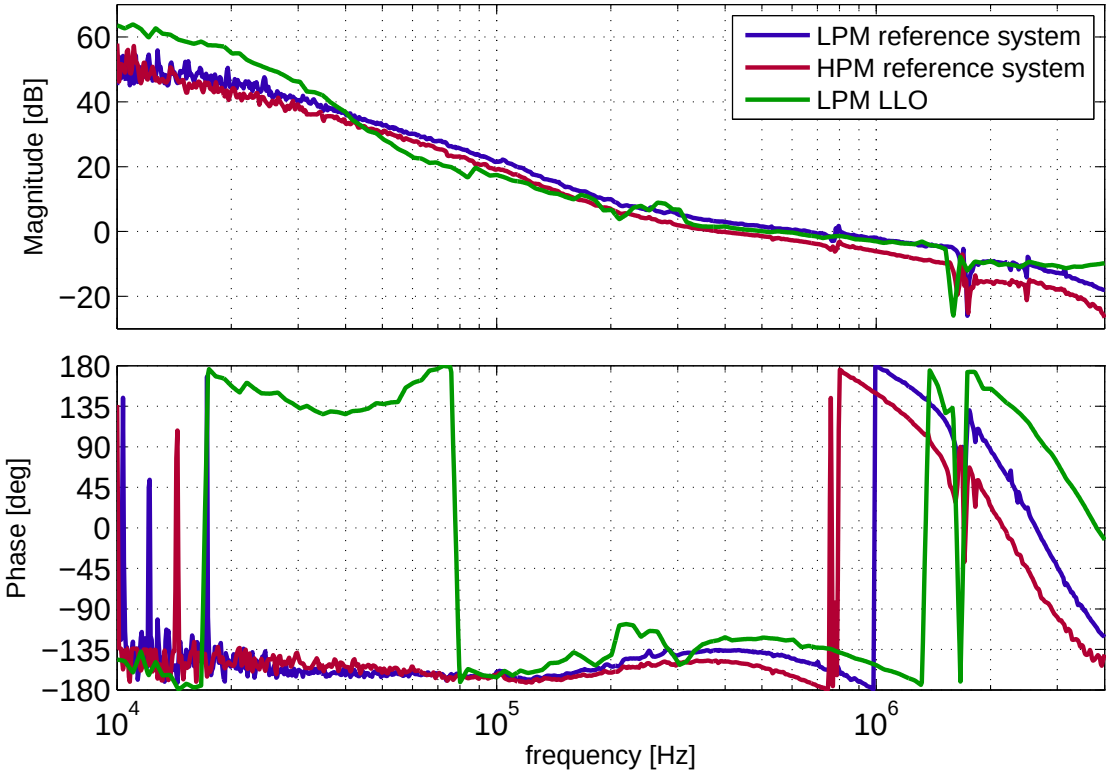

Figure 5.9: Frequency stabilization loop transfer function measured in LPM (blue) and HPM (red) at the Reference System and a LPM measurement from LLO (green). Additional phase lag is introduced by the HPO in HPM. The LLO measurement has a higher cross over frequency which leads to a higher gain at 10 kHz compared to the measurement at the Reference System. The EOM resonances are stronger at the Reference System. In LPM a UGF of 600 kHz with a phase margin of 35 degree (55 degree at LLO) is achieved whereas in HPM the UGF is 380 kHz with 32.5 degree of phase margin.

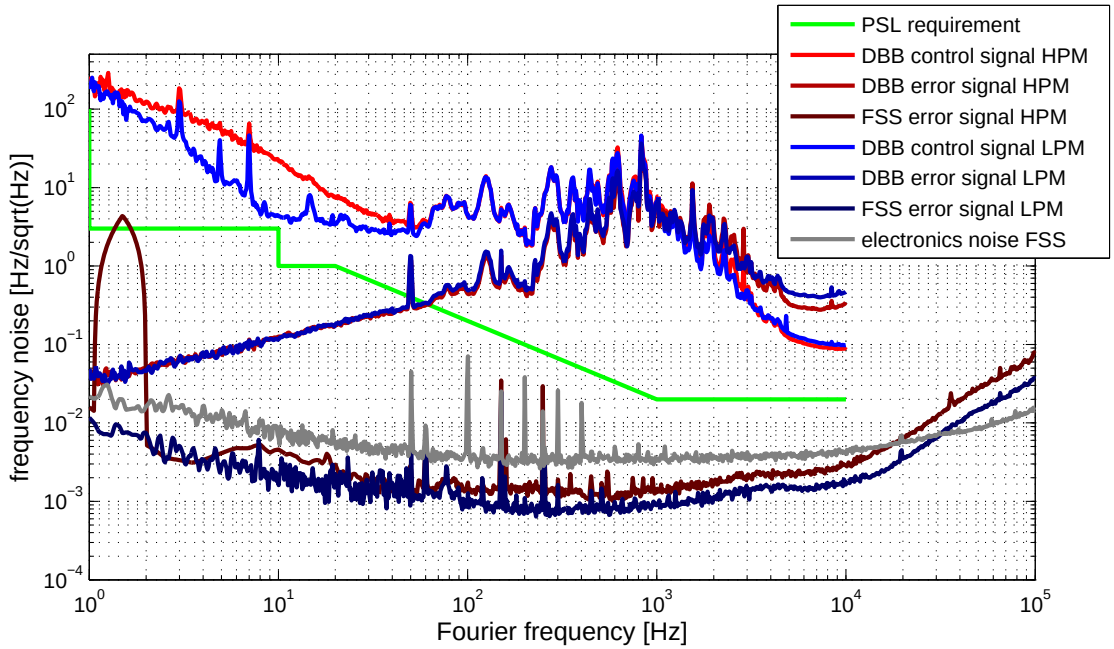

Figure 5.10: Frequency noise measurement at the Reference System. The DBB control and error signal show the length noise of the DBB resonator in LPM and HPM, which is an upper limit for the frequency noise of the stabilized laser. Excess noise is present in HPM at Fourier frequencies less than 40 Hz. In contrast the frequency stabilization error signal is a best estimate for the frequency stability. The measurements were done in LPM and HPM and the HPM measurement contains a peak at 3 Hz of unknown origin.

The origin of the 3 Hz peak in the HPM measurement could not be determined. Electronics noise at the error point was obtained while there was no light on the PD and is shown in Fig. 5.10. Since the power directed towards the reference cavity was not always at the same level the shot noise limited sensitivity of $120\,\mathrm{mHz}/\sqrt{\mathrm{Hz}}$ is calculated for a worst case with a carrier power of 5 mW[3][Bla01]. Although the shot noise limited sensitivity increases above the reference cavity pole frequency it is still below the noise level observed at the error point for all Fourier frequencies.

As the RF PDs shot noise limited input sensitivity is 1.8 mA, more than 2.5 mW sideband power is required to exceed the electronics noise. This corresponds to

[3]This power level is required in transmission of the reference cavity for the LIGO arm length stabilization system. Additional shot noise due to higher order spatial modes is neglected in this assumption.

a modulation depth of 0.5 rad assuming a total power level of 20 mW in the beam directed towards the reference cavity.

While the frequency stabilization error point measurement sets a lower limit for the stabilized laser frequency noise, an upper limit can be obtained by the frequency noise measured with the DBB (Fig. 5.10). The DBB PDH control loop has a UGF of 700 Hz, such that the measured frequency noise is observed in the control signal below and in the error signal above 700 Hz. As it is confirmed in the frequency noise measurement with the IMC (Sec. 5.4.1) the measured noise level represents the length noise of the DBB resonator. However, the DBB frequency noise is close to the reference cavity length noise at 5 Hz [CSA+13], which is dominated by vertical seismic motion. Compared with the PMC (Fig. 3.11) the DBB resonator is a much better frequency reference. Furthermore, there is an increased noise level in HPM below 40 Hz which might be due to the presence of scattered light.

Noise couplings

There are a number of noise sources, apart from the inherent reference cavity noise, that can influence the performance of the frequency stabilization. This Section will discuss the coupling mechanisms and point out the benefits of using an AOM as an actuator for the power stabilization and the PMC as part of the frequency stabilization loop with respect to cross couplings.

Since an AOM does not effect the phase of the beam in zeroth order, a power actuation does not have an effect on the frequency stabilization. In other cases when the current to the laser pump diodes is actuated a frequency modulation is imposed on the laser beam as well [WBD+00]. However, amplitude modulations have an effect on the frequency stability as they can impose offsets on the frequency stabilization error signal. In the ideal case when the reference cavity is locked exactly on resonance amplitude modulations appear as second order effects [Fri93]. If there is a small electronics offset in the frequency stabilization control loop or noise imposed by residual amplitude modulation (RAM) produced by the EOM [WGB85, KIK+14], amplitude modulation coupling will appear as first order effect. Fluctuations of the RAM at the modulation sideband frequency results in a similar coupling effect. Since the sensing for the power stabilization is done downstream of the PMC the power noise is suppressed very well in the beam directed towards the reference cavity. However, variations of the RF power applied to the AOM, that is used as frequency actuator, could add power noise to the beam.

Phase noise added by the PMC is suppressed by the frequency stabilization, as the PMC is part of the frequency stabilization control loop (Fig. 5.4). Since the PMC pole is approximately at the UGF of the frequency stabilization control

loop, it has a negligible effect on the shot noise limited sensitivity of the control loop. A study showing the advantages of having the PMC within the frequency stabilization control loop was conducted at Caltech [Kaw03].

Furthermore, phase fluctuations caused by vibrations of the periscope used to couple the laser beam into the reference cavity and pointing noise in conjunction with static misalignments [Fri93] can cause excess frequency noise.

5.4 Input-Modecleaner

In the previous measurements with the DBB (Sec. 5.3) the frequency noise measurement accuracy was limited by inherent length fluctuations of the DBB resonator. The Input-Modecleaner serves as a very good frequency reference for frequencies above 5 Hz and a frequency noise measurement utilizing the IMC is obtained in Section 5.4.1.

The IMC is a resonator in a triangular configuration inside the LIGO vacuum system. Its three mirrors have a diameter of 150 mm, a thickness of 75 mm and a weight of 2.9 kg. They are individually suspended by a three stage pendulum, which is mounted to a seismically isolated optical table. Two of the mirrors (IMC_1 and IMC_3) are flat, have a power transmission of 0.006 and are located adjacent to each other, such that the beam is hitting them at an angle of 44.6 degree (Fig. 5.4). The third mirror has a ROC of 27.24 m, is high reflective and approximately 16 m apart from the other two. Consequently, the optical round trip path length is 32.9 m. The Gaussian beam waist size is 2.12 mm and it is located between the flat mirrors [MMT+13].

Frequency noise is passively suppressed above the pole frequency of 8.72 kHz. The FSR is 9.1 MHz and the IMC has a finesse of 522. Moreover, there is active frequency noise suppression, which is described in the next Section. The IMC acts as spatial mode filter and filters RF modulation sidebands. In regular operation the laser beam traveling towards the IMC is vertically polarized with respect to the optical table[4]. The IMC acts as polarization filter as a horizontally polarized beam experiences an extra phase shift of π per round trip due to an odd number of reflections. Furthermore the IMC provides a pointing noise filtering factor of 250 [Mül09] and its eigenmode serves as stable beam reference for the IFO.

[4]For alignment purposes the polarization of the input beam is rotated in order to reduce the finesse.

Control loop

Figure 5.4 shows the control loop for the IMC. Similarly to the locking of the PMC the IMC is kept resonant with the impinging laser field by PDH locking technique. Phase modulation sidebands for the locking are imprinted by an EOM downstream of the PMC at 24.08 MHz. The RF PD has the same style as the one used for the sensing of reference cavity error signal (Sec. 5.2.1). In contrast to the PMC, the IMC serves as frequency reference as well. Therefore the controller incorporates a common gain stage (IMC_{COM}) followed by a split of the signal fed back to the IMC length actuator (IMC_L) and to the laser frequency (IMC_F).

As the IMC length noise is dominated at low Fourier frequencies by seismic noise that drives the suspension resonances, which are below 3 Hz, the rigid reference cavity is a better frequency reference. Above the pendulum resonances of the IMC suspensions, seismic noise is strongly suppressed and the IMC is the better frequency reference, respectively. Theoretical models show that the ideal cross over frequency is at 5 Hz. However, hierarchical control of the three length actuators in conjunction with the pendulum resonances limits the cross over frequency to 15 Hz [Mue14]. The best cross over frequency can be experimentally determined by a measurement of the frequency noise with the arm cavities, which were not commissioned during the IMC commissioning.

The actuator for the frequency actuation consists of a low noise VCO and an AOM (Isomet 1205C). The AOM is operated in a double pass configuration to minimize beam pointing of the diffracted beam. Hence, it is placed in the focus of a curved mirror with 300 mm ROC (Fig. 5.4). A small beam waist size inside the AOM of 155 µm reduces the interaction time of the acoustical wave with the laser beam and thus the time delay in the IMC feedback control loop. The VCO output frequency is 80 MHz and can be adjusted by ± 1 MHz. Hence, the frequency of the laser beam is shifted by 160 ± 2 MHz. The VCO design was improved compared to the iLIGO design because VCO phase noise was dominating the frequency noise of the beam transmitted by the IMC at high Fourier frequencies [Adh04]. For aLIGO a lower phase noise is achieved by a reduction of the dynamic range of the VCO [AS09].

The phase lag imposed by the AOM was measured to be 19 degree at 50 kHz and 42 degree at 100 kHz. This allows the operation of the IMC control loop with a UGF up to 100 kHz. The phase noise equivalent frequency noise of the VCO is flat and less than $1\,\mathrm{mHz}/\sqrt{\mathrm{Hz}}$ in a frequency band between 40 Hz and 30 kHz [AS09], which contributes twice to the frequency noise of the laser beam due to the AOM double pass.

A variable gain stage in the common path of the IMC controller allows a lower gain during lock acquisition in order to avoid saturation effects. At 1 kHz the

control loop provides a gain of 50 dB, while it was robustly locked with a UGF of 40 kHz and a phase margin of 67.5 degree.

5.4.1 Frequency noise measurement

During the IMC commissioning, the IMC is operated at different input power levels. Most of the time the input power was 3 W, but it was increased to a maximum power 120 W for a short high power test described in Section 5.4.2. For the frequency noise measurement with the IMC the FFUs and air conditioning in the laser room were turned off. The measured signal is the control signal of the IMC acquired at a monitor port of the VCO, which represents the frequency noise of the pre-stabilized beam at the input of the IMC between Fourier frequencies of 15 Hz up to the UGF of the IMC feedback control loop[5]. A subsequent pole-zero combination in the VCO path, a 6 dB amplification at the VCO monitor port, the voltage to frequency conversion coefficient of 246 kHz/V at DC and a factor of two due to the AOM double pass have to be considered for the calibration of the signal.

Figure 5.11 shows a history of the frequency noise at the input of the IMC over the course of the IMC commissioning. The IMC was operated at input power levels of 1 W and 3 W. Between September of 2012 and January of 2013 the VCO was changed from the iLIGO version to the low-noise aLIGO version, which is described in the previous Section. The power stabilization was operated in different conditions, that were unfortunately not recorded at the time of the frequency noise measurement. The frequency stabilization loop for the reference cavity provided 19 dB gain at 100 kHz and 60 dB at 10 kHz. In between the frequency noise measurements the alignment of the reference cavity and the alignment of the IMC was changed several times. Between January of 2013 and August of 2013 the water distribution of the HPO was modified as described in the next Section. Moreover, a passive lowpass filter was added to the electronics of the PZT, which is mounted to the top of the periscope, that is sitting on the laser table and used to direct the laser beam towards the IMC.

Some noise sources are not displayed in Figure 5.11 as their influence to the total noise is negligible. Among them is the photon shot noise, which is below 200 $\mu Hz/\sqrt{Hz}$ and increasing above the IMC pole. The phase noise equivalent frequency noise of the VCO is at approximately 200 $\mu Hz/\sqrt{Hz}$ and other effects caused by technical RPN are at least two orders of magnitude below the measured frequency noise level.

As for most of the other measurements the frequency noise in HPM is higher

[5]For the January 2013 measurements the UGF was 20 kHz and for the September 2013 measurement 30 kHz.

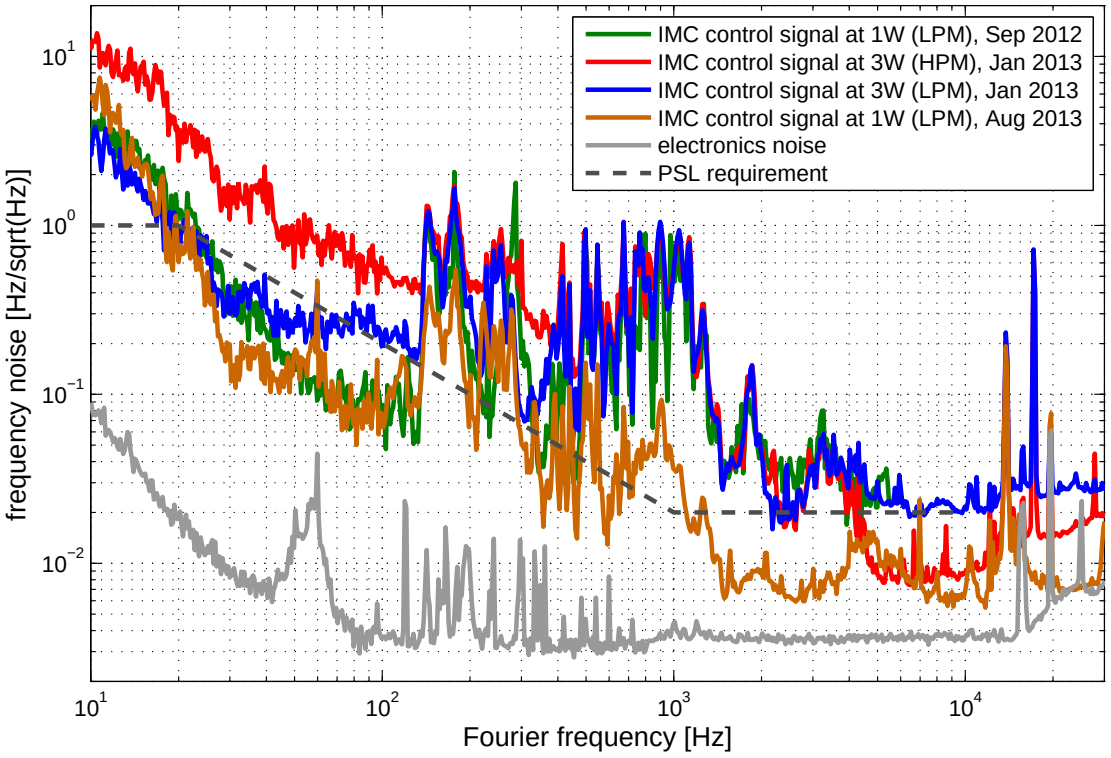

Figure 5.11: Measurement of the IMC control signal fed back to the VCO representing the frequency noise of the beam entering the IMC in HPM (red trace) and LPM (green, blue and orange traces). Three measurements show the frequency noise over one year of IMC commissioning. At low frequencies an increase in the noise level in HPM is observed, while the dominating noise source is unknown. The mid frequency band is dominated by vibrations on the laser injection bench. Fourier frequencies above 5 kHz could be limited by injection bench fluctuations as well or by power to frequency noise coupling. Electronics noise is not limiting the frequency noise performance below 20 kHz.

at Fourier frequencies up to 100 Hz. The dominating noise source for all measurements up to 80 Hz is unknown. Seismic noise coupling to the reference cavity is at a level of 0.1 Hz/$\sqrt{\text{Hz}}$ at 15 Hz according to a measurement taken at Caltech in a different environment [CSA+13]. Above 15 Hz the coupling is decreasing rapidly due to the influence of the reference cavity suspension. The frequency noise between 80 Hz and 2 kHz is dominated by vibrations of the periscope on the laser table and optic mounts [Mue14]. This was measured by a frequency noise projection of an accelerometer signal acquired at the top of the periscope. The noise improved after the modification of the laser water distribution. Thus the best noise curve obtained in August of 2013 touches the thermal noise limit described in Equation (5.1) at 1.5 kHz. The trace measured in September of 2012 ends at 5 kHz as it was acquired digitally at a sampling rate of 16 kHz.

Since the accelerometer data were also sampled digitally it cannot be estimated if noise above 5 kHz is correlated to injection bench vibrations as well. The difference between the measurements at Fourier frequencies above 4 kHz and the limiting noise source for the measurement taken in August 2013 might be caused by power noise to frequency noise cross coupling. To investigate this possibility a transfer function from the out-of-loop power stabilization PD to the NPRO PZT control signal was measured at the Reference System and at LLO. The source was injected at the error point of the power stabilization loop. The measurements were dominated by noise up to 10 kHz, which is already the cross over frequency between the PZT and the EOM path and so the coupling constant obtained is setting an upper limit for the coupling. At 10 kHz a coupling coefficient of 10^4 Hz/RIN was measured at LLO and 10^5 Hz/RIN at the Reference System. Another transfer function was measured from the power stabilization out-of-loop PD to the frequency stabilization error point. The coupling coefficient at the error point is 0.29 Hz/RIN at 10 kHz. This coefficient has to be multiplied by the loop gain of the frequency stabilization control loop. Assuming a gain of 60 dB the coupling coefficient is 290 Hz/RIN. A power noise of $2 \cdot 10^{-7}/\sqrt{\text{Hz}}$ as derived from Figure 3.3 yields a frequency noise as high as 2 mHz/$\sqrt{\text{Hz}}$. Due to the coupling mechanism of amplitude to frequency noise (Sec. 5.2.1) the coupling coefficient can change depending on the control loop offset. Enabling the power stabilization decreases the power noise at 10 kHz by 5 dB to 20 dB. As the status and the gain of the power stabilization loop was not recorded further investigation are required to determine the limiting noise sources at high frequencies. Moreover, the strong peak at 14 kHz could be caused by a resonance of the reference cavity spacer. A measurement of the electronics noise shows that it is not limiting the frequency noise performance below 20 kHz.

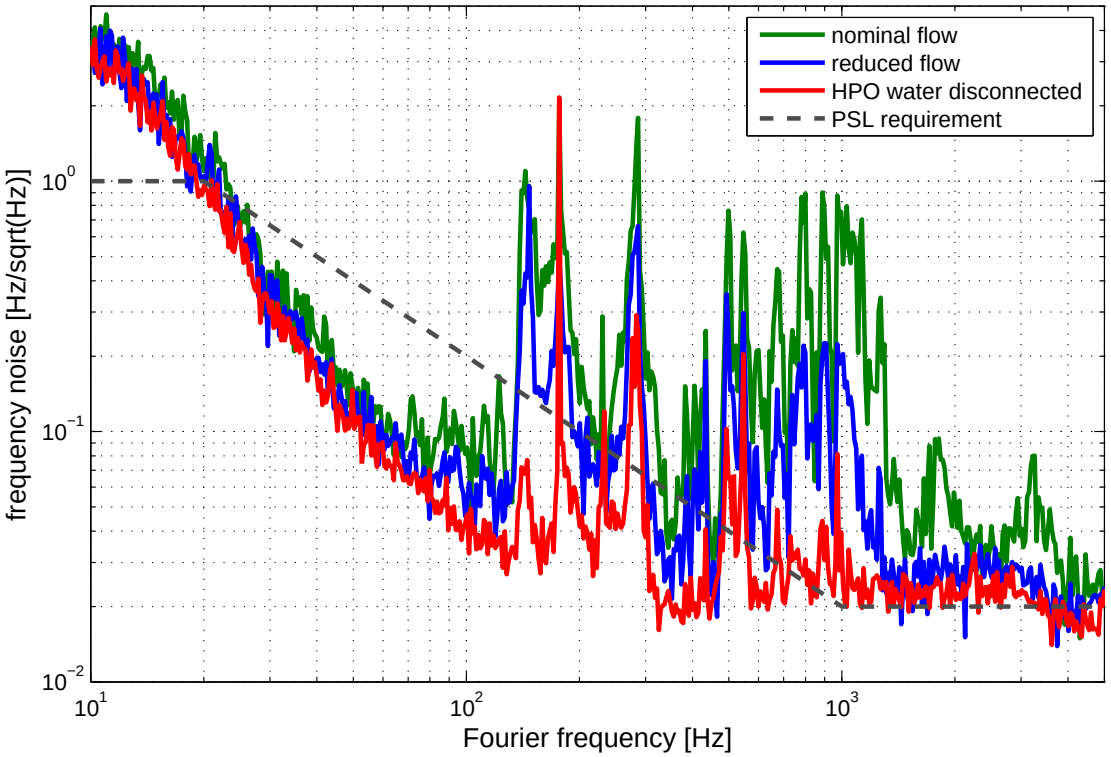

Figure 5.12: Measurement of the frequency noise of the beam entering the IMC in LPM with different configurations of the HPO cooling water distribution. The first measurement was obtained with the nominal flow rate (green trace), a reduced flow rate (blue trace) and with the water lines disconnected from the HPO. A noise reduction is achieved between 80 Hz and 5 kHz.

Excess noise due to vibration of cooling water

High flow rates are required in order to provide sufficient cooling of the HPO laser crystals (Sec. 3.1.2). It was found that the connectors used to supply the cooling water to the HPO create a turbulent flow at the HPO water interface. This is leading to vibrations that propagate throughout the laser table and ring up resonances of mechanical components on the table.

To evaluate the influence on the coupling to the frequency noise of the laser beam entering the IMC the water flow was reduced and afterwards the water lines to the HPO were completely disconnected. Figure 5.12 depicts the three scenarios. An obvious reduction in the noise coupling is observed by lowering the flow rate. In case that the water lines are disconnected from the HPO only a few resonances are left in the frequency noise spectrum.

However, to operate the HPO the nominal flow rate is required to avoid damages caused by heat. Therefore the water interface was changed such that the hoses are directly connected to the HPO interface. Thereby the small aperture of the old connectors were removed, which leads to a more laminar flow through the interface. Nevertheless, turbulent water flow remains in the cooling chambers for the laser crystals.

5.4.2 High power Input-Modecleaner test

To demonstrate that the IMC is capable of handling high input powers as they are planned for the operation of aLIGO, the laser power of the input beam was increased up to 120 W[6]. The laser power was increased in steps of 30 W and kept at the final power level of 120 W, which was the highest available input beam power at that time, for more than one hour. The study of thermal effects that can arise due to absorption in the IMC optics and the robustness of the nested control loop were two of the main aspects of the high power IMC test.

One possibility to characterize absorptions is by measuring the pole frequency. As the round trip IMC length does not change this is a direct measurement of the finesse and consequently the losses inside the cavity (Eq. (3.17)). The specification for absorptions of a IMC mirror is 1 ppm and the loss due to scattering should stay below 15 ppm [MMT+13]. An increase of the total loss by 10 ppm shifts the cavity pole frequency by 30 Hz.

A transfer function is measured from a high bandwidth PD upstream of the IMC to another PD downstream, while a swept sine is applied to the AOM that serves as power stabilization actuator. A single pole lowpass is fitted to the data to determine the cavity pole. Figure 5.13 shows the results of the fitted pole frequencies at different input power levels. The standard deviation is calculated for the mean value. For the measurements of power levels from 3 W to 120 W the mean value of the pole frequency varies by 131 Hz but the data does not show an explicit trend. Hence, it is obvious that this method cannot be utilized to detect absorption changes on a ppm level. However, it can be used to check for clipping in the IMC beam path, which increase the loss by several hundred ppm. Due to apertures that are supposed to block scattered light, beam clipping is a concern when the IMC alignment is changed. To determine absorptions of the mirrors tracking of the Gouy phase as described in Section 3.2.4 or a measurement of mechanical internal resonance frequencies of the optics is more accurate.

[6] After this test it was found that contaminations on the IMC optics in conjunction with high power could cause permanent damage and the IMC was only operated at low power.

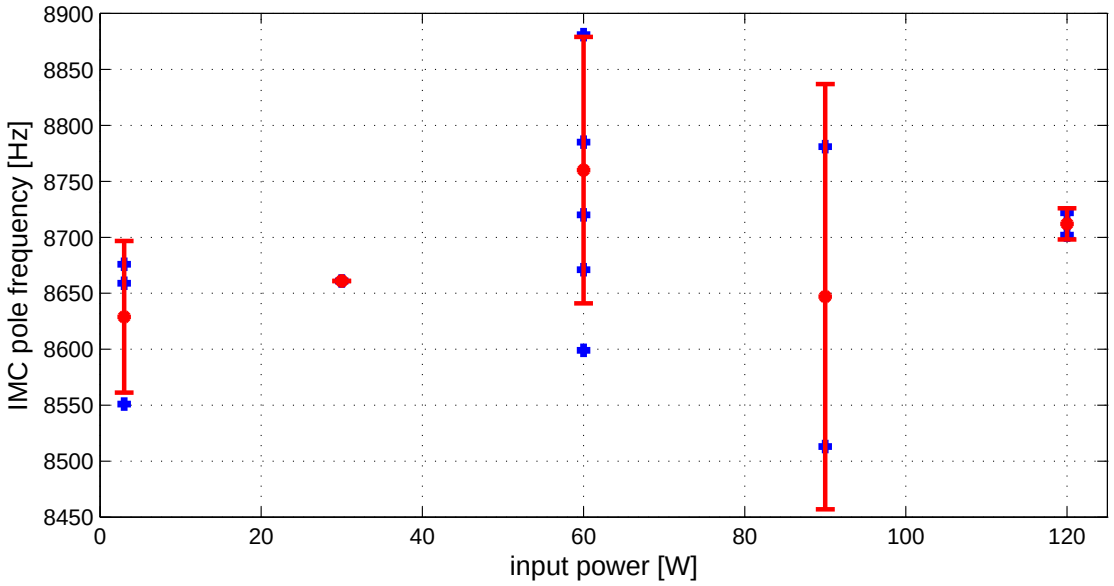

Figure 5.13: Pole frequency measurement of IMC pole at input power levels up to 120 W. The pole frequency is obtained by a transfer function measurement of power fluctuation suppression upstream and downstream of the IMC. The fitted pole frequencies, the mean values and their standard deviation is plotted. This method cannot detect mirror absorption changes on a ppm level. It can be used as a fast detection of losses due to clipping in the IMC beam path.

5.5 Prospects

Future improvements of the frequency stabilization with respect to the control loops considered in this thesis can be split into two categories. The first is the improvement of the robustness, gain and bandwidth of the frequency stabilization control loop. The other is the characterization and mitigation of noise sources unrelated to the loop gain limitations of the frequency stabilization.

To improve the bandwidth of the control loop the EOM has to be replaced by an EOM whose resonances are at higher frequencies. In order to avoid phase lag from the HPO the EOM can be located in the high power beam downstream of the HPO [OMM10]. Furthermore, if the electronics path parallel to the high voltage OP is reactivated more phase margin is provided above 500 kHz. For now loop gain is not a major concern as the out-of-loop frequency noise measurement (Fig. 5.11) is not limited by the gain of the control loop (Fig. 5.10) up to Fourier frequencies of 10 kHz. However, increasing the bandwidth of the frequency stabilization control loop could be beneficial as it permits to raise the

UGF of the IMC control loop without causing loop instabilities[7].

Characterizing the frequency noise sources for Fourier frequencies below 80 Hz and above 5 kHz is essential (Sec. 5.4.1). However, if this noise originates from the reference cavity it is suppressed by the loop gain of the IMC control loop and will not contribute to the frequency noise at the input of the IFO. A second out-of-loop measurement with the IFO arms will provide a characterization of the reference cavity noise below 15 Hz and helps to identify and mitigate noise sources. For the Fourier frequency range between 80 Hz and 5 kHz vibration absorbers are currently installed on the periscope to damp mechanical resonances.

For further characterization of effects related to the high laser power, a long term IMC test, in order to obtain a high power out-of-loop frequency noise measurement can be conducted. This allows for a long term test of the control loop robustness in HPM and for a study of excess noise at low Fourier frequencies.

5.6 Summary

In this Chapter the laser frequency stabilization using the reference cavity and the IMC as sensor is described. Moreover, the unstabilized laser frequency noise is characterized in Section 5.1 and was found to follow the characteristic NPRO frequency noise for an operation in HPM and LPM.

For the description of the control loop (Sec. 5.2) a detailed study of the sensor (Sec. 5.2.1), controller (Sec. 5.2.2) and the actuator (Sec. 5.2.3) was performed. The actuator analysis includes an examination of the effects the HPO adds. It was determined that the HPO adds approximately 40 degree phase lag at 1 MHz to the control loop transfer function.

The performance of the full control loop is evaluated in Section 5.3. In LPM a UGF of 600 kHz is achieved whereas in HPM the additional phase lag allows an operation with a UGF of 380 kHz. The experimental data are in accordance with the control loop simulations presented in Section 5.2.4. EOM resonances at 780 kHz and 1.7 MHz limit the maximum bandwidth of the control loop.

An out-of-loop frequency noise measurement with the DBB resonator is limited by the resonator's inherent length noise (Sec. 5.3). Therefore an out-of-loop measurement is obtained with the IMC (Sec. 5.4.1). The measurement revealed that the input beam reaches a frequency noise stability of $6 \cdot 10^{-3}\,\mathrm{Hz}/\sqrt{\mathrm{Hz}}$ at a Fourier frequency of 1.5 kHz which is close to the coating thermal noise limit.

[7] As the current IMC transfer function has 45 degree phase margin at 100 kHz, it is possible to increase the UGF beyond 100 kHz in the current configuration. Splitting the IMC feedback signal into two paths and feeding fast frequency fluctuations directly back to the TTFSS error point circumvents the time delay introduced by the propagation of the acoustical wave in the AOM, allows for an even higher UGF [KBD+12]

This measurement was obtained after replacing the HPO water interface, which caused vibrations on the laser table due to a turbulent flow in conjunction with a high flow rate. The measured frequency noise is so far not limited by the loop gain of the frequency stabilization up to a Fourier frequency of 20 kHz.

In order to test the robustness of the IMC control loops and to study thermal effects the input power was increased to 120 W. By determination of the IMC pole frequency a method is presented which can determine clipping inside the IMC path which creates losses of more than 100 ppm (Sec. 5.4.2).

Further investigation are required to identify frequency noise sources below Fourier frequencies of 80 Hz and above 5 kHz (Sec. 5.5). An out-of-loop of frequency noise measurement below 15 Hz can only be obtained with the LIGO arm cavities as they are a more stable frequency reference than the IMC.

6 Conclusion

An ultra-stable high power laser is one of the key elements for a state-of-the-art interferometric gravitational wave detector. For Advanced LIGO the custom high power laser, the Pre-Modecleaner, the power- and frequency stabilization systems are described, analyzed and characterized in detail.

Three high power laser systems have been implemented, two of them at the LIGO observatories and the third at the AEI in Hannover. These systems operated without a major downtime for three years robustly and with the required noise performance. The long term characterization of the systems is described in Chapter 3. Moreover, a PMC was designed and extensively characterized. Contaminations related to the high power operation were found and mitigated.

In Chapter 4 the performance of the aLIGO power stabilization control loops was evaluated in two different configurations with a sensor inside and outside the vacuum system, respectively. In order to design and optimize the control loop a simulation was carried out before the control loop was implemented. Operating the loop with the in vacuum sensor a quantum noise limited stability at a relative power noise level of $3.5 \cdot 10^{-8}/\sqrt{\text{Hz}}$ was achieved over a Fourier frequency band between 30 Hz and 500 Hz. As contamination control issues in other LIGO subsystems did not allow for a higher power level it was not possible reach the design sensitivity of $2 \cdot 10^{-9}/\sqrt{\text{Hz}}$ at 10 Hz.

Since the requirements in terms of frequency stability did not change compared to iLIGO the existing frequency stabilization, which utilizes a rigid reference cavity as frequency reference, was adapted and optimized for the aLIGO configuration. The characterization (Chap. 5) revealed that the HPO adds 45 degree of phase lag at 1 MHz, which needs to be accounted for in the control loop design. Consequently, the UGF of the high bandwidth control loop is lower in HPM than in LPM when the HPO is switched off. The frequency noise was evaluated using the IMC as out-of-loop sensor. For a Fourier frequency

band from 20 Hz to 10 kHz the noise is below the requirements set by the GWD except for peaks in the 100 Hz to 1 kHz region, which are caused by vibrations of mechanical components on the laser table.

In order to study the thermal effects inside the IMC a high power test was conducted (Chap. 5). The input power level was raised up to 120 W and thermal effects were not disturbing the IMC operation.

A reliable and well characterized high power laser system is essential for the successful operation of a GWD. The aLIGO PSL described in this thesis forms such a system and will most likely provide the light for the first direct detection of gravitational waves.

Bibliography

[AAA+09a] B P Abbott, R Abbott, R Adhikari, P Ajith, B Allen, G Allen, R S Amin, S B Anderson, W G Anderson, M A Arain, M Araya, H Armandula, P Armor, Y Aso, S Aston, P Aufmuth, C Aulbert, S Babak, P Baker, S Ballmer, et al. LIGO: the laser interferometer gravitational-wave observatory. *Reports on Progress in Physics*, 72(7):076901, 2009. 1, 3, 84

[AAA+09b] F. Acernese, M. Alshourbagy, F. Antonucci, S. Aoudia, K. G. Arun, P. Astone, G. Ballardin, F. Barone, L. Barsotti, M. Barsuglia, Th. S. Bauer, S. Bigotta, S. Birindelli, M. A. Bizouard, C. Boccara, F. Bondu, L. Bonelli, L. Bosi, S. Braccini, C. Bradaschia, et al. Laser with an in-loop relative frequency stability of $1.0\text{x}10^{-21}$ on a 100-ms time scale for gravitational-wave detection. *Phys. Rev. A*, 79:053824, May 2009. 77

[AAA+12] T Accadia, F Acernese, M Alshourbagy, P Amico, F Antonucci, S Aoudia, N Arnaud, C Arnault, K G Arun, P Astone, S Avino, D Babusci, G Ballardin, F Barone, G Barrand, L Barsotti, M Barsuglia, A Basti, Th S Bauer, F Beauville,et al. VIRGO: a laser interferometer to detect gravitational waves. *Journal of Instrumentation*, 7(03):P03012, 2012. 1

[AAF11] Rich Abbott, Rana Adhikari, and Peter Fritschel. ISC RF photodetector design: LSC and WFS. Technical Report T1100402-v2, LIGO Document Control Center, 2011. 88

[ABF08] R. Adhikari, S. Ballmer, and P. Fritschel. Interferometer sensing

and control design requirements. Technical Report T-070236-00-D, LIGO Document Control Center, 2008. 77

[ACT+06] S Avino, E Calloni, A Tierno, B Agrawal, R De Rosa, L De Fiore, L Milano, and S R Restaino. Low-noise adaptive optics for gravitational wave interferometers. *Classical and Quantum Gravity*, 23(20):5919, 2006. 54

[Adh04] Rana Adhikari. *Sensitivity and Noise Analysis of 4 km Laser Interferometric Gravitational Wave Antennae*. PhD thesis, Massachusetts Institute of Technology, 2004. 84, 98

[Adh14] Rana X. Adhikari. Gravitational radiation detection with laser interferometry. *Rev. Mod. Phys.*, 86:121–151, Feb 2014. 3, 86

[AMM+09] M. Arain, G. Mueller, R. Martin, V. Quetschke, D. H. Reitze, D. B. Tanner, and L. Williams. Input optics subsystem design requirements document. Technical Report T-020020-04-D, LIGO Document Control Center, 2009. 77

[AMS97] Rich Abbott, James Mason, and Rick Savage. Npro frequency stabilization. Technical Report T-970051-00, LIGO Document Control Center, 1997. 82, 90

[And84] D. Z. Anderson. Alignment of resonant optical cavities. *Appl. Opt.*, 23:2944–2949, 1984. 10, 54

[AS09] C. Isaac Angert and Daniel Sigg. Characterization of a voltage controlled oscillator. Technical Report T0900451-v1, LIGO Document Control Center, 2009. 98

[ASM05] Rich Abbott, Paul Schwinberg, and Joshua Myers. Ttfss. Technical Report D040105-x0 (version B), LIGO Document Control Center, 2005. 89

[AtTC05] Masaki Ando and the TAMA Collaboration. Current status of the TAMA300 gravitational-wave detector. *Classical and Quantum Gravity*, 22(18):S881, 2005. 7

[BBC+02] F Bondu, A Brillet, F Cleva, H Heitmann, M Loupias, C N Man, H Trinquet, and the VIRGO Collaboration. The VIRGO injection system. *Classical and Quantum Gravity*, 19(7):1829, 2002. 7, 74

[BC01] Alessandra Buonanno and Yanbei Chen. Quantum noise in second generation, signal-recycled laser interferometric gravitational-wave detectors. *Phys. Rev. D*, 64:042006, Jul 2001. 5

[BFMB96] F. Bondu, P. Fritschel, C. N. Man, and A. Brillet. Ultrahigh-spectral-purity laser for the VIRGO experiment. *Opt. Lett.*, 21(8):582–584, Apr 1996. 82

[Bftat12] L. Barsotti and P. Fritschel for the aLIGO team. Early aLIGO configurations: example scenarios toward design sensitivity. Technical Report LIGO-T1200307-v4, LIGO Document Control Center, 2012. 61

[BGF+03] Raymond G. Beausoleil, Eric K. Gustafson, Martin M. Fejer, Erika D'Ambrosio, William Kells, and Jordan Camp. Model of thermal wave-front distortion in interferometric gravitational-wave detectors. i. thermal focusing. *J. Opt. Soc. Am. B*, 20(6):1247–1268, Jun 2003. 35

[Bla01] E. D. Black. An introduction to pound-drever-hall laser frequency stabilization. *American Journal of Physics*, 1:79–87, 2001. 14, 85, 95

[BLFB08] Amber L. Bullington, Brian T. Lantz, Martin M. Fejer, and Robert L. Byer. Modal frequency degeneracy in thermally loaded optical resonators. *Appl. Opt.*, 47(15):2840–2851, May 2008. 35

[Bog13] Christina Bogan. *Stabilized High Power Lasers and Spatial Mode Conversion*. PhD thesis, University of Hannover, 2013. 7, 19, 44, 50, 53, 74

[BR03] Hans-A. Bachor and Timothy C. Ralph. *A Guide to Experiments in Quantum Optics*. Wiley-VCH, 2003. 40, 41

[Bro99] O. S. Brozek. *Frequenzstabilisierung eines Nd:YAG-Hochleistungs-Laser-Systems für den Gravitationswellendetektor GEO 600*. PhD thesis, University of Hannover, 1999. 78, 79, 82

[BSK05] B W Barr, K A Strain, and C J Killow. Laser amplitude stabilization for advanced interferometric gravitational wave detectors. *Classical and Quantum Gravity*, 22(20):4279, 2005. 39

[BTD01] Joshua C. Bienfang, Russell F. Teehan, and Craig A. Denman. Phase noise transfer in resonant optical cavities. *Review of Scientific Instruments*, 72:3208–3214, 2001. 84

[CBF+13] L. Carbone, C. Bogan, P. Fulda, A. Freise, and B. Willke. Generation of high-purity higher-order laguerre-gauss beams at high laser power. *Phys. Rev. Lett.*, 110:251101, Jun 2013. 7

[CHK+10] C. W. Chou, D. B. Hume, J. C. J. Koelemeij, D. J. Wineland, and T. Rosenband. Frequency comparison of two high-accuracy Al^+ optical clocks. *Phys. Rev. Lett.*, 104:070802, Feb 2010. 77

[Col14] BICEP2 Collaboration. Bicep2 i: Detection of b-mode polarization at degree angular scales. *arXiv:submit/0934323*, 2014. 1

[CSA+13] Tara Chelermsongsak, Frank Seifert, Koji Arai, Rana Adhikari, and Eric Gustafson. Thermal noise probe experiment. Technical Report T-1200057-v11, LIGO Document Control Center, 2013. 86, 96, 101

[Day90] Timothy Day. *Frequency stabilized solid state lasers for coherent optical communications*. PhD thesis, Stanford University, 1990. 78, 82

[DHK+83] R. W. P. Drever, J. L. Hall, F. V. Kowalski, J. Hough, G. M. Ford, A. J. Munley, and H. Ward. Laser phase and frequency stabilization using an optical resonator. *Applied Physics B: Lasers and Optics*, 31:97–105, 1983. 14

[EBF+08] M. Evans, S. Ballmer, M. Fejer, P. Fritschel, G. Harry, and G. Ogin. Thermo-optic noise in coated mirrors for high-precision optical measurements. *Phys. Rev. D*, 78:102003, Nov 2008. 86

[Ein16] Albert Einstein. Näherungsweise Integration der Feldgleichungen der Gravitation. *Sitzungsberichte der Königlich Preussischen Akademie der Wissenschaften Berlin*, pages 688–696, 1916. 1

[Ein18] Albert Einstein. Über Gravitationswellen. *Sitzungsberichte der Königlich Preussischen Akademie der Wissenschaften Berlin*, pages 154–167, 1918. 1

[FGB95] Alejandro D. Farinas, Eric K. Gustafson, and Robert L. Byer. Frequency and intensity noise in an injection-locked, solid-state laser. *J. Opt. Soc. Am. B*, 12(2):328–334, Feb 1995. 81

[Flo11] Angel Flores. Coherent beam combining of fiber amplifiers in a kw regime. In *CLEO:2011 - Laser Applications to Photonic Applications*, page CFE3. Optical Society of America, 2011. 26

[Fri93] P. Fritschel. Notes on the laser frequency stabilization. Technical Report VIR-NOT-LAL-1380-51, VIRGO collaboration, 1993. 86, 96, 97

[FSW+07] M. Frede, B. Schulz, R. Wilhelm, P. Kwee, F. Seifert, B. Willke, and D. Kracht. Fundamental mode, single-frequency laser amplifier for gravitational wave detectors. *Optics Express*, 15:459–465, 2007. 7, 13, 19, 70

[ftLSC13] Lisa Barsotti for the LIGO Scientific Collaboration. Enhanced sensitivity of the LIGO gravitational wave detector by using squeezed states of light. *Nat Photon*, 7(8):613–619, 08 2013. 43

[FWB+04] M. Frede, R. Wilheim, M. Brendel, C. Fallnich, F. Seifert, B. Willke, and K. Danzmann. High power fundamental mode Nd:YAG laser with efficient birefringence compensation. *Optics Express*, 12:3581–3589, 2004. 12

[FWKF05] Maik Frede, Ralf Wilhelm, Dietmar Kracht, and Carsten Fallnich. Nd:YAG ring laser with 213 W linearly polarized fundamental mode output power. *Opt. Express*, 13(19):7516–7519, Sep 2005. 12

[Gar05] F. M. Gardner. *Phaselock Techniques*. Wiley-Interscience, 2005. 79

[GBM+10] C. Gréverie, A. Brillet, C.N. Man, W. Chaibi, J.P. Coulon, and K. Feliksik. High power fiber amplifier for Advanced VIRGO. In *Lasers and Electro-Optics (CLEO) and Quantum Electronics and Laser Science Conference (QELS), 2010 Conference on*, pages 1–2, May 2010. 25

[GK04] Christopher C. Gerry and Peter L. Knight. *Introductory Quantum Optics*. Cambridge University Press, 2004. 40

[Gro07] H. Grote. High power, low-noise, and multiply resonant photodetector for interferometric gravitational wave detectors. *Review of Scientific Instruments*, 78(5):–, 2007. 88

[GS11] J.J. Gorman and B. Shapiro. *Feedback Control of MEMS to Atoms*. MEMS Reference Shelf. Springer, 2011. 51

[GtLSC10] H Grote and the LIGO Scientific Collaboration. The GEO 600 status. *Classical and Quantum Gravity*, 27(8):084003, 2010. 1

[GWI13] GWINC. Gwinc - gravitational wave interferometer noise calculator. Technical Report https://awiki.ligo-wa.caltech.edu/aLIGO/GWINC, LIGO Scientific Collaboration, 2013. 5

[Hei99] Gerhard Heinzel. *Advanced optical techniques for laser-interferometric graviational-wave detectors*. PhD thesis, Max-Planck-Institut für Quantenoptik, 1999. 11, 61

[Hei00] Gerhard Heinzel. Program for linearsimulation and optimization of analog electronic circuits, 2000. 48

[HGB+94] C.C. Harb, M.B. Gray, H.-A. Bachor, R. Schilling, P. Rottengatter, I. Freitag, and H. Welling. Suppression of the intensity noise in a diode-pumped neodymium:yag nonplanar ring laser. *Quantum Electronics, IEEE Journal of*, 30(12):2907–2913, Dec 1994. 79

[HGS+02] Gregory M Harry, Andri M Gretarsson, Peter R Saulson, Scott E Kittelberger, Steven D Penn, William J Startin, Sheila Rowan, Martin M Fejer, D R M Crooks, Gianpietro Cagnoli, Jim Hough, and Norio Nakagawa. Thermal noise in interferometric gravitational wave detectors due to dielectric optical coatings. *Classical and Quantum Gravity*, 19(5):897, 2002. 85

[HH84] J. L. Hall and T. W. Hänsch. External dye-laser frequency stabilizer. *Opt. Lett.*, 9(11):502–504, Nov 1984. 81

[HtLSC10] Gregory M Harry and the LIGO Scientific Collaboration. Advanced LIGO: the next generation of gravitational wave detectors. *Classical and Quantum Gravity*, 27(8):084006, 2010. 1, 3, 45

[HV90] Hello, Patrice and Vinet, Jean-Yves. Analytical models of thermal aberrations in massive mirrors heated by high power laser beams. *J. Phys. France*, 51(12):1267–1282, 1990. 35

[Kaw03] Seiji Kawamura. Configuration study of pre-mode cleaner and reference cavity in the 40m PSL system. Technical Report T030149-00-R, LIGO Document Control Center, 2003. 97

[KB85] T. J. Kane and R. L. Byer. Monolithic, unidirectional single-mode Nd:YAG ring laser. *Optics Letters*, 10:65–67, 1985. 13

[KBD+12] P. Kwee, C. Bogan, K. Danzmann, M. Frede, H. Kim, P. King, J. Pöld, O. Puncken, R. L. Savage, F. Seifert, P. Wessels, L. Winkelmann, and B. Willke. Stabilized high-power laser system for the gravitational wave detector Advanced LIGO. *Opt. Express*, 20(10):10617–10634, May 2012. 2, 32, 35, 48, 50, 60, 70, 74, 105

[KIK+14] Keiko Kokeyama, Kiwamu Izumi, William Z. Korth, Nicolas Smith-Lefebvre, Koji Arai, and Rana X. Adhikari. Residual amplitude modulation in interferometric gravitational wave detectors. *J. Opt. Soc. Am. A*, 31(1):81–88, Jan 2014. 96

[KRHM85] G.A. Kerr, N.A. Robertson, J. Hough, and C.N. Man. The fast frequency stabilisation of an argon laser to an optical resonator using an extra-cavity electro-optic modulator. *Applied Physics B*, 37(1):11–16, 1985. 81

[KSA06] Peter Fritschel Kentaro Somiya, Osamu Miyakawa and Rana Adhikari. Length sensing and control for adLIGO. Technical Report T060272-00-I, LIGO Document Control Center, 2006. 46

[KSWD07] P. Kwee, F. Seifert, B. Willke, and K. Danzmann. Laser beam quality and pointing measurement with an optical resonator. *Review of Scientific Instruments*, 78(7):073103, 2007. 10, 16, 28

[KTAAM07] Z. Derrar Kaddour, A. Taleb, K. Ait-Ameur, and G. Martel. Revisiting gouy phase. *Optics Communications*, 280(2):256 – 263, 2007. 35

[KW08] Patrick Kwee and Benno Willke. Automatic laser beam characterization of monolithic Nd:YAG nonplanar ring lasers. *Appl. Opt.*, 47(32):6022–6032, Nov 2008. 19, 21, 79, 90

[KWD08] P. Kwee, B. Willke, and K. Danzmann. Optical ac coupling to overcome limitations in the detection of optical power fluctuations. *Opt. Lett.*, 33:1509–1511, 2008. 32, 45

[KWD09] P. Kwee, B. Willke, and K. Danzmann. Shot-noise-limited laser power stabilization with a high-power photodiode array. *Opt. Lett.*, 34:2912–2914, 2009. 39, 56, 60, 64

[KWD10] P Kwee, B Willke, and K Danzmann. Quantum limit of different laser power stabilization schemes involving optical resonators. *Journal of Physics: Conference Series*, 228(1):012023, 2010. 44

[Kwe05] P. Kwee. Charakterisierung von lasersystemen für gravitationswellendetektoren. *Diplomarbeit*, 2005. 79

[Kwe10] Patrick Kwee. *Laser characterization and stabilization for precision interferometry*. PhD thesis, University of Hannover, 2010. 44, 59

[Lev98] Yu. Levin. Internal thermal noise in the LIGO test masses: A direct approach. *Phys. Rev. D*, 57:659–663, Jan 1998. 85

[LFR+02] Brian Lantz, Peter Fritschel, Haisheng Rong, Ed Daw, and Gabriela González. Quantum-limited optical phase detection at the 10^{-10}-rad level. *J. Opt. Soc. Am. A*, 19(1):91–100, Jan 2002. 77

[Liu05] J.-M. Liu. *Photonic Devices*. Cambridge University Press, 2005. 51

[Mee88] Brian J. Meers. Recycling in laser-interferometric gravitational-wave detectors. *Phys. Rev. D*, 38:2317–2326, Oct 1988. 4

[Miz95] Jun Mizuno. *Comparison of optical configurations for laser-interferometric gravitational-wave detectors*. PhD thesis, University of Hannover, 1995. 4, 10

[MMaM+09] J. Millo, D. V. Magalhães, C. Mandache, Y. Le Coq, E. M. L. English, P. G. Westergaard, J. Lodewyck, S. Bize, P. Lemonde, and G. Santarelli. Ultrastable lasers based on vibration insensitive cavities. *Phys. Rev. A*, 79:053829, May 2009. 86

[MMRW94] Euan Morrison, Brian J. Meers, David I. Robertson, and Henry Ward. Automatic alignment of optical interferometers. *Appl. Opt.*, 33(22):5041–5049, Aug 1994. 18

[MMT+13] R. Martin, G. Mueller, D. B. Tanner, L. Williams, J. Gleason, D. Feldbaum, C. Mueller, and M. Heintze. Advanced LIGO input optics final design: Baffles, layouts, mode-matching telescope, alignment. Technical Report T0900386-v6, LIGO Document Control Center, 2013. 97, 103

[MMT+14] Chris Mueller, Rodica Martin, David Tanner, Cheryl Vorvick, Luke Williams, and Guido Mueller. Alignment of the in-vacuum input optics. Technical Report T13000327-v1, LIGO Document Control Center, 2014. 60

[MOMM07] Norikatsu Mio, Takafumi Ozeki, Kosuke Machida, and Shigenori Moriwaki. Laser intensity stabilization system using laser-diode-pumped Nd:YAG rod-laser amplifier. *Japanese Journal of Applied Physics*, 46(8A):5338–5341, 2007. 39

[MSN+93] J. Mizuno, K.A. Strain, P.G. Nelson, J.M. Chen, R. Schilling, A. Rüdiger, W. Winkler, and K. Danzmann. Resonant sideband extraction: a new configuration for interferometric gravitational wave detectors. *Physics Letters A*, 175(5):273 – 276, 1993. 45

[Mue05] Guido Mueller. Beam jitter coupling in Advanced LIGO. *Opt. Express*, 13(18):7118–7132, Sep 2005. 28

[Mue14] Chris Mueller. The Advanced LIGO input mode cleaner. Technical Report G1400096, LIGO Document Control Center, 2014. 98, 101

[Mül09] Guido Müller. Pointing requirements for Advanced LIGO. Technical Report T0900142-v2, LIGO Document Control Center, 2009. 55, 60, 97

[MWD10] Tobias Meier, Benno Willke, and Karsten Danzmann. Continuous-wave single-frequency 532 nm laser source emitting 130 W into the fundamental transversal mode. *Opt. Lett.*, 35(22):3742–3744, Nov 2010. 7

[MWG+14] R. Martin, L. Williams, J. Gleason, R. Savage, and G. Mueller. Mode matching to iss-pd. Technical Report LIGO T-1400176-v1, LIGO Document Control Center, 2014. 60, 73

[NKA+03] Shigeo Nagano, Seiji Kawamura, Masaki Ando, Ryutaro Takahashi, Koji Arai, Mitsuru Musha, Souichi Telada, Masa-Katsu Fujimoto, Mitsuhiro Fukushima, Yoshihide Kozai, Shoken Miyama, Akitoshi Ueda, Koichi Waseda, Toshitaka Yamazaki, Hideki Ishizuka, Kazuaki Kuroda, Sumihiro Matsumura, Osamu Miyakawa, Shinji Miyoki, Masatake Ohashi, et al. Development of a multistage laser frequency stabilization for an interferometric gravitational-wave detector. *Review of Scientific Instruments*, 74:4176–4183, 2003. 82

[NKC04] Kenji Numata, Amy Kemery, and Jordan Camp. Thermal-noise limit in the frequency stabilization of lasers with rigid cavities. *Phys. Rev. Lett.*, 93:250602, Dec 2004. 86

[Noc04] F. Nocera. LIGO laser intensity noise suppression. *Classical and Quantum Gravity*, 21(5):S481–S485, 2004. 74

[NRS06] T. Nazarova, F. Riehle, and U. Sterr. Vibration-insensitive reference cavity for an ultra-narrow-linewidth laser. *Applied Physics B*, 83(4):531–536, 2006. 86

[OMM10] Noriaki Ohmae, Shigenori Moriwaki, and Norikatsu Mio. Wideband and high-gain frequency stabilization of a 100-W injection-locked Nd:YAG laser for second-generation gravitational wave detectors. *Review of Scientific Instruments*, 81(7):–, 2010. 82, 104

[OVH+00] D.J. Ottaway, P.J. Veitch, C. Hollitt, D. Mudge, M.W. Hamilton, and J. Munch. Frequency and intensity noise of an injection-locked Nd:YAG ring laser. *Applied Physics B*, 71(2):163–168, 2000. 20

[Põl09] Jan Hendirk Põld. Stabilization of the Advanced LIGO 200W laser. Diploma Thesis, 2009. 12, 26, 32, 50, 90

[Pun11] Oliver Puncken. *Pumpkopfdesign für den Advanced LIGO Laser*. PhD thesis, Leibniz Universität Hannover, 2011. 12

[Que08] Volker Quetschke. Electro-optic modulators and modulation for Enhanced LIGO and beyond. In *Coherent Optical Technologies and Applications*, page CMC1. Optical Society of America, 2008. 53

[RftL13] D. H. Reitze and D. H. Shoemaker for the LVC. Gravitational-wave physics and astronomy using ground-based interferometers. In *WSPC - Proceedings*, 2013. 6

[ROZ+04] Jameson Rollins, David Ottaway, Michael Zucker, Rainer Weiss, and Richard Abbott. Solid-state laser intensity stabilization at the 10-8 level. *Opt. Lett.*, 29(16):1876–1878, Aug 2004. 39

[RSS+81] A. Rüdiger, R. Schilling, L. Schnupp, W. Winkler, H. Billing, and K. Maischberger. A mode selector to suppress fluctuations in laser beam geometry. *Optica Acta: International Journal of Optics*, 28(5):641–658, 1981. 26

[Sau94] P. R. Saulson. *Fundamentals of Interferometric Gravitational Wave Detectors*. World Scientific, 1994. 5, 26, 45

[SBJ+98] R. Storz, C. Braxmaier, K. Jäck, O. Pradl, and S. Schiller. Ultrahigh long-term dimensional stability of a sapphire cryogenic optical resonator. *Opt. Lett.*, 23(13):1031–1033, Jul 1998. 86

[SCKM06] K. Somiya, Y. Chen, S. Kawamura, and N. Mio. Frequency noise and intensity noise of next-generation gravitational-wave detectors with rf/dc readout schemes. *Phys. Rev. D*, 73:122005, Jun 2006. 45

[SCKM07] K. Somiya, Y. Chen, S. Kawamura, and N. Mio. Erratum: Frequency noise and intensity noise of next-generation gravitational-wave detectors with rf/dc readout schemes [phys. rev. d 73, 122005 (2006)]. *Phys. Rev. D*, 75:049905, Feb 2007. 45

[Sei09] F. Seifert. *Power Stabilization of High Power Lasers for Second Generation Gravitational Wave Detectors*. PhD thesis, University of Hannover, 2009. 44, 53, 58, 62

[Sie86] Siegman. *Lasers*. University Science Books, 1986. 13, 16, 19

[SKH+06] F. Seifert, P. Kwee, M. Heurs, B. Willke, and K.Danzmann. Laser power stabilization for second-generation gravitational wave detectors. *Opt. Lett.*, 31:2000–2002, 2006. 39

[SKS98] R. L. Savage, P. J. King, and S. U. Seel. A highly-stabilized 10-watt Nd:YAG laser for the laser interferometer gravitational-wave observatory (LIGO). *LIGO Scientific Collaboration, P980002-00-D*, 1998. 7, 82

[Som12] Kentaro Somiya. Detector configuration of KAGRA–the japanese cryogenic gravitational-wave detector. *Classical and Quantum Gravity*, 29(12):124007, 2012. 1

[SS09] Daniel Sigg and Paul Schwinberg. Ttfss assembly. Technical Report D0901897-v1, LIGO Document Control Center, 2009. 89

[SSR+97] Stefan Seel, Rafael Storz, Giuseppe Ruoso, Jürgen Mlynek, and Stephan Schiller. Cryogenic optical resonators: A new tool for laser frequency stabilization at the 1 hz level. *Phys. Rev. Lett.*, 78:4741–4744, Jun 1997. 86

[ST58] A. L. Schawlow and C. H. Townes. Infrared and optical masers. *Phys. Rev.*, 112:1940–1949, Dec 1958. 79

[ST91] Saleh and Teich. *Fundamentals of Photonics*. Wiley-Interscience, 1991. 8, 9, 11, 12

[TAT08] K Takahashi, M Ando, and K Tsubono. Stabilization of laser intensity and frequency using optical fiber. *Journal of Physics: Conference Series*, 122(1):012016, 2008. 39

[Tea11] Einstein Telescope Science Team. *Einstein gravitational wave Telescope conceptual design study, http://www.et-gw.eu/*, 2011. 26

[TPN+11] Henrik Tünnermann, Jan Hendrik Pöld, Jörg Neumann, Dietmar Kracht, Benno Willke, and Peter Weßels. Beam quality and noise properties of coherently combined ytterbium doped single frequency fiber amplifiers. *Opt. Express*, 19(20):19600–19606, Sep 2011. 26

[TSF+02] R. Takahashi, Y. Saito, M. Fukushima, M. Ando, K. Arai, D. Tatsumi, G. Heinzel, S. Kawamura, T. Yamazaki, and S. Moriwaki. Direct measurement of residual gas effect on the sensitivity in TAMA300. *Journal of Vacuum Science and Technology A*, 20:1237–1241, 2002. 86

[TSNK12] T. Theeg, H. Sayinc, J. Neumann, and D. Kracht. All-fiber counter-propagation pumped single frequency amplifier stage with 300-W output power. *Photonics Technology Letters, IEEE*, 24(20):1864–1867, Oct 2012. 25

[Tün13] Henrik Tünnermann. *Fiber Amplifiers for Gravitational Wave Detectors: Temporal Dynamics and Coherent Beam Combining*. PhD thesis, University of Hannover, 2013. 26

[TWMB95] Matthew S. Taubman, Howard Wiseman, David E. McClelland, and Hans-A. Bachor. Intensity feedback effects on quantum-limited noise. *J. Opt. Soc. Am. B*, 12(10):1792–1800, Oct 1995. 44

[UGFB97] Noboru Uehara, Eric K. Gustafson, Martin M. Fejer, and Robert L. Byer. Modeling of efficient mode-matching and thermal-lensing effect on a laser-beam coupling into a mode-cleaner cavity. *Proc. SPIE*, 2989:57–68, 1997. 35

[UU94] N. Uehara and K. Ueda. Ultrahigh-frequency stabilization of a diode-pumped Nd:YAG laser with a high-power-acceptance photodetector. *Opt. Lett.*, 19(10):728–730, May 1994. 82

[Vaj14] Gabriele Vajente. Summary of the iss status at livingston. Technical Report G1400403-v1, LIGO Document Control Center, 2014. 73

[VB99] S.P. Vyatchanin V.B. Braginsky, M.L. Gorodetsky. Thermodynamical fluctuations and photo-thermal shot noise in gravitational wave antennae. *Physics Letters A*, 264(1):1–10, 1999. 86

[VKL+10] Henning Vahlbruch, Alexander Khalaidovski, Nico Lastzka, Christian Gräf, Karsten Danzmann, and Roman Schnabel. The GEO 600 squeezed light source. *Classical and Quantum Gravity*, 27(8):084027, 2010. 43

[WBD+00] B. Willke, S. Brozek, K. Danzmann, V. Quetschke, and S. Gossler. Frequency stabilization of a monolithic Nd:YAG ring laser by controlling the power of the laser-diode pump source. *Opt. Lett.*, 25:1019–1021, 2000. 82, 96

[WDRS91] W. Winkler, K. Danzmann, A. Rüdiger, and R. Schilling. Heating by optical absorption and the performance of interferometric gravitational-wave detectors. *Phys. Rev. A*, 44:7022–7036, Dec 1991. 35

[WGB85] Edward A. Whittaker, Manfred Gehrtz, and Gary C. Bjorklund. Residual amplitude modulation in laser electro-optic phase modulation. *J. Opt. Soc. Am. B*, 2(8):1320–1326, Aug 1985. 96

[Win12] Lutz Winkelmann. *Injection-locked high power oscillator for Advanced gravitational wave observatories*. PhD thesis, Leibniz Universität Hannover, 2012. 12, 18, 81

[Wis99] H. M. Wiseman. Light amplification without stimulated emission: Beyond the standard quantum limit to the laser linewidth. *Phys. Rev. A*, 60:4083–4093, Nov 1999. 79

[WKSF11] B. Willke, P. King, R. Savage, and P. Fritschel. Pre-stabilized laser design requirements. Technical Report T-050036-v4, LIGO Document Control Center, 2011. 12, 46, 77

[WNT10] J. M. Weisberg, D. J. Nice, and J. H. Taylor. Timing measurements of the relativistic binary pulsar psr b1913+16. *The Astrophysical Journal*, 722(2):1030, 2010. 1

[WPK+11] L. Winkelmann, O. Puncken, R. Kluzik, C. Veltkamp, P. Kwee, J. Poeld, C. Bogan, B. Willke, M. Frede, J. Neumann, P. Wessels, and D. Kracht. Injection-locked single-frequency laser with an output power of 220 W. *Applied Physics B*, 102(3):529–538, 2011. 2, 12, 18

[WUG+98] B. Willke, N. Uehara, E. K. Gustafson, R. L. Byer, P. J. King, S. U. Seel, and Jr. R. L. Savage. Spatial and temporal filtering of a 10-W Nd:YAG laser with a fabry–perot ring-cavity premode cleaner. *Opt. Lett.*, 23(21):1704–1706, Nov 1998. 26

[YDD+11] JiangY. Y., LudlowA. D., LemkeN. D., FoxR. W., ShermanJ. A., MaL. S., and OatesC. W. Making optical atomic clocks more stable with 10-16-level laser stabilization. *Nat Photon*, 5(3):158–161, 03 2011. 77

[YIO+96] S. T. Yang, Y. Imai, M. Oka, N. Eguchi, and S. Kubota. Frequency-stabilized, 10-W continuous-wave, laser-diode end-pumped, injection-locked Nd:YAG laser. *Opt. Lett.*, 21(20):1676–1678, Oct 1996. 81

[Zaw03] I. Zawischa. *Injektionsgekoppelte diodengepumpte Nd:YAG- und Nd:YVO_4-Laser für terrestrische interferometrische Gravitationswellendetektoren*. PhD thesis, University of Hannover, 2003. 13, 20

[ZBD+02] I Zawischa, M Brendel, K Danzmann, C Fallnich, M Heurs, S Nagano, V Quetschke, H Welling, and B Willke. The GEO 600 laser system. *Classical and Quantum Gravity*, 19(7):1775, 2002. 7

[ZRO02] Mike Zucker, Jamie Rollins, and David Ottaway. High bandwidth FSS card. Technical Report T020091-00-D, LIGO Document Control Center, 2002. 92

[Zuc89] Michael E. Zucker. *Experiments with a laser interferometric gravitational wave antenna*. PhD thesis, California Institute of Technology, 1989. 81

Publications

[1] P. Kwee, C. Bogan, K. Danzmann, M. Frede, H. Kim, P. King, J. Pöld, O. Puncken, R. L. Savage, F. Seifert, P. Wessels, L. Winkelmann, and B. Willke. Stabilized high-power laser system for the gravitational wave detector advanced LIGO. *Opt. Express*, 20(10):10617–10634, May 2012.

[2] K Dahl, T Alig, G Bergmann, A Bertolini, M Born, Y Chen, A V Cumming, L Cunningham, C Gräf, G Hammond, G Heinzel, S Hild, S H Huttner, R Jones, F Kawazoe, S Köhlenbeck, G Kühn, H Lück, K Mossavi, P Oppermann, J Pöld, K Somiya, A A van Veggel, A Wanner, T Westphal, B Willke, K A Strain, S Goßler, and K Danzmann. Status of the AEI 10 m prototype. *Classical and Quantum Gravity*, 29(14):145005, 2012.

[3] Fumiko Kawazoe, Gerald Bergmann, Alessandro Bertolini, Michael Born, Yanbei Chen, Alan V Cummning, Liam Cunningham, Katrin Dahl, Christian Gräf, Giles Hammond, Gerhard Heinzel, Stefan Hild, Sabina H Huttner, Russell Jones, Sina Köhlenbeck, Gerrit Kühn, Harald Lück, Kasem Mossavi, Jan Hendrik Pöld, Kentaro Somiya, A Marielle van Veggel, Alexander Wanner, Tobias Westphal, Benno Willke, Kenneth Strain, Stefan Goßler, and Karsten Danzmann. The AEI 10 m prototype interferometer frequency control using the reference cavity and its angular control. *Journal of Physics: Conference Series*, 363(1):012012, 2012.

[4] T. Westphal, G. Bergmann, A. Bertolini, M. Born, Y. Chen, A.V. Cumming, L. Cunningham, K. Dahl, C. Gräf, G. Hammond, G. Heinzel, S. Hild, S. Huttner, R. Jones, F. Kawazoe, S. Köhlenbeck, G. Kühn, H. Lück, K. Mossavi, J.H. Pöld, K. Somiya, A.M. Veggel, A. Wanner, B. Willke, K.A.

Strain, S. Goßler, and K. Danzmann. Design of the 10 m AEI prototype facility for interferometry studies. *Applied Physics B*, 106(3):551–557, 2012.

[5] Henrik Tünnermann, Jan Hendrik Pöld, Jörg Neumann, Dietmar Kracht, Benno Willke, and Peter Weßels. Beam quality and noise properties of coherently combined ytterbium doped single frequency fiber amplifiers. *Opt. Express*, 19(20):19600–19606, Sep 2011.

[6] L. Winkelmann, O. Puncken, R. Kluzik, C. Veltkamp, P. Kwee, J. Poeld, C. Bogan, B. Willke, M. Frede, J. Neumann, P. Wessels, and D. Kracht. Injection-locked single-frequency laser with an output power of 220 W. *Applied Physics B*, 102(3):529–538, 2011.

[7] Jan Hendirk Põld. Stabilization of the Advanced LIGO 200W laser. Diplomarbeit, 2009.

[8] J. Aasi, ..., J.H. Pöld, and ... First searches for optical counterparts to gravitational-wave candidate events. *The Astrophysical Journal Supplement Series*, 211(1):7, 2014.

[9] J. Aasi, ..., J.H. Pöld, and ... Search for long-lived gravitational-wave transients coincident with long gamma-ray bursts. *Phys. Rev. D*, 88:122004, Dec 2013.

[10] J. Aasi, ..., J.H. Pöld, and ... Directed search for continuous gravitational waves from the galactic center. *Phys. Rev. D*, 88:102002, Nov 2013.

[11] J. Aasi, ..., J.H. Pöld, and ... Parameter estimation for compact binary coalescence signals with the first generation gravitational-wave detector network. *Phys. Rev. D*, 88:062001, Sep 2013.

[12] J. Aasi, ..., J.H. Pöld, and ... Enhanced sensitivity of the LIGO gravitational wave detector by using squeezed states of light. *Nat Photon*, 7(8):613–619, 08 2013.

[13] J. Aasi, ..., J.H. Pöld, and ... Einstein@home all-sky search for periodic gravitational waves in LIGO S5 data. *Phys. Rev. D*, 87:042001, Feb 2013.

[14] Adrián-Martínez S., ..., J.H. Pöld, and ... A first search for coincident gravitational waves and high energy neutrinos using LIGO, Virgo and ANTARES data from 2007. *Journal of Cosmology and Astroparticle Physics*, 2013(06):008, 2013.

[15] J. Aasi, ..., J.H. Pöld, and ... Search for gravitational waves from binary black hole inspiral, merger, and ringdown in LIGO-Virgo data from 2009–2010. *Phys. Rev. D*, 87:022002, Jan 2013.

[16] J. Abadie, ..., J.H. Pöld, and ... Upper limits on a stochastic gravitational-wave background using LIGO and Virgo interferometers at 600–1000 Hz. *Phys. Rev. D*, 85:122001, Jun 2012.

[17] J. Abadie, ..., J.H. Pöld, and ... All-sky search for gravitational-wave bursts in the second joint LIGO-Virgo run. *Phys. Rev. D*, 85:122007, Jun 2012.

[18] J. Abadie, ..., J.H. Pöld, and ... Search for gravitational waves from intermediate mass binary black holes. *Phys. Rev. D*, 85:102004, May 2012.

[19] J. Abadie, ..., J.H. Pöld, and ... Search for gravitational waves from low mass compact binary coalescence in LIGO's sixth science run and Virgo's science runs 2 and 3. *Phys. Rev. D*, 85:082002, Apr 2012.

[20] J. Abadie, ..., J.H. Pöld, and ... Search for gravitational waves associated with gamma-ray bursts during LIGO science run 6 and Virgo science runs 2 and 3. *The Astrophysical Journal*, 760(1):12, 2012.

[21] J. Abadie, ..., J.H. Pöld, and ... Implications for the origin of GRB 051103 from LIGO observations. *The Astrophysical Journal*, 755(1):2, 2012.

[22] J. Abadie, ..., J.H. Pöld, and ... Swift follow-up observations of candidate gravitational-wave transient events. *The Astrophysical Journal Supplement Series*, 203(2):28, 2012.

[23] J. Aasi, ..., J.H. Pöld, and ... The characterization of Virgo data and its impact on gravitational-wave searchesirgo data and its impact on gravitational-wave searches. *Classical and Quantum Gravity*, 29(15):155002, 2012.

[24] J. Abadie, ..., J.H. Pöld, and ... All-sky search for periodic gravitational waves in the full S5 LIGO data. *Phys. Rev. D*, 85:022001, Jan 2012.

[25] J. Abadie, ..., J.H. Pöld, and ... Implementation and testing of the first prompt search for gravitational wave transients with electromagnetic counterparts. *Astronomy and Astrophysics*, 539:A124, 2012.

[26] J. Abadie, ..., J.H. Pöld, and ... First low-latency LIGO+Virgo search for binary inspirals and their electromagnetic counterparts. *Astronomy and Astrophysics*, 541:A155, 2012.

[27] J. Abadie, ..., J.H. Pöld, and ... A gravitational wave observatory operating beyond the quantum shot-noise limit. *Nat Phys*, 7(12):962–965, 12 2011.

[28] J. Abadie, ..., J.H. Pöld, and ... Beating the spin-down limit on gravitational wave emission from the vela pulsar. *The Astrophysical Journal*, 737(2):93, 2011.

[29] J. Abadie, ..., J.H. Pöld, and ... Search for gravitational wave bursts from six magnetars. *The Astrophysical Journal Letters*, 734(2):L35, 2011.

Acknowledgements

First of all, I would like to thank Benno Willke for his mentoring and dedicated support in person and remotely. His advises and numerous scientific discussions were always very helpful.

A special thanks goes to Valera Frolov, who taught me a lot about LIGO and Gravitational Wave detectors and supported my work at the LIGO site.

For the perfect team work during the Advanced LIGO laser installations and commissioning as well as the fun times off site I would like to thank Christina, Patrick, Olli, Lutz, Peter, Mike and Rick.

I particularly enjoyed being part of the LIGO Livingston detector commissioning team. During long nights at the detector, problems with my measurements or searching for a place to stay for a few weeks I could always count on the help of Adam, Anamaria, Chris, David, Den, Keiko, Koji, Matt, Rich, Ryan, Suresh, Zach and the staff at the LIGO Livingston observatory. Thank you guys for an awesome time abroad.

I enjoyed the relaxed and productive atmosphere at the AEI Hannover and with our collaborators in Hannover. Therefore I would like to thank Patrick, Frank, Tobias, Steffen, Robin, Reza, Michaela, Hyunjoo, Henning, Gerrit, Maik, Basti, Christian, Matthias, Marcin, Peter and the colleagues at AEI.

Many thanks to Gerald for his Ansys support and Henrik for the collaborative work on the coherent beam combining experiment.

Finally, I would like to express my gratitude to my family for their unlimited support, to Sarah for brightening up my life in the last couple of months and to Vanaisa, who already impressed me as a child with his knowledge and dedication to science.

About the Author

Jan Hendrik Põld was born on the 11th of September in Bielefeld, Germany. He received his Abitur at the Friedrich-von-Bodelschwigh-Gymnasium Bielefeld in 2004. Afterwards he studied Physics at the Leibniz Universität Hannover and received the diploma degree for his work on the Advanced LIGO 200 W laser in 2009.

Since then he works as research associate at the Max-Planck-Institute for Gravitational Physics (Albert-Einstein-Institut) and the Leibniz Universität Hannover. He got a three year scholarship from the International Max Planck Research School on Gravitational Wave Astronomy and a six month scholarship from the German Academic Exchange Service. During his PhD work he was a visiting research student at the California Institute of Technology between 2011 and 2013.